University of California
Santa Barbara

Defect Physics and Hydrogen Transport in Solid-State Hydrogen Electrolytes from First Principles

A dissertation submitted in partial satisfaction
of the requirements for the degree

Doctor of Philosophy
in
Materials

by

Andrew Joseph Even Rowberg

Committee in charge:

Professor Chris G. Van de Walle, Chair
Professor Anton Van der Ven
Professor Ram Seshadri
Professor Bradley F. Chmelka

September 2021

The Dissertation of Andrew Joseph Even Rowberg is approved.

Professor Anton Van der Ven

Professor Ram Seshadri

Professor Bradley F. Chmelka

Professor Chris G. Van de Walle, Committee Chair

September 2021

Defect Physics and Hydrogen Transport in Solid-State Hydrogen Electrolytes from First Principles

by

Andrew Joseph Even Rowberg

To my parents, my biggest fans

Acknowledgements

As I write these acknowledgements, it is remarkable to think of all that has transpired over the past five years. I walked into the Engineering II Building on September 12, 2016 as a relatively fresh-faced first-year PhD student, completely unversed in the ways of first-principles calculations, and now, I prepare to leave with a wealth of experience, a nice publication record, and a host of people to thank for making my time in Santa Barbara memorable.

First and foremost, I am indebted to my thesis advisor, Prof. Chris G. Van de Walle, for welcoming me into the group and teaching me so much about how to be a better scientist and communicator. One thing I deeply admire about Chris is his willingness to ask questions about just about anything—rather than take a statement at face value, he digs deep to make sure (a) that it is accurate, and (b) that he understands why. His questions during group meetings and one-on-one discussions and in comments files for our papers have pushed me away from complacency and toward being a more curious, open-minded researcher. I am grateful for his patience with my mistakes, his support for my development as a scientist, and his eagerness to see me succeed.

I also thank the members of my thesis committee, Profs. Anton Van der Ven, Ram Seshadri, and Brad Chmelka. It has been a great privilege to interact with all three of them during my PhD tenure, as they have all been exceedingly gracious and supportive of my research, while asking excellent questions and providing helpful feedback.

It has been a true pleasure to get to know the postdocs and fellow graduate students who have called the Van de Walle Group home over the years, and I have benefitted tremendously from our interactions, scientific and otherwise. First, I am grateful to Dr. Leigh Weston, my most frequent coauthor and a valued mentor as I was getting started in the group and starting to learn the ropes of DFT. It has also been a great

pleasure working with my other coauthors, Drs. Karthik Krishnaswamy, Santosh KC, Michael Swift, and Sai Mu, with whom I enjoyed profitable and pleasant working relationships. My thanks as well to the other members of the group with whom I have overlapped: Prof. Hartwin Peelaers; Drs. Nicholas Adamski, Youngho Kang, Stephanie Mack, Jimmy Shen, Yongjin Shin, Mengen Wang, Wennie Wang, Darshana Wickramaratne, Baiyu Zhang, Xie Zhang, Fangzhou Zhao, Zhen Zhu; and Future Drs. Yubi Chen, Azi Jackson, Mark Turiansky, and Haochen Wang. I will cherish my memories of the group, from our legendary barbeques on Goleta Beach, to occasional LAN parties and hiking/camping outings. The good news about the science life is that one is rarely more than a conference away from catching up with old colleagues, so here's to making more memories in the not-too-distant future.

I am also grateful to my mentors from beyond UCSB. In particular, I credit my first research advisor, Prof. Mark C. Hersam at Northwestern University, for teaching me many valuable lessons about taking initiative and managing time. In addition to being a world-class researcher, Mark is a fantastic person who, somehow, always finds the time in his jam-packed schedule for the members and alumni of his enormous group—even the undergrads like me! Dr. Tejas Shastry, my graduate-student mentor in the Hersam Group, was a great guide for me with his confidence, intelligence, and patience. In the summer of 2017, I had the great opportunity to work as a summer intern at Lawrence Livermore National Lab, under the supervision of Dr. Brandon C. Wood, who taught me a lot and was very supportive of my work. I also thank Drs. Tadashi Ogitsu and Sabrina Wan, with whom I interacted closely at the lab, and my experimental collaborators Drs. Jim White and Farid El Gabaly, who were enthusiastic supporters of my DFT work. I learned a lot about the process of collaborative research from my time working with them, and I look forward to more fruitful collaborations as I prepare to start work as a postdoctoral researcher at LLNL.

My work at UCSB would not have been possible without the generous support of my funders. I am very thankful to the National Science Foundation for supporting my PhD education with a Graduate Research Fellowship. I also thank the Department of Energy for providing the primary funding for my work on hydrogen electrolytes while at UCSB, as well as the Office of Naval Research and the Air Force Office for Scientific Research for supporting me at various points during my PhD tenure. Computational resources from the DOE, NSF, and DOD allowed me to run the pricey calculations needed to obtain the results presented in this thesis and in my publications. The ever-available UCSB campus resources provided through the Center for Scientific Computing, part of the California NanoSystems Institute, definitely made my life a lot easier, too. I am very appreciative of the work Paul Weakliem and Fuzzy Rogers do maintaining the on-campus computing resources and supporting the research being done at UCSB, as well as the many others working at user facilities around the country to keep the metaphorical lights on for people like me.

I would be remiss if I did not also thank the staff who made sure that everything behind the scenes ran smoothly here at UCSB. I am thinking particularly of the steady leadership of Jocelyn Guzman in the Materials Department main office, as well as the attention to detail exhibited by Fukiko Miyazaki and Emi Sautot processing so many of my reimbursement requests, and many others beside.

I must also acknowledge that, even beyond my research endeavors, I have had a lot of fun in grad school—one might perhaps say too much fun! It has been a privilege to be a part of many groups in and around UCSB during my five years here, through which I have made a number of meaningful friendships. Of these, I certainly must thank all the wonderful people I have gotten to know through the UCSB Bridge Club, which I founded on a bit of a whim in 2017, and with which I won the Online College Bridge Championship in 2020. I was even profiled in the UCSB Current and

interviewed by a podcast for my bridge exploits! Thanks, too, to my good friends at the Santa Barbara Bridge Center downtown, who rooted for me along my journey to becoming a Life Master this past summer. I am also grateful to the members of the Grad News Bears, my intramural softball team, with whom I crossed an item off my bucket list by winning an intramural championship in 2019 (that's a lot of championships for one PhD career!). Outside of the competitive realm, I am thankful to my fellow members of the Graduate Simulation Seminar Series (GS^3), which I helped organize for three years and through which I brought people together from across campus (and the country) to discuss their diverse computational research topics in a fun, friendly setting. Finally, I am grateful to have exercised the right half of my brain through my five-year membership in the UCSB Chamber Choir, from which I have many fond memories, and as part of my ever-supportive church family at the University Methodist Church in Isla Vista. Along with my enjoyment of Santa Barbara's uniquely beautiful natural diversions, from the beaches to the mountaintops, these groups helped keep me grounded and at peace through the ups and downs of grad school.

I am so very appreciative of everyone who was supported me over the years. I have been blessed with many wonderful, lifelong friends from different phases in my life: from my first home in Northern Virgina; from my time at Northwestern University; from my year as a Fulbright fellow in Munich, Germany; and from Santa Barbara. The same goes for my family, including the aunts, uncles, and cousins whom I have had the welcome chance to see much more frequently while living on the West Coast. And, in particular, my immediate family: my brother, Jeffrey, and my parents, Dick and Nancy, and their cats, of course. I am the person I am today because of their love and support. Both of my parents showed me what can come of hard work and kindness, as they navigated successful careers in Washington, D.C. to make an indisputable

impact in policy, notably, in my mother's case, helping to craft the seminal Americans with Disabilities Act (ADA). And I would not be completing my PhD without the inspiration of my father, who received his PhD in plasma physics from UCLA just more than 50 years ago and had a really impactful career in science policy. If I can continue to lead a life inspired by their example, mine will be a life well-lived.

Curriculum Vitæ
Andrew Joseph Even Rowberg

Education

2021	Ph.D. in Materials Science (Expected) University of California, Santa Barbara
2015	B.S., Summa Cum Laude, in Materials Science and Engineering, and Engineering Science and Applied Mathematics Northwestern University

Awards

2021	Bright Horizon Global Foundation Materials Department Service Award
2021	Ovshinsky Student Travel Award, American Physical Society, Division of Materials Physics
2020	UC President's Lindau Nobel Laureate Meetings Fellow
2019	Doctoral Student Travel Grant, UCSB Academic Senate
2016	National Science Foundation Graduate Research Fellowship
2015	U.S. Fulbright Program Student Fellowship

Publications

1	Maogang Gong, Tejas A. Shastry, Qiannan Cui, Ryan R. Kohlmeyer, Kyle A. Luck, Andrew J. E. Rowberg, Tobin J. Marks, Michael F. Durstock, Hui Zhao, Mark C. Hersam, and Shenqiang Ren. **"Understanding Charge Transfer in Carbon Nanotube-Fullerene Bulk Heterojunctions,"** *ACS Applied Materials & Interfaces* **7**, 7428 (2015).
2	Tejas A. Shastry, Sarah C. Clark, Andrew J. E. Rowberg, Kyle A. Luck, Kan-Sheng Chen, Tobin J. Marks, and Mark C. Hersam. **"Enhanced Uniformity and Area Scaling in Carbon Nanotube-Fullerene Bulk-Heterojunction Solar Cells Enabled by Solvent Additives,"** *Advanced Energy Materials* **6**, 1501466 (2016).

3 Andrew J. E. Rowberg, Leigh Weston, and Chris G. Van de Walle. **"Ion-Transport Engineering of Alkaline-Earth Hydrides for Hydride Electrolyte Applications,"** *Chemistry of Materials* **30**, 5878 (2018).

4 James L. White, Andrew J. E. Rowberg, Liwen F. Wan, ShinYoung Kang, Tadashi Ogitsu, Robert D. Kolasinski, Josh A. Whaley, Alexander A. Baker, Jonathan R. I. Lee, Yi-Sheng Liu, Lena Trotochaud, Jinghua Guo, Vitalie Stavila, David Prendergast, Hendrik Bluhm, Mark D. Allendorf, Brandon C. Wood, and Farid El Gabaly.
"Identifying the Role of Dynamic Surface Hydroxides in the Dehydrogenation of Ti-Doped $NaAlH_4$," *ACS Applied Materials & Interfaces* **11**, 4930 (2019).

5 Andrew J. E. Rowberg, Leigh Weston, and Chris G. Van de Walle. **"Optimizing Proton Conductivity in Zirconates Through Defect Engineering,"** *ACS Applied Energy Materials* **2**, 2611 (2019).

6 Santosh KC, Andrew J. E. Rowberg, Leigh Weston, and Chris G. Van de Walle.
"First-Principles Study of Antisite Defects in Perovskite Stannates," *Journal of Applied Physics* **126**, 195701 (2019).

7 Andrew J. E. Rowberg, Karthik Krishnaswamy, and Chris G. Van de Walle.
"Prospects for High Carrier Mobility in the Cubic Germanates," *Semiconductor Science and Technology* **35**, 085030 (2020).

8 Andrew J. E. Rowberg, Karthik Krishnaswamy, and Chris G. Van de Walle.
"Inflection Points in the Conduction-Band Structure of $BaSnO_3$," *Physical Review B* **102**, 115201 (2020).

9 Andrew J. E. Rowberg, Leigh Weston, and Chris G. Van de Walle. **"Defect Chemistry and Hydrogen Transport in La/Sr-Based Oxyhydrides,"** *The Journal of Physical Chemistry C* **125**, 2250 (2021).

10 Andrew J. E. Rowberg, Michael W. Swift, and Chris G. Van de Walle.
"Understanding Carbon Contamination in the Proton-Conducting Zirconates and Cerates," *Physical Chemistry Chemical Physics* **23**, 14205 (2021).

11 Andrew J. E. Rowberg and Chris G. Van de Walle.
"Hydride Conductivity in Nitride Hydrides," *ACS Applied Energy Materials* **4**, 6348 (2021).

12 Sai Mu, Andrew J. E. Rowberg, Joshua Leveillee, Feliciano Giustino, and Chris G. Van de Walle.
"First-principles study of electron transport in ScN," *Physical Review B* **104**, 075118 (2021).

13 Andrew J. E. Rowberg, Sai Mu, Michael W. Swift, and Chris G. Van de Walle.
"Structural, electronic, and polarization properties of YN and LaN," *Physical Review Materials* **Accepted** (2021).

Contributed Talks

2021 American Physical Society March Meeting, Online Meeting
"Prospects for High Carrier Mobility in the Cubic Germanates"

2020 American Physical Society March Meeting, Denver, CO
"Defect Chemistry in La/Sr-Based Oxyhydrides"

2019 Hydrogen-Metal Interactions Gordon Research Conference, Barcelona, Spain
"Defect Engineering of Hydrogen Electrolyte Materials"

2019 American Physical Society March Meeting, Boston, MA
"Optimizing Proton Conductivity in Zirconates through Defect Engineering"

2018 Defects in Semiconductors Gordon Research Seminar, New London, NH
"Ion-Transport Engineering of Alkaline-Earth Hydrides for Hydride Transport Applications"

2017	American Physical Society March Meeting, Los Angeles, CA "Defect Properties of Alkaline-Earth Hydrides for Hydrogen Energy Applications"
2016	American Physical Society March Meeting, New Orleans, LA "First-Principles Calculations of Barium Hydride for Hydrogen Transport Applications"

Invited Talks

2020	American Physical Society March Meeting, Denver, CO "First-Principles Design of Solid-State Hydrogen Electrolytes"

Abstract

Defect Physics and Hydrogen Transport in Solid-State Hydrogen Electrolytes from First Principles

by

Andrew Joseph Even Rowberg

Hydrogen is an attractive carrier of renewable energy due to its natural abundance, high energy density, and lack of harmful byproducts when converted to electricity in a fuel cell. Solid-state hydrogen fuel cells are gaining particular attention for their stability, storage capacity, and ability to operate at high temperatures. However, their technological adoption requires highly conductive solid-state hydrogen electrolytes. In crystalline electrolytes, conductivity is tied to the concentration of mobile hydrogen defects, be they hydrogen interstitials or vacancies. Increasing the concentration of such defects improves the ionic conductivity. Understanding how to do so requires knowledge of the defect chemistry, including native point defects as well as extrinsic dopants and impurities.

To this end, we examine a suite of prospective solid-state hydrogen electrolyte materials using accurate first-principles calculations based on density functional theory with a hybrid functional. These include proton-conducting oxides, such as the alkaline-earth zirconates ($CaZrO_3$, $SrZrO_3$, $BaZrO_3$) and cerates ($SrCeO_3$ and $BaCeO_3$), as well as several hydride-ion conductors, namely, the alkaline-earth hydrides (CaH_2, SrH_2, and BaH_2), $La_{2-x-y}Sr_{x+y}LiH_{1-x+y}O_{3-y}$ oxyhydrides, and the nitride hydride Sr_2LiH_2N. We report on calculations of defect formation energies under conditions representative of experimental growth and operation.

Our results suggest approaches for improving ionic conductivity through defect engineering. For instance, in the alkaline-earth zirconates and hydrides, we show that alkali metal dopants boost the concentration of mobile hydrogen defects, while also possessing low Coulombic binding energies to those defect species so as not to hinder their mobility. Native point defects and extrinsic impurities also affect these materials' chemical stability. In the alkaline-earth cerates, carbon impurities hamper device performance and stability, and we show specifically why their impact is worse than in the zirconates. For the oxyhydrides and nitride hydride, the same defects that grant them high hydride conductivity provide a stabilizing effect that may permit synthesis.

The work summarized here lays a foundation for the development of solid-state fuel cells and of hydrogen as a reliable energy source. These goals require the engineering of novel materials such as those described here; thus, our results provide essential knowledge to help power a sustainable energy future.

Contents

List of Figures

List of Tables

Chapter 1

Introduction

1.1 Overview

Of all the crises facing humankind in the 21st century, none is more profound for the future of our species than that of climate change. Studies on the greenhouse effect and how human sources contribute to it date back to calculations by Svante Arrhenius performed at the end of the 19th century [1]; however, widespread acknowledgement of the problem is typically linked with NASA director James Hansen's testimony before Congress in 1988 [2]. Even at the time, the recognition that humans contribute to climate change was long overdue, and a continued lack of action has allowed the climate crisis to become increasingly more acute. It presents dire consequences by spurring refugee movement, increasing the intensity of storms and fires, decreasing biodiversity, and negatively impacting the global economy and public health [3], and scientists agree that it requires significant, unified public action to address [4].

There is widespread agreement that the most effective solution to combat climate change is the adoption of so-called "green" or "renewable" forms of energy [5, 6]. In contrast to more conventional forms of energy, such as oil and natural gas, renewable

energy sources have a practically infinite supply, and they do not directly produce greenhouse gases such as carbon dioxide (CO_2), which is the largest contributor to climate change. There are numerous sources of renewable energy under investigation, among them, solar, wind, geothermal, and hydroelectric power. Most likely, all of these and other energy sources will play a role in decarbonizing humanity's energetic footprint.

This thesis will focus on one particular carrier of renewable energy: hydrogen. Hydrogen is, by far, the most abundant element in the Universe. It is also the most abundant element on Earth; here, however, it is most commonly present in molecules including water (H_2O) and fossil fuels [7, 8]. It has attracted significant research over the years due to its exceptionally high gravimetric energy density, which is roughly three times that of natural gas [9–11]. This chapter will provide an overview of hydrogen energy; namely, how electricity is generated through the use of hydrogen fuel cells, and the current status of hydrogen energy's adoption. Subsequent chapters will outline our contributions to research into solid-state hydrogen fuel cell technology, beginning with the computational methodology rooted in density-functional theory covered in Chapter 2, and continuing with case studies into different material systems being considered for hydrogen energy devices. The thesis will then conclude with a brief outlook for the field in the years to come.

1.2 Hydrogen Fuel Cells

Diatomic hydrogen (H_2) possesses an exceptionally high gravimetric energy density of 142 MJ/kg, more than three times that of natural gas (47 MJ/kg) [9]. The most common means for obtaining energy from H_2 is through the use of a fuel cell, which

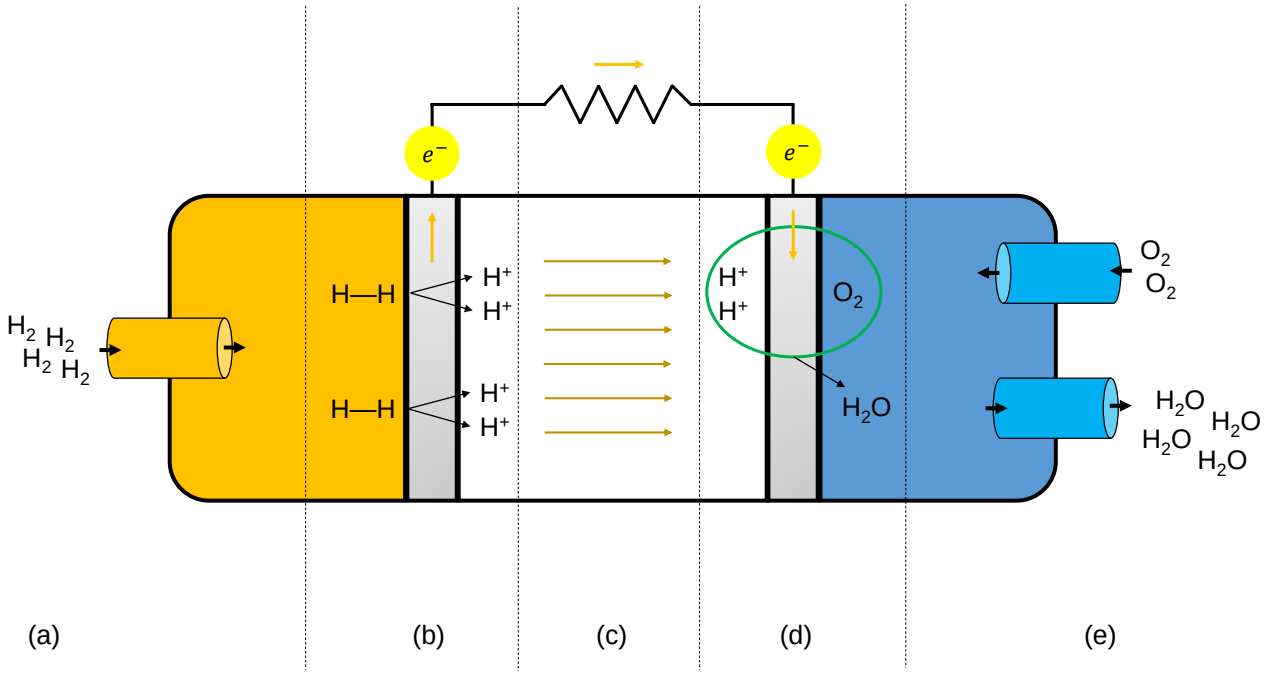

Figure 1.1: The operation of a hydrogen fuel cell, split into five parts. (a) Hydrogen gas (H_2) is supplied from an external store. (b) H_2 is split at the anode into two protons (H^+) and two electrons (e^-). (c) Protons pass through the electrolyte, while electrons are conducted through a circuit to generate electrical power or charge a battery. (d) Protons and electrons meet molecular oxygen (O_2) at an interface between the electrolyte and cathode, where they combine to form water (H_2O). (e) Water is then released as the sole byproduct of the reaction.

makes use of the hydrogen electrochemical reaction:

$$2H_2 + O_2 \rightarrow 2H_2O + \Delta E, \tag{1.1}$$

where ΔE is the aforementioned energy density of H_2, released during the reaction. Importantly, this process is carbon neutral; water is the only chemical byproduct.

The precise mechanism by which H_2 reacts with molecular oxygen (O_2) in a fuel cell is depicted schematically in Fig. 1.1 [10, 12]. Key to the operation of a fuel cell is the ability to ionize atomic hydrogen.

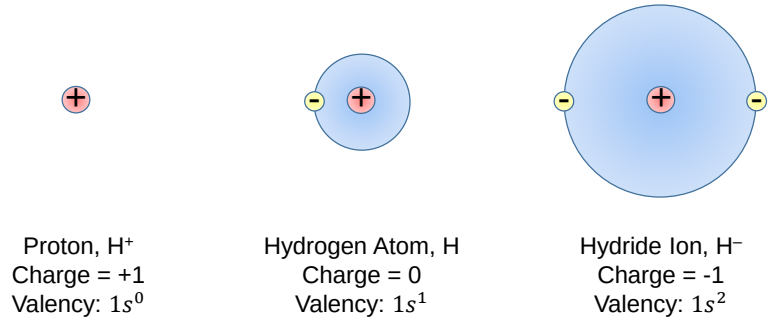

Figure 1.2: The ions of hydrogen, H, as they would incorporate as interstitials in a host material. The 1*s* valence shell of hydrogen prefers to be empty of electrons, giving rise to small, positively charged protons (H^+), or to be filled with two electrons, which yields larger, negatively charged hydride ions (H^-). Compared with protons and hydride ions, the hydrogen atom (H^0) is not easily stabilized in materials.

The movement of ionic hydrogen through the electrolyte, depicted in the middle section of the fuel cell [Fig. 1.1(c)], drives the movement of charge to help generate electricity. In most fuel cells, hydrogen ionizes as positively charged protons (H^+); however, hydrogen can just as readily ionize as negatively charged hydride ions (H^-). This ability to adopt two opposite charge states favorably is unique to hydrogen, leading some to call it the "non-conformist" element [13]. The ions of hydrogen, as they would be seen in an electrolyte, are depicted schematically in Fig. 1.2.

By taking into account the ionization of hydrogen, Eq. 1.1 can be separated into two components. The first, shown schematically in Fig. 1.1(b), can be described (for protons) as follows:

$$H_2 \rightarrow 2H^+ + 2e^-. \tag{1.2}$$

Similarly, for hydride ions, an analogous splitting can be expressed as:

$$H_2 \rightarrow 2H^- + 2h^+, \tag{1.3}$$

with h^+ referring to holes, the positively charged quasiparticle signaling the absence of electrons. Note that the operation of a fuel cell making use of hydride ions is effectively identical to that of the schematic in Fig. 1.1, except that the ionic charge carriers of hydrogen have an opposite sign, and electrons flow through the circuit in the opposite direction. In the second component of the reaction, these hydrogen ions combine with O_2 to form water:

$$2H^+ + \frac{1}{2}O_2 + 2e^- \rightarrow H_2O. \tag{1.4}$$

For hydride ions, the analogous reaction can be written as:

$$2H^- + \frac{1}{2}O_2 + 2h^+ \rightarrow H_2O. \tag{1.5}$$

At both electrolyte interfaces, with the anode and with the cathode [Fig. 1.1(b) and (d)], the reactions are aided by the presence of a catalyst, typically platinum [10, 14].

In this thesis, we will focus on the properties of electrolytes. Current commercial hydrogen fuel cells incorporate polymer electrolyte membranes (PEMs), typically Nafion™, to transport hydrogen ions and drive an electric current [14, 15]. However, these polymeric systems have limited stability and fairly small temperature ranges for operation [16]. As a result, one outstanding goal of hydrogen energy research is to replace this polymer with a solid-state electrolyte, which offers higher operating temperatures and superior stability [10, 17]. The realm of solid-state hydrogen electrolytes is vast, though it can be divided into two overarching categories, proton conductors and hydride ion conductors, both of which will be discussed in this thesis. To begin, it is necessary to understand the distinct conduction mechanisms for protons and hydride ions, which will be treated in the following two subsections.

1.2.1 Proton Conduction

Proton diffusion typically proceeds through one of two mechanisms. The vehicle mechanism describes the movement of protons as part of a larger diffusing species, such as the hydronium (H_3O^+) ion or the ammonium (NH_4^+) ion, which moves through a system [18]. The vehicle mechanism is most common in aqueous electrolytes; thus, we will not consider it further in this discussion.

Structural diffusion, on the other hand, is more prevalent in solid systems, for which the diffusion of large species is untenable. It is shown schematically in Fig. 1.3(a). This mechanism is often referred to as "Grotthuss diffusion" due to its similarity to the proton diffusion mechanism first described by von Grotthuß [19]. However, it should be noted that Grotthuss diffusion traditionally focuses specifically on proton transfer through hydrogen-bonded liquids (e.g., H_2O), rather than solids in which hydrogen is an impurity—thus, the moniker is not entirely appropriate for this mechanism. In structural diffusion, protons bond with anionic species, and these bonds can typically be broken and reformed easily. For protons to diffuse through a system, the anionic species must be structurally flexible so that they can reorient sufficiently to facilitate proton hopping to neighboring sites [18, 20].

Many of the best solid-state proton conductors are perovskite oxides [21], which adopt a crystal structure similar to that of the perovskite mineral, $CaTiO_3$. Standard perovskite oxides have the generic chemical formula ABO_3, where A and B are cations. Structural diffusion relies on the ability of bonds in a lattice to reorient themselves to create the hydrogen bonding environments necessary for proton transfer; therefore, systems with more flexible bonds are preferred [21–23]. In the case of perovskites, proton transfer proceeds by way of repeated hopping of interstitial protons from one oxygen anion to another [Fig. 1.3(a)].

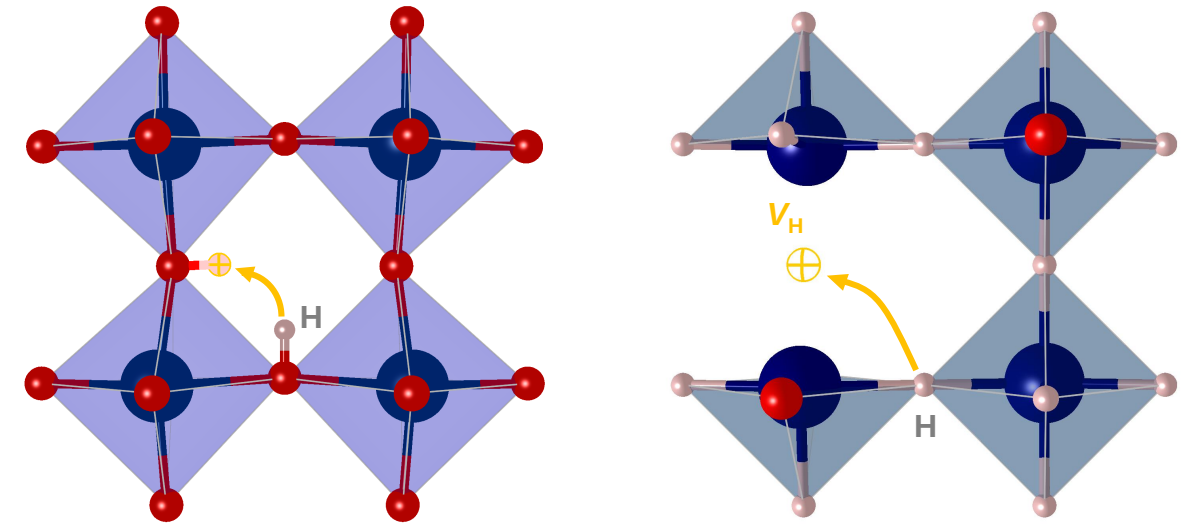

Figure 1.3: Schematics of common diffusion mechanisms in solid-state electrolytes for (a) protons and (b) hydride ions. In proton conductors, hydrogen is loosely bonded to native anions and migrates through the material by hopping from one anion site to another. In hydride conductors, migration is most commonly mediated by vacancies, which allow native hydride anions to move within the crystal.

1.2.2 Hydride Ion Conduction

Hydride ions, which contain a full 1*s* valence shell (Fig. 1.2), are the smallest and most mobile of anions. Their moderate electronegativity allows them to form covalent, metallic, and ionic bonds in materials in which they are found [24]. In comparison with protons, reactions involving hydride ions are typically found to proceed at slower rates and depend more strongly on temperature [25]. In materials for which hydride ion migration has been extensively studied, including oxyhydrides and some metal hydrides [26–29], hydride ions diffuse most readily via exchange with vacancies. This process is shown schematically in Fig. 1.3(b). In other materials, however, such as NaH [30], $LiBH_4$ [31], MgH_2 [32], and $NaAlH_4$ [33], interstitial hydride ion migration barriers were computationally determined to be smaller than the barriers for vacancy-mediated diffusion, implying that interstitial diffusion may be most prominent for those systems. In either case, the presence of the mobile defect species (vacancies or interstitials) is critical for hydride diffusion to proceed.

1.3 Current Status of the Field

The first proposals for creating a "hydrogen society", in which energy from hydrogen can be used to power day-to-day applications, came from a Danish scientist in the late 19th century [34]. A slow development of the technology followed over the course of the 20th century [7], in which hydrogen gained notoriety (perhaps unfairly so [35]) for its oft-cited role in the Hindenburg airship disaster in 1937. However, the 21st century has seen a marked increase in development of the technology due to heavy government interest and investment, which peaked in the early 2000s, dropped dramatically after 2008, and has since risen again worldwide [7, 11]. Hydrogen vehicles

are currently available for lease in California [36], while infrastructure for hydrogen-powered mass transit and industrial equipment continues to develop, particularly in Japan, but also in such countries as China, France, and Germany [7].

The U.S. Department of Energy (DOE) managed about $200 million in FY2019 for hydrogen energy research, which was directed by the Fuel Cell Technologies Office (FCTO) in collaboration with dozens of partners at universities, national laboratories, and industries [37]. This continuing work aims to reach DOE's goals for hydrogen cost and storage by 2050, by which time hydrogen could satisfy approximately 18% of the world's energy demand and reduce CO_2 emissions by 40–60% [38]. In terms of cost, DOE has set an ultimate target of $30/kW for a polymer electrolyte membrane (PEM) fuel cell with an 80 kW power output, which includes a $4/kg cost for H_2 at the pump [39]. Current prices are considerably higher: between $50/kW and $210/kW for fuel cells, depending on the system volume, and up to $16/kg for H_2 at the pump [40]. For on-board storage in hydrogen-powered vehicles, an ultimate cost of $8/kWh is needed, which can be compared with the high cost of compressed H_2 of up to $24/kWh [39].

Clearly, major materials advances are needed to meet these goals. Current production of hydrogen, while widespread, is based almost exclusively on combustion of natural gas [41–43], and this process contributes worldwide to annual CO_2 emissions on par with the total CO_2 output of Indonesia and the United Kingdom combined [7]. A possibly game-changing solution funded by the FCTO lies in materials capable of efficient water-splitting, including III-V photoabsorbers [44] and electrolytically active ABX_3 perovskites [39, 45]. Such water-splitting technology is still in its infancy, however. More viable, at present, are facilities that use renewable energy generated from solar cells or wind turbines to electrolyze water. This approach provides a possible path toward grid balancing, which addresses the imbalance between supply and

demand for renewable energy by storing unneeded energy for later use—in this case, that energy is stored in the form of hydrogen [46, 47].

Reducing fuel cell costs through replacements for the expensive platinum catalyst is another promising avenue [48–50]. In current fuel cells, the catalyst makes up approximately 40% of the total cost, making it a critical component for optimization [51]. Simply replacing the catalyst with one that does not contain platinum would reduce the cost associated with the catalyst by two orders of magnitude [40]. As such, significant research efforts are being directed toward designing platinum-free catalysts, typically comprised of more affordable transition metals such as cobalt, manganese, and iron, which still can offer high catalytic activity [50, 52]. Alternatively, using nanocrystalline alloys of platinum with other metals, such as nickel, lowers costs by reducing the required platinum content and, in addition, improves durability and catalytic performance (the latter by a factor of 80) [53].

Finally, minimizing the storage volume of hydrogen is critical in vehicular applications, for which space is at a premium. Hydrogen has an exceptionally low density as a molecular gas (approximately 0.09 kg m^{-3} at room temperature and atmospheric pressure), meaning that high-pressure tanks are required for its storage, and liquid hydrogen is similarly difficult to store on account of its low critical temperature (–241 °C) [9]. As a result, there is tremendous interest in complex metal hydrides, which possess some of the best storage densities for hydrogen [17, 34, 54]. Understanding the kinetics for hydrogen uptake and release in these systems is of key importance [55, 56]. Beyond simply using solid-state systems to store hydrogen, there is interest in developing all-solid-state hydrogen fuel cells, which require solid-state, crystalline electrolytes with high ionic conductivity for hydrogen. As previously mentioned, these systems provide key advantages of stability and higher permissible operating temper-

atures as compared with PEM fuel cells, which degrade at low temperatures [10, 16, 17].

1.4 Goals of this Thesis

This thesis will highlight our recent theoretical and computational research into the properties and design of emerging solid-state hydrogen electrolyte materials. Chapter 2 will introduce the primary methodology: density-functional theory based on a hybrid exchange-correlation functional. The bulk of the remainder of the thesis will highlight several notable materials systems, differentiating between proton conductors and hydride-ion conductors, as shown in Fig. 1.4.

Proton-conducting oxides will be discussed in Chapter 3. Specifically, we will discuss the zirconates ($CaZrO_3$, $SrZrO_3$, and $BaZrO_3$), which are among the best proton-conducting oxides. The chapter will include an in-depth analysis of their point-defect properties, including an analysis of acceptor dopants needed to incorporate hydrogen. In addition, we will discuss their propensity to form detrimental carbonate complexes. Their chemical stability with respect to carbonates will be contrasted with that of the cerates ($SrCeO_3$ and $BaCeO_3$), which are more conductive than the zirconates but less stable.

Hydride-ion conductors will be the focus of the remaining chapters. Chapter 4 will examine the hydride ion-conducting alkaline-earth hydrides (CaH_2, SrH_2, and BaH_2), again from the perspective of point defects and their relationship to ionic conductivity. We will discuss the properties of acceptor dopants necessary to improve hydride conductivity. Chapter 5 will introduce the mixed anionic oxyhydrides, specifically La_2LiHO_3 and Sr_2LiH_3O, which are among the best-known hydride-ion conductors. A particular focus will be placed on their disparate stability and conductivity and

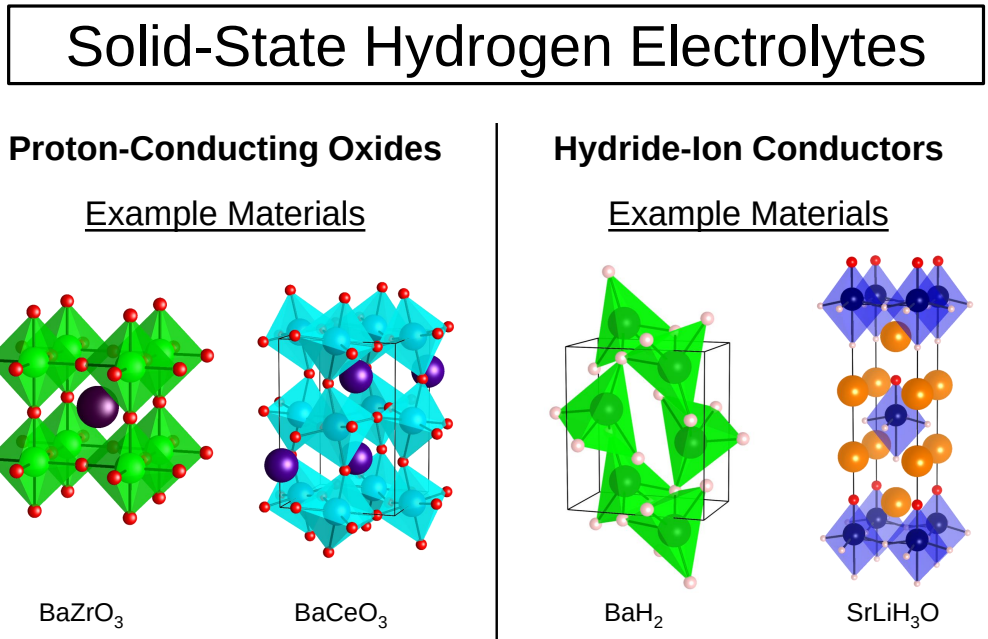

Figure 1.4: A schematic of different types of hydrogen electrolytes examined in this thesis, highlighting pertinent properties and objectives relevant to the work.

how both can be tuned through defect engineering and optimized synthesis conditions. Chapter 6 will share insights on a little-explored material, Sr_2LiH_2N, a mixed anionic nitride hydride that exhibits exceptionally low activation energies for hydride-ion conduction. Finally, Chapter 7 will summarize the research results presented and provide a brief outlook for future research directions into solid-state hydrogen energy materials.

Chapter 2

A First-Principles Approach to Calculating Point Defects

2.1 Many-Body Quantum Mechanics

2.1.1 The Schrödinger Wave Equation

All matter is comprised of atoms, which, in turn consist of positively charged nuclei and smaller, negatively charged electrons. Studying the properties of materials therefore requires an understanding of the behavior of these particles. The mass of the nuclei is large enough for them to be approximated in many cases as classical particles; however, electrons are several orders of magnitude lighter and necessarily require a quantum mechanical treatment.

Quantum mechanics is an inherently probabilistic science, with the Schrödinger wave equation at its core [57]:

$$i\hbar\frac{\partial\Psi}{\partial t} = -\frac{\hbar^2}{2m_e}\nabla^2\Psi + V\Psi. \tag{2.1}$$

Note that the formulation above is for a single electron. Here, $i = \sqrt{-1}$, $\hbar$ is Planck's constant divided by 2π, m_e is the electron mass, and V is some external potential, which may or may not have a spatial or time dependence. $\Psi = \Psi(x,t)$ is the wavefunction of the electron, which does not have any physical meaning itself; rather, it was shown by Max Born that $|\Psi|^2$ is the probability distribution of the electron [58]. The ∇^2 operator is a spatial second derivative—were we assuming that Ψ only had spatial dependence along the x-direction, we could instead write it as $\frac{\partial^2\Psi}{\partial x^2}$.

It is common to use the time-independent Schrödinger equation for problems in which time dependence can be neglected:

$$-\frac{\hbar^2}{2m_e}\nabla^2\psi(\mathbf{r}) + V\psi(\mathbf{r}) = \hat{\mathcal{H}}\psi(\mathbf{r}) = E\psi(\mathbf{r}). \tag{2.2}$$

Note that writing this time-independent expression requires the approach of separation of variables, whereby assumptions are made that $\Psi(\mathbf{r},t) = \psi(\mathbf{r})\phi(t)$ and that V has no time dependence. Here, E is an energy eigenvalue of the differential equation. For compactness, the above equation (or any eigenvalue equation) can be written with the operator $\hat{\mathcal{H}}$, the Hamiltonian, which captures all energetic effects acting upon $\psi(\mathbf{r})$. The first part of the Hamiltonian in Eq. 2.2, $-\frac{\hbar^2}{2m_e}\nabla^2$, captures the kinetic energy of the electron, while the remainder, V, relates to the potential energy due to, e.g., Coulombic interactions. Thus, the Hamiltonian is an "energy" operator for the electron, yielding its energy, E, as an eigenvalue.

2.1.2 Extending the Schrödinger Equation

Equations 2.1 and 2.2 have proven vital to the development of quantum mechanics. However, there are significant limits to the types of problems that can be solved exactly with them, particularly for systems containing multiple electrons. In such cases,

the so-called many-body Hamiltonian is used [59]:

$$\hat{\mathcal{H}} = -\frac{\hbar^2}{2m_e}\sum_i \nabla_i^2 - \sum_I \frac{\hbar^2}{2M_I}\nabla_I^2 + \frac{1}{2}\sum_{i\neq j}\frac{e^2}{|\mathbf{r}_i - \mathbf{r}_j|} - \sum_{i,I}\frac{Z_I e^2}{|\mathbf{r}_i - \mathbf{R}_I|} + \frac{1}{2}\sum_{I\neq J}\frac{Z_I Z_J}{|\mathbf{R}_I - \mathbf{R}_J|}. \quad (2.3)$$

Equation 2.3 has five distinct components, which we will briefly examine individually. The first term is the familiar kinetic energy of the electrons, generalized to the case of many electrons, each defined by an index i. Similarly, the second term describes the kinetic energy of nuclei, labeled by indices I and having mass M_I. The third term captures the Coulombic interactions between electrons i and j (excluding spurious self-interactions), with the product of both particles' charge ($-e$) in the numerator and the distance between them in the denominator. In the same way, the fourth term captures Coulombic interactions between electrons i and nuclei I, and the fifth term does so between nuclei I and J. Nuclei have charge $+Z_I e$, where Z_I is the number of protons in the nucleus, also known as the atomic number. The third and fifth terms are multiplied by factors of one-half to account for double-counting of interactions.

It is convenient and quite accurate for most systems to apply the Born-Oppenheimer approximation [60] to simplify the above expression. This approximation neglects the motion and, thus, kinetic energy of the nuclei, as their masses are considerably larger than those of the electrons. As a result, the second term in the Hamiltonian of Eq. 2.3 can be discarded, and the electronic and ionic (nuclear) components of the many-body expression can be decoupled. We can then express the remainder of Eq. 2.3 in a more compact operator form:

$$\hat{\mathcal{H}} = \hat{T} + \hat{V}_{\text{int}} + \hat{V}_{\text{ext}} + E_{II}, \quad (2.4)$$

where the subscript "int" refers to electon-electron interactions, "ext" refers to the external interaction of nuclei upon electrons, and E_{II} is the nuclear energy and is in-

dependent of electron positions. As the Hamiltonian is an energy operator, the total energy of the system can be expressed similarly as a sum of expectation values:

$$E = \langle \hat{\mathcal{H}} \rangle = \langle \hat{T} \rangle + \langle \hat{V}_{\text{int}} \rangle + \langle \hat{V}_{\text{ext}} \rangle + E_{II}. \tag{2.5}$$

While complete in its description of the physics of the many-body problem, solving the Schrödinger equation using the Hamiltonian of Eqs. 2.3 or 2.4 is, in practice, analytically intractable. With the position of electrons known only probabilistically, evaluating $\hat{V}_{\text{int}}$ and $\hat{V}_{\text{ext}}$ exactly is not possible. Aside from that, most systems contain enormous numbers of electrons, which only compounds the difficulty. For a system with N electrons, the Schrödinger equation is a partial differential equation with $3N$ dimensions, which is coupled with 2^N spin states. Integration on a grid with G points therefore requires $2^N G^{3N}$ total numbers of storage, meaning that the computational costs increase exponentially with the number of electrons. For a simple diatomic N_2 molecule, containing fourteen electrons, on the order of 10^{100} complex numbers would need to be stored, and containing that much data would require storage space orders of magnitude larger than the size of the Milky Way galaxy [61]. Fortunately, several breakthroughs in the field of density functional theory (DFT) have made it possible for these problems to be solved numerically with high accuracy. We will discuss several of these approximations and the theoretical pathway toward obtaining them in the following section.

2.2 Foundations of Density Functional Theory

2.2.1 Hartree-Fock Theory

One of the earliest theoretical frameworks with which to treat systems with many electrons was Hartree-Fock theory [62, 63], in which the many-body wavefunction is written as the product of single-electron wavefunctions. In order to obey the Pauli exclusion principle, which restricts identical fermions from occupying the same state, this many-body electronic wavefunction must be antisymmetric; i.e., for the two-particle case, $\Psi(\mathbf{r}_1, s_1, \mathbf{r}_2, s_2) = -\Psi(\mathbf{r}_2, s_2, \mathbf{r}_1, s_1)$. Here, s_1 and s_2 refer to the spins of the two particles. This requirement can be satisfied by writing the wavefunction as a Slater determinant of the single-electron wavefunctions [63, 64]. The resultant Hamiltonian has the following expectation value:

$$\langle \hat{\mathcal{H}}^{\mathrm{HF}} \rangle = \langle \hat{T} \rangle + \langle \hat{V}_{\mathrm{ext}} \rangle + U + J, \tag{2.6}$$

where U is the direct electron-electron interaction energy—also known as the Hartree energy—and J is the so-called "exchange" energy. (Refer to Section 3.5 in Ref. [59] for a more detailed derivation and explicit description of these terms.) The exchange energy, which acts only between electrons of the same spin and has a negative sign, accounts for Pauli exclusion. Both U and J contain spurious self-interaction terms; however, because these terms in U and J have opposite signs, they cancel one another.

Because the exchange energy always serves to lower the total energy, physicists often relate its effect to that of a fictitious positively charged particle, called the "exchange hole." The presence of this positively charged species interacting with electrons lowers the total energy via Coulombic attraction with exactly the same magnitude as the exchange term J. Hartree-Fock theory fails, however, to take into account

another term that serves to lower the energy, namely, correlation. Quite simply, the correlation energy is simply the remaining energy difference between the energetic sum in Eq. 2.6 and the real energy of the system. The physical meaning of correlation relates to the screening of charge brought about by various distributions of electrons, which, like exchange, serves to lower the total energy. Unfortunately, correlation cannot be calculated analytically, although numerical methods can be used to approximate it fairly accurately in certain cases, with Quantum Monte Carlo calculations serving as the gold standard in this realm [65]. The exchange and correlation energies are often grouped together as the "exchange-correlation energy" or E_{xc}, as will be discussed more in Sections 2.2.3 and 2.2.4.

2.2.2 Hohenberg-Kohn Theorems

Pierre Hohenberg and Walter Kohn laid the groundwork for DFT with the two Hohenberg-Kohn theorems, developed in 1964 [66]. Crucially, their work showed that the electron *density*, n, is directly related by way of a *functional* (a function of a function) to the exact total energy and, therefore, all properties of a system.

The two Hohenberg-Kohn theorems are as follows:

Theorem 1 *For a system of interacting particles under the influence of an external potential* $\hat{V}_{\text{ext}}(\mathbf{r})$*, the potential* $\hat{V}_{\text{ext}}(\mathbf{r})$ *is uniquely determined by the ground-state particle density* $n(\mathbf{r})$*, aside from a constant.*

Theorem 2 *Consider a functional* $E[n(\mathbf{r})]$ *relating energy to density, which is valid for any external potential* $\hat{V}_{\text{ext}}(\mathbf{r})$*. For a particular choice of* $\hat{V}_{\text{ext}}(\mathbf{r})$*, the minimum value of this functional is the exact ground-state energy, and the corresponding density* $n(\mathbf{r})$ *is the exact ground-state density,* $n_0(\mathbf{r})$*.*

This exact functional can be written simply as the sum of functionals capturing all kinetic and potential energy terms:

$$E_{\mathrm{HK}}[n(\mathbf{r})] = T[n(\mathbf{r})] + E_{\mathrm{int}}[n(\mathbf{r})]. \tag{2.7}$$

The proofs of these theorems are remarkably straightforward (see Ref. [66]), and their power cannot be understated. They show that one quantity—the ground-state electron density—is sufficient to understand all properties of a system in its entirety. However, the precise functional relating density and energy is not known; thus, approximations for it are needed.

2.2.3 The Kohn-Sham Ansatz

As the Hohenberg-Kohn theorems show, the electron density has tremendous predictive power for describing materials properties. However, direct calculations on the interacting system are extremely expensive. Walter Kohn and Lu Jeu Sham pioneered an approach that replaces the interacting system with an auxiliary, non-interacting system of particles [67]. The key Kohn-Sham *ansatz* requires that this auxiliary system has the same ground-state electron density as the full interacting system. Thus, calculations to determine ground-state properties can be performed on the auxiliary system, which has its own Hamiltonian with a Kohn-Sham potential that differs from that of the real system.

The Kohn-Sham energy can be written as:

$$E_{\mathrm{KS}}[n(\mathbf{r})] = T_s[n(\mathbf{r})] + \int d\mathbf{r} V_{\mathrm{ext}}(\mathbf{r}) n(\mathbf{r}) + E_{\mathrm{Hartree}}[n(\mathbf{r})] + E_{xc}[n(\mathbf{r})], \tag{2.8}$$

where T_s is the independent-particle kinetic energy, V_{ext} is the potential from nuclei and any external fields, and E_{II} is the energy due to nuclei-nuclei repulsion, as in Eq. 2.5. E_{Hartree} is the energy from Coulombic interaction of the electron cloud of density $n(\mathbf{r})$ interacting with itself, given by:

$$E_{\text{Hartree}}[n] = \frac{1}{2}\int\int d\mathbf{r}d\mathbf{r}'\frac{n(\mathbf{r})n(\mathbf{r}')}{|\mathbf{r}-\mathbf{r}'|}. \tag{2.9}$$

Note that this energy is not the same as $\langle\hat{V}_{\text{int}}\rangle$ in Eq. 2.5: $\langle\hat{V}_{\text{int}}\rangle$ captures the Coulomb energy of interacting, correlated electrons, while E_{Hartree} refers to the Coulomb energy in a fictitious, continuous charge density. Both, however, refer to systems with the same electron density, n.

Finally, $E_{xc}[n]$ is the exchange-correlation energy functional, mentioned previously. It can be written compactly as:

$$E_{\text{xc}}[n(\mathbf{r})] = \langle\hat{T}\rangle - T_s[n(\mathbf{r})] + \langle\hat{V}_{\text{int}}\rangle - E_{\text{Hartree}}[n(\mathbf{r})], \tag{2.10}$$

where $\langle\hat{T}\rangle + \langle\hat{V}_{\text{int}}\rangle$ is equal to the Hohenberg-Kohn energy functional E_{HK} defined in Eq. 2.7. This exchange-correlation energy perfectly captures the difference between the Kohn-Sham auxiliary system and the real system. Because the other terms in Eq. 2.8 are straightforward to calculate for a non-interacting system, knowing E_{xc} would allow for calculations of the real energy. Unfortunately, it is not known exactly, but adequate approximations exist that make the Kohn-Sham approach highly useful for calculations.

2.2.4 Exchange-Correlation Functionals

Approximating the exchange-correlation functional has become one of the premier tasks for those looking to improve the accuracy of DFT calculations. Kohn and Sham paired their eponymous procedure with a description of the first approximate functional, wherein exchange and correlation were considered to be local properties of systems approximated as a uniform electron gas [67]. Due to the simple analytic form of exchange and the accurate approximations to correlation for such a gas, this approximation was straightforward to implement. The local nature of this approximation gave rise to its name: the "local density approximation" (LDA)—or, if considering spin, the "local spin density approximation" (LSDA). The L(S)DA proved to be successful for calculating materials properties, particularly for simple metals, which most closely approach the electron density of the homogeneous electron gas, and it can be easily parameterized for calculations [65, 68, 69].

As research in the field progressed, new functionals were developed with the goal of producing results closer to the threshold of "chemical accuracy," defined as energies within 1 kcal/mol (0.0434 eV) of the real result. John Perdew and Karla Schmidt referred to the development of functionals as a sort of "Jacob's ladder" of chemical accuracy, whereby functionals based on increasingly more accurate approximations climb toward that ultimate, "heavenly" goal [70]. Unquestionably, the most popular rung of the latter remains that of the generalized gradient approximation (GGA), which accounts for the non-homogeneity of the electron gas by including a dependence on the spatial gradient of electron density [71]. GGA functionals, in particular that developed by Perdew, Burke, and Ernzerhof (PBE) [72], remain ubiquitous due to their low computational cost and superior accuracy compared to the L(S)DA. While L(S)DA tends to underestimate the lattice spacing in materials, GGA functionals tend

to overestimate the lattice spacing, but generally produce values closer to those measured in experiments. However, both L(S)DA and GGA tend to underrepresent significantly the band gap of semiconductors due to their self-interaction terms (often incorrectly predicting small-gap materials to be metals), and they and perform poorly for predicting various other electronic properties, including the localization of charge [73].

Many other functionals have been developed to circumvent the problems of these mostly local functionals with varying degrees of success. For information about functionals in the realm of meta-GGAs, orbital-dependent functionals, and others, the reader is referred to Refs. [61] (Ch. 3), [74] (Ch. 5), and [75] (Ch. 4). In this thesis, the functionals of most interest will be the so-called "hybrid" functionals. Such functionals were designed with the explicit aim of correcting the shortcomings of GGA functionals, and they traditionally maintain a portion of GGA exchange and correlation. However, to correct the problem of underestimating the band gap in semiconductors, these functionals mix GGA approaches with orbital-dependent Hartree-Fock exchange energy. In doing so, they combine the Hartree-Fock approach's exact treatment of exchange with the description of correlation in GGA functionals [76]. Most common is the PBE0 functional, based upon the original PBE GGA functional. The exchange-correlation energy for PBE0 can be written as [77]:

$$E_{xc}^{\mathrm{PBE0}} = aE_x^{\mathrm{HF}} + (1-a)E_x^{\mathrm{PBE}} + E_c^{\mathrm{PBE}}. \tag{2.11}$$

The term a is the mixing parameter determining how much Hartree-Fock exchange is substituted for that of the PBE GGA functional. It is most typical to set $a = 1/4$, which follows from various physical arguments [77, 78].

The work in this thesis will be primarily based upon the hybrid functional of Heyd, Scuseria, and Ernzerhof (HSE). It is similar in spirit to PBE0; however, it uses a screened Coulomb potential to calculate exchange, thus removing the long-range component of the Hartree-Fock energy and restricting the range over which the exchange hole (see Section 2.2.1) can be delocalized [79]. In similar fashion to Eq. 2.11, the exchange-correlation energy for HSE can be written as:

$$E_{xc}^{\mathrm{HSE}} = aE_x^{\mathrm{HF,SR}}(\omega) + (1-a)E_x^{\mathrm{PBE,SR}}(\omega) + E_x^{\mathrm{PBE,LR}}(\omega) + E_c^{\mathrm{PBE}}, \tag{2.12}$$

where the superscripts "SR" and "LR" denote "short-range" and "long-range" components, respectively. HSE introduces a screening parameter, ω, to dictate the extent of short-range interactions included in the energy. This approach is significantly more accurate than that of other functionals for structural and electronic properties, for both metals and semiconductors [80]. Due to the need for high accuracy in the work presented here, HSE (specifically, the updated version HSE06[81]) with $a = 1/4$ and $\omega = 0.2$, will be the functional of choice.

2.2.5 Pseudopotentials

One additional crucial topic for DFT calculations is that of pseudopotentials, which provide more efficient ways to model specific atoms in a material. In atoms, electrons can be divided into two categories: core electrons, which are relatively close to the nucleus, and valence electrons, which are further from the nucleus. The core electrons are tightly bound to the nucleus, while valence electrons are free to interact with those of other atoms to form bonds. In a solid, the wavefunctions of valence electrons vary smoothly and are perturbed by the nuclei and strongly-bound core electrons. Therefore, the valence wavefunctions can be efficiently expanded in a plane-wave basis [82].

However, core electrons tend to exhibit large oscillations in their wavefunctions, making it prohibitive to capture them with plane waves (for the example of silicon, which has ten core electrons, on the order of 10^5 plane waves would be needed simply for these core states) [83]. To circumvent this problem, core states are typically described with an effective potential, allowing valence electrons to be treated explicitly with a plane-wave expansion [82, 84]—this approach defines what is meant by a "pseudopotential." Considering the large numbers of core electrons in many atoms, using pseudopotentials has been immensely successful in calculating materials properties.

Many methods for constructing pseudopotentials exist, dating back to the work of Enrico Fermi on electron and neutron scattering [85, 86]. One early advance was in the orthogonalized plane wave (OPW) technique, which modeled valence electrons with a plane-wave expansion orthogonal to the wavefunctions of the core states [87]. This approach accurately captured the behavior of electron wavefunctions far from the core, while replacing the oscillatory all-electron wavefunction near the core with a smoother pseudo wavefunction. The OPW approach allowed for the generalization of pseudopotentials to model different systems. However, the utility of OPWs is limited by the fact that they are generally too repulsive at their core (displaying so-called "hard core" character), and outside of the core region, while they show the correct shape, they differ by a normalization factor from the actual wavefunction [88].

Subsequently, empirical pseudopotentials, designed to reproduce known properties of materials, became popular, as they showed exceptional promise for calculating properties of more complex compounds [84]. These pseudopotentials assume a particular functional form, with parameters determined through fitting with experimentally obtained data. Therein, however, lies the limitation of the empirical pseudopotential method: their construction is reliant on the availability of experimental data, placing them in stark constrast to *ab initio* pseudopotentials.

A key requirement of pseudopotentials was laid out in the work of Hamann, Schlüter, and Chiang [89] in the form of norm conservation. A "norm-conserving" pseudopotential is divided into two distinct spacial regions by the core radius, R_c. For $r > R_c$, the pseudopotential agrees with the all-electron wavefunctions, which in that region are smooth and can be well-described with a plane-wave expansion. For $r < R_c$, however, the pseudopotential approach replaces the complex core wavefunction with a smooth function that is easier to treat computationally and has the same integrated charge. In other words, if we consider the all-electron wavefunction $\psi(r)$ and pseudo wavefunction $\psi^P(r)$, the following condition must hold:

$$\int_0^{R_c} |\psi(r)| r^2 dr = \int_0^{R_c} |\psi^P(r)| r^2 dr = Q, \tag{2.13}$$

where Q is the total charge within $r < R_c$ for the real system. Additionally, pseudo wavefunctions and their derivatives are required to be continuous at R_c.

However, replacing this central part of the wavefunction necessarily limits the accuracy of any pseudopotential approach. For this reason, projector augmented wave (PAW) pseudopotentials have been widely adopted. Within the PAW approach, auxiliary localized functions are introduced that are related to the real all-electron wavefunctions via linear transformation [90]. These auxiliary functions are constructed so as to be smooth and readily integrable.

Expressed mathematically, the all-electron wavefunction is written in the PAW formalism as:

$$|\Psi\rangle = |\tilde{\Psi}\rangle + \sum_i c_i (|\phi_i\rangle - |\tilde{\phi}_i\rangle), \tag{2.14}$$

where $|\Psi\rangle$ is the full wavefunction, $|\tilde{\Psi}\rangle$ is the smooth pseudo wavefunction, $|\phi_i\rangle$ and $|\tilde{\phi}_i\rangle$ are partial wave components of the wavefunctions, and c_i are linear coefficients.

Because the transformation between the all-electron wavefunction and the pseudo wavefunction is linear, these coefficients can be determined by the inner product of the smooth pseudo wavefunction $|\tilde{\Psi}\rangle$ and the projection operators $\tilde{p}_i$, which are chosen to be orthogonal to the smooth pseudo wavefunctions $|\tilde{\phi}_i\rangle$ (i.e., $\langle \tilde{p}_i | \tilde{\phi}_{i'} \rangle = \delta_{ii'}$).

The primary advantage of PAWs is that they retain the information of the all-electron wavefunction, including the core electron states, leading to improved computational accuracy [91]. In addition, the use of smooth auxiliary functions means that fewer plane waves are needed for the plane-wave expansion. In the work discussed in this thesis, PAW pseudopotentials will be utilized to describe each type of atom.

2.3 Defects in Materials

The materials scientist Colin Humphreys once wrote: "Crystals are like people: it is the defects in them that tend to make them interesting!" [92] He was correct: point defects play a pivotal role in a number of properties that make semiconductors and insultors technologically useful. Studying how they form and what properties they convey is vital to a complete understanding of any crystalline material. What follows is a brief summary of the point defect formalism used throughout this thesis, following principally from the work of Freysoldt *et al*. [93]

2.3.1 Point Defects

Traditionally, materials scientists have concerned themselves with two broad categories of defects: extended defects, which include grain boundaries and dislocations, and point defects, which tend to involve one or two particular atoms in a material.

Both are critical for materials operation. However, extended defects are particularly onerous to examine from an *ab initio* approach, as their size is difficult to take into account in simulation cells, which have periodic boundaries in most DFT codes. Point defects, however, are more easily captured within a DFT calculations. They have been shown to be responsible for wide-ranging phenomena, including mass transport [94], electrical conductivity [95], carrier recombination [96, 97], and optical properties [98, 99], among many others.

There are three primary types of point defects: vacancies, interstitials, and substitutional defects. Vacancies are formed where an atom is missing from the periodic crystal lattice. We will denote vacancies as V_{A}, with A being the chemical identity of the atom absent from the crystal. Interstitials represent effectively the opposite condition, namely, an extra atom inserted into the lattice. The notation we will use for an interstitial species of element A is A_i. Substitutional species are formed where one type of atom is found occupying the lattice site for a different species, for example, a gallium atom substituting on an arsenic site in GaAs, which would be denoted as $\mathrm{Ga}_{\mathrm{As}}$. Defects can also form collectively as complexes [see Section 2.4.2 for more details], which, when limited to no more than a few atoms, can be treated computationally within the same formalism as isolated point defects.

Impurities, intentional or otherwise, can also be treated as point defects. It is common for materials to contain some foreign contaminants, which may be unintentionally incorporated during growth or added intentionally to introduce a desired property. Impurities that are added intentionally are often called dopants. In the case of GaAs, for instance, magnesium could substitute on the gallium site ($\mathrm{Mg}_{\mathrm{Ga}}$). Because magnesium has two valence electrons, one fewer than gallium, this defect will tend to attract an additional electron, making it an electron "acceptor." Such a charged defect can be labeled with its charge as a superscript, i.e., $\mathrm{Mg}_{\mathrm{Ga}}^{-}$. Similarly, a posi-

tively charged defect would be called an electron "donor." Impurities can also form as interstitials: in one significant example, H_i has been demonstrated to be a source of unintentional n-type conductivity in ZnO [100]. Whether or not an impurity can incorporate into a given crystal lattice, and in what configuration, depends on both the material and its synthesis conditions, as will be discussed subsequently.

2.3.2 Formation Energy in Supercells

As noted, most DFT codes use periodic boundary conditions, meaning that if a defect is added to a single unit cell, it will interact strongly with its periodically repeated images. Furthermore, particularly for small unit cells, the defect concentrations being simulated in this manner would be unrealistically high; typical defect concentrations are on the order of a few atom percent, which cannot be captured in most unit cells. To address these problems, one can make use of supercells, which maintain the same material structure but are much larger in size (often on the order of a few hundred atoms), thereby permitting accurate studies of defects in the dilute limit.

The formation energy of a point defect D in charge state q, $E^f(D^q)$, is calculated as [93]

$$E^f(D^q) = E(D^q) - E_{\text{bulk}} + \sum n_{\text{A}}\mu_{\text{A}} + qE_F + \Delta_{\text{corr}}. \tag{2.15}$$

Here, $E(D^q)$ represents the total energy of a supercell containing defect D in charge state q; E_{bulk} is the total energy of a supercell containing no defects; n_{A} represents the number of atoms of species A added ($n_{\text{A}} < 0$) or removed ($n_{\text{A}} > 0$); μ_{A} is the chemical potential of species A in a theoretical external reservoir; E_F is the Fermi level, which is a variable with values ranging from the valence-band maximum (VBM) to the conduction-band minimum (CBM); and Δ_{corr} is a finite-size correction term. The concentration of a point defect is related to its formation energy by a Boltzmann rela-

tion; namely,

$$c(D^q) = N_{\text{sites}} \exp\left(-\frac{E^f(D^q)}{k_B T}\right), \tag{2.16}$$

where N_{sites} is the number of available sites for the defect and k_B is the Boltzmann constant. Clearly, smaller formation energies lead to larger defect concentrations, exponentially so; for this reason, it is typically a good approximation to focus solely on the lowest-energy defects at any particular value of E_F.

The correction term Δ_{corr} is needed to calculate formation energies for charged defects. Even for supercells, periodic boundary conditions still lead to spurious electrostatic interactions between such defects and their periodically repeated images in neighboring cells. Increasing the size of the supercell can lead to a more accurate result; however, doing so will also increase the computational expense, which is particularly undesirable when using a hybrid functional. Currently, the preferred approach to produce accurate formation energies is the use of an *a posteriori* term to correct for the self-interaction error. In this work, Δ_{corr} will be calculated based on the work of Freysoldt *et al*. [101, 102], whose approach has been demonstrated to outperform several other proposed correction techniques [103].

2.3.3 Chemical Potentials

The chemical potentials μ_{A} from Eq. 2.15 are variables that must be carefully chosen so as to represent experimental conditions. They correspond to the energies of atoms in an external reservoir with which the components of defects or impurities are exchanged. For example, in forming an oxygen vacancy, the chemical potential of oxygen is included in the formation energy to indicate an energy increase corresponding to the addition of one oxygen atom to that external reservoir—this energy increase is the chemical potential of oxygen.

These chemical potentials can be written as the sum of two terms,

$$\mu_{\mathrm{A}} = E_{\mathrm{A}} + \Delta\mu_{\mathrm{A}}, \tag{2.17}$$

where E_{A} is the total energy of element A in its lowest-energy elemental form, while $\Delta\mu_{\mathrm{A}}$ is the deviation from that energy. E_{A} is calculated with DFT as the total energy per atom of the reference phase: for many elements, such as calcium or strontium, this phase is the ground-state elemental phase, while for an element such as oxygen or hydrogen, the reference phase is the diatomic moleculer ground state, O_2 or H_2. Bounds are placed on these $\Delta\mu_{\mathrm{A}}$ values by the thermodynamic stability condition for the compound of interest, along with the limits imposed by competing phases. These limits require knowledge of the compounds' enthalpies of formation, which can be calculated using DFT. For an arbitrary compound $\mathrm{A}_x\mathrm{B}_y\mathrm{C}_z$, the enthalpy of formation is calculated as follows:

$$\Delta H^f(\mathrm{A}_x\mathrm{B}_y\mathrm{C}_z) = E_{\mathrm{A}_x\mathrm{B}_y\mathrm{C}_z} - xE_{\mathrm{A}} - yE_{\mathrm{B}} - zE_{\mathrm{C}}. \tag{2.18}$$

The terms on the right-side of the equation refer to total energies calculated in DFT. Note that DFT intrinsically calculates ground-state properties, that is, with $T = 0$ K. Thus, the enthalpy of formation is also equivalent to the Gibbs free energy in these calculations, as the entropic term is zero at $T = 0$ K [93].

Values for $\Delta\mu_{\mathrm{A}}$ can be correlated to quantities that are readily controlled in experiments. For gaseous substances, $\Delta\mu_{\mathrm{A}}$ is related to experimental temperatures and partial pressures through the following expression:

$$\Delta\mu_{\mathrm{A}} = H^0(T) - TS^0(T) + RT\ln\frac{p_{\mathrm{A}}}{p^0}, \tag{2.19}$$

where $H^0(T)$ and $S^0(T)$ are tabulated for gases such as H_2, O_2, N_2, and H_2O [104], p_A is the partial pressure, and p^0 is the pressure at the standard conditions used in the tabulation. Relating chemical potentials to measurable properties for elements with solid reference phases is more challenging. Where those chemical potentials are concerned, the best way to refer to them is by discussing element-"rich" or -"poor" conditions, corresponding to a relative abundance of that particular element. That is, for example, calcium-rich conditions would indicate an energetic preference for calcium incorporation, while calcium-poor conditions would indicate the opposite. Experimentally, these conditions could be related to an overabundance (element-rich) or lack (element-poor) of the element in question.

Binary Compounds

Chemical potential stability regions are best understood through examples. Most straightforward are binary compounds, such as BaH_2. Thermodynamic equilibrium restricts the values of $\Delta\mu_{Ba}$ and $\Delta\mu_H$ as follows:

$$\Delta\mu_{Ba} + 2\Delta\mu_H = \Delta H^f(BaH_2). \tag{2.20}$$

In a binary compound, the only other chemical potential restrictions are those that prevent elemental phases from forming:

$$\Delta\mu_{Ba} \leq 0, \tag{2.21}$$

$$\Delta\mu_H \leq 0. \tag{2.22}$$

Using these conditions, it is possible to plot a phase stability diagram for BaH_2 in two-dimensional chemical potential space as a function of $\Delta\mu_{Ba}$ and $\Delta\mu_H$.

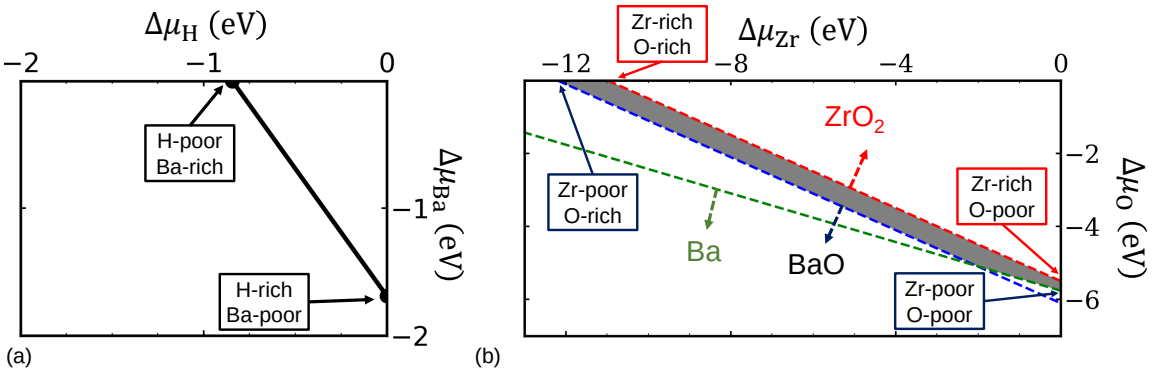

Figure 2.1: Chemical potential stability diagrams for (a) BaH_2 and (b) $BaZrO_3$. In (a), the stability region is the line segment, while in (b), the stability region is shaded gray. In (a), H-poor (Ba-rich) and H-rich (Ba-poor) conditions are labeled with arrows. In (b), Zr-poor/O-rich, Zr-poor/O-poor, Zr-rich/O-rich, and Zr-rich/O-poor conditions are labeled. Panel (b) also indicates regions in which the limiting phases ZrO_2 and BaO will form.

This diagram is shown in Fig. 2.1(a), using $\Delta H^f(BaH_2) = -1.69$ eV, determined using Eq. 2.18 and calculated total energies. The stable region is simply the line segment corresponding to Eq. 2.20, bounded by equilibrium with elemental materials ($\Delta\mu_{Ba} = 0$, Ba-rich, and $\Delta\mu_H = 0$, H-rich). The boundaries of this region are labeled to indicate different combinations of H-rich/H-poor and Ba-rich/Ba-poor conditions that can be used to map the defect physics comprehensively. Any set of chemical potentials between those two limits can be used to calculate defect formation energies under conditions of stability.

Ternary Compounds

The situation for ternary compounds is slightly more complex. However, stability regions can still be plotted in two dimensions at thermodynamic equilibrium. As an example, consider $BaZrO_3$, for which thermodynamic equilibrium is set by:

$$\Delta\mu_{Ba} + \Delta\mu_{Zr} + 3\Delta\mu_O = \Delta H^f(BaZrO_3). \tag{2.23}$$

This condition sets one constraint on the three chemical potential variables, permitting the other two to be plotted easily.

In the case of $BaZrO_3$, stability is limited by certain binary compounds, namely,

$$\Delta\mu_{\mathrm{Ba}} + \Delta\mu_{\mathrm{O}} \leq \Delta H^f(\mathrm{BaO}), \tag{2.24}$$

$$\Delta\mu_{\mathrm{Zr}} + 2\Delta\mu_{\mathrm{O}} \leq \Delta H^f(\mathrm{ZrO_2}). \tag{2.25}$$

The limits on elemental phases also persist:

$$\Delta\mu_{\mathrm{Ba}} \leq 0, \tag{2.26}$$

$$\Delta\mu_{\mathrm{Zr}} \leq 0, \tag{2.27}$$

$$\Delta\mu_{\mathrm{O}} \leq 0. \tag{2.28}$$

By combining Eqs. 2.24 and 2.26 with the condition on $\Delta\mu_{\mathrm{Ba}}$ imposed by Eq. 2.23, $\Delta\mu_{\mathrm{Ba}}$ can be replaced:

$$\Delta\mu_{\mathrm{Zr}} + 2\Delta\mu_{\mathrm{O}} \geq \Delta H^f(\mathrm{BaZrO_3}) - \Delta H^f(\mathrm{BaO}), \tag{2.29}$$

$$\Delta\mu_{\mathrm{Zr}} + 3\Delta\mu_{\mathrm{O}} \geq \Delta H^f(\mathrm{BaZrO_3}), \tag{2.30}$$

which maps the limiting condition onto $\Delta\mu_{\mathrm{Zr}}$–$\Delta\mu_{\mathrm{O}}$ space.

The stability region for $BaZrO_3$ is shown in Fig. 2.1(b). In this particular case, the stability region is no longer merely a line. It is bounded by the conditions expressed in Eqs. 2.25, 2.29, and 2.30, which are labeled, as well as the elemental phase limits for oxygen and zirconium. As in the case of binary compounds, the stability region allows for identification of certain chemical potential limits. It is most obvious to express these in terms of the chemical potential terms used on the two axes (i.e., O-rich/poor

and Zr-rich/poor); however, if one assumes for instance that $\Delta\mu_O$ is fixed, it follows from Eq. 2.23 that Zr-rich conditions are equivalent to Ba-poor conditions (similarly for Zr-poor and Ba-rich). In this case, it is reasonable to assume a certain value of $\Delta\mu_O$, as that value is most closely tied to experimentally-controlled conditions, and then refer to differences between Zr-rich (Ba-poor) and Zr-poor (Ba-rich) conditions for that specific choice.

Quaternary Compounds

Stability regions can be defined for quaternary compounds. However, in following the same procedure as for ternary compounds, it is clear that three of the four variables can vary freely, even after invoking thermodynamic stability. One can plot chemical stability in three dimensions; however, for the sake of presentation, it is often easier to treat one variable as a fixed parameter, once more allowing plots to be shown in two dimensions. The variable to be fixed can be chosen to correspond to a species (i.e., N, O, or H) that is most readily related to an experimentally measured partial pressure. This approach is discussed in full in Appendix A as pertains to the La/Sr-based oxyhydrides and the nitride hydride Sr_2LiH_2N.

Impurity Chemical Potentials

When extrinsic species are introduced, it is necessary to define an additional chemical potential. In doing so, one must consider the additional limiting phases most likely to form upon introduction of the new element. For example, in the case of BaH_2, the addition of potassium (K) would necessitate the definition of $\Delta\mu_K$. As before, $\Delta\mu_K \leq 0$ in order to prevent the precipitation of metallic sodium. Additionally, the most energetically favorable phase containing K and Ba and/or H must be consid-

ered. In this case, that phase is KH. Preventing the formation of KH requires that:

$$\Delta\mu_{\mathrm{K}} + \Delta\mu_{\mathrm{H}} \leq \Delta H^f(\mathrm{KH}). \tag{2.31}$$

$\Delta\mu_{\mathrm{H}}$ is determined by the chemical potential conditions under investigation (i.e., Ba-rich/H-poor or Ba-poor/H-rich, as defined in Fig. 2.1). For convenience, it is common to assume the upper bound for Eq. 2.31 to set a value for $\Delta\mu_{\mathrm{K}}$: this position represents the solubility limit for K in BaH_2.

Note that the limiting phase may be dependent on the choice of, e.g., H-rich or H-poor conditions. For the materials under examination in this thesis, that will be uncommon; however, in general, one must be careful to account for all possible limiting phases when introducing an impurity.

2.3.4 Plotting Defect Formation Energies

Once the atomic chemical potentials are fixed (e.g., by using one of the conditions indicated in Fig. 2.1), one can plot defect formation energies. The traditional approach to do so involves selecting the Fermi level, E_F, as the free variable, which can vary from the VBM to the CBM. Then, the lowest-energy charge state is plotted for each defect within that range of E_F.

This approach is summarized schematically for a defect D^q in Fig. 2.2. In panel (a), the various charge states ($q = +1$, 0, and -1) for D^q are plotted for all E_F. It is clear from Eq. 2.15 that defect formation energy varies linearly with E_F; thus, each of these charge states are lines with slopes equal to the charge state. As defect concentration increases exponentially with formation energy (see Eq. 2.16), the lowest-energy lines (shown with solid black lines in Fig. 2.2(a)) are most pertinent at any given value of E_F. Charge-state transition levels are located at the intersections of these lines, where

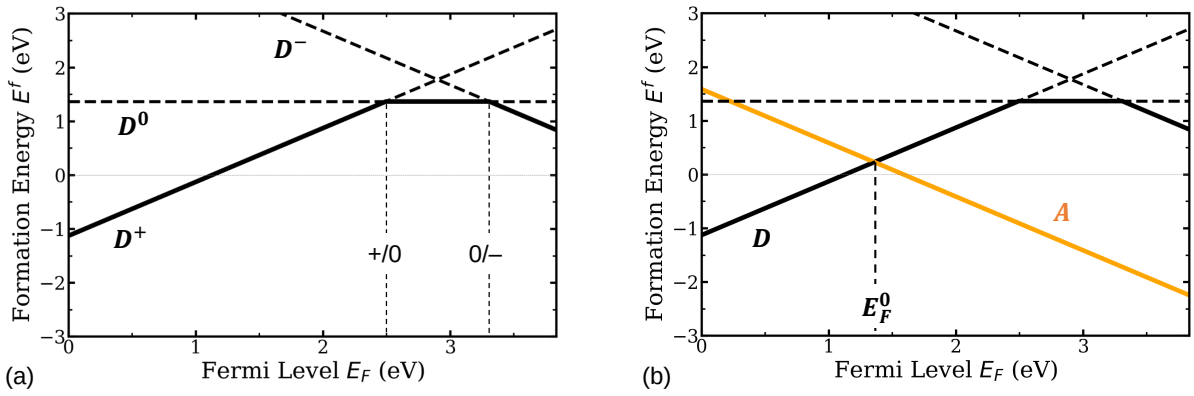

Figure 2.2: (a) Schematic formation energy diagram for a defect D^q, with charge states $q = +1$, 0, and -1. Charge-state transition levels are labeled and indicated with dashed vertical lines. The energetic hull of D is shown in solid black lines, indicating which charge states are preferred at different positions of the Fermi level. (b) The same defect as in panel (a) accompanied by a negatively charged defect A, colored orange. The position of the Fermi level to satisfy charge neutrality is indicated with a vertical dashed line labeled E_F^0.

the favored charge state changes. These positions can be very important for defects that act as recombination centers or traps.

One important result of a defect formation energy diagram is the position of E_F at which charge neutrality is established, which is determined by the lowest-energy positively and negatively charged defects. In Fig. 2.2(b), the species D is accompanied by another defect, A. This second defect is found only in the -1 charge state within the band gap and has a lower formation energy than D^-. Thus, charge neutrality will be achieved at the intersection labeled E_F^0 and marked with a vertical dashed line. One can also say that the Fermi level is "pinned" at this location. Of course, charge neutrality must cover all defects in a system, not simply those with the lowest formation energy; however, we make the approximation that higher energy defects need not be considered due to their exponentially higher concentration (see Eq. 2.16).

If A were not present, as in Fig. 2.2(a), charge neutrality would occur between the range of $\varepsilon_{+/0}$ and $\varepsilon_{0/-}$, where the lowest energy defect is neutral (D^0).

In defect engineering, it is often desirable to introduce an extrinsic species (i.e., a dopant) with a low enough formation energy so as to move the Fermi level. This strategy can lower the formation energies of useful defects and is particularly valuable in the case of hydrogen electrolytes, as will be seen in subsequent chapters.

2.4 Diffusion and Conductivity in Materials

Ionic conductivity in an electrolyte depends on both the formation energy of mobile charge carriers as well as their energetic migration barrier, E_b, for diffusion. As discussed in Section 2.3.2, the concentration, c, is exponentially related to the formation energy E^f via Eq. 2.16. The diffusivity, D, can be expressed as

$$D(T) = D_0 \exp\left(-\frac{E_b}{k_B T}\right), \tag{2.32}$$

with D_0 given by

$$D_0 \approx \alpha \nu a^2 \exp\left(\frac{\Delta S}{k_B}\right). \tag{2.33}$$

α is a geometry-related factor that is often close to unity; ν is a hopping frequency that can be approximated as 10^{13} s^{-1}, close to a typical phonon frequency; a is the distance between sites; and ΔS is an entropy term [105]. The ionic conductivity, σ, is then related to the defect concentration and the diffusivity via the Nernst-Einstein equation [106]:

$$\sigma = \frac{cDe^2}{k_B T} = \frac{D_0 e^2 N_{\text{sites}}}{k_B T} \exp\left(-\frac{(E^f + E_b)}{k_B T}\right), \tag{2.34}$$

where the activation energy is given as

$$E_a = E_b + E^f. \tag{2.35}$$

We have already described how to calculate E^f. E_b can also be determined using DFT, using a theoretical framework based on harmonic transition state theory (hTST) [107]. For a mobile species, E_b is the energetic barrier for the minimum energy path (MEP) connecting two energetic minima, the initial and final states of the diffusion process. Intermediate configurations along the MEP are identified by reaction coordinates, a measure of progression along the pathway adopted from the terminology of chemistry. As shown in Eq. 2.32, E_b determines the rate at which the species travels between the initial and final states. According to hTST, these states lie at energetic minima on a potential energy surface, which are separated by a unique saddle point. The MEP passes through this saddle point, which is E_b higher in energy than the initial point. The theoretical treatment by Vineyard in Ref. [107] provides the mathematical framework necessary for calculating diffusion rates on this potential energy surface, and his work provides the theoretical foundation for the nudged elastic band (NEB) method commonly used for DFT calculations of defect mobility.

2.4.1 The Nudged Elastic Band Method

The NEB method is one of the most successful first-principles approaches for determining migration barriers for bulk and surface processes [108–110]. As input, a user needs simply to provide a series of interpolated configurations, or "images," linking the relaxed initial and final states for the diffusion process under analysis. NEB will relax these images in tandem to locate the MEP. The energy difference between the initial state and the highest energy intermediate image is the migration barrier E_b. NEB

is quite proficient at locating the true saddle point configuration along the MEP; ergo, it is a very effective method for evaluating E_b.

There are several key features of NEB that make it particularly effective. For one, the images are joined by spring-like forces, which provide repulsive interactions when the images become too close to one another and attractive interactions when the images are far apart (hence, the process is "elastic") [111]. The total energy calculations for intermediate images provide the potential energy surface needed to calculate additional forces. The total forces—from the spring-like link between images and from the potential energy surface—are minimized through Verlet integration to direct the system to convergence. Another important feature in NEB is that only certain components of the forces are used for minimization, in a process known as "nudging;" for details, we direct the reader to Ref. [110]. For the work described in this thesis, we will rely upon climbing image NEB (CI-NEB), an improved version of the algorithm wherein the image corresponding to the saddle point is freed from spring forces and thereby allowed to converge to the exact saddle point [112].

2.4.2 Binding Energy

In many materials, defects form as clusters, often bound together by Coulombic attraction. For ionic conduction to proceed, it may be necessary to break apart such complexes. To do so, the mobile species must overcome a Coulombic binding energy, given in the following expression for a complex between defects D_1^p and D_2^q:

$$E_{\text{bind}}([D_1D_2]^{p+q}) = E^f(D_1^p) + E^f(D_2^q) - E^f([D_1D_2]^{p+q}). \tag{2.36}$$

In the above definition, a positive value for the binding energy indicates that the complex is bound. A negative value for the binding energy, on the other hand, implies

that the complex will spontaneously dissociate into its component pieces and cannot be stabilized. When using dopants to introduce additional carriers in an ionic conductor, the binding energy between dopants and mobile ionic species must be carefully considered, as a positive binding energy will make ionic diffusion more difficult. This topic will be pertinent in the subsequent two chapters.

2.5 Calculation Details

The power of DFT is in its ability to model complex, quantum-mechanical phenomena in a computationally tractable fashion. A number DFT codes are available; however, the work presented in this thesis makes exclusive use of the Vienna *Ab initio* Simulation Package (VASP), a powerful and flexible code that has become one of the most popular in the field [113]. Throughout, the HSE06 hybrid functional is used, with exceptions for most NEB calculations, which make use of the less-expensive PBE GGA functional to lower computational costs. PAW pseudopotentials, provided through VASP, are used to simulate different atomic species; the specific electronic configurations of these pseudopotentials (i.e., which electrons are treated as valence states) will be identified in each chapter.

Chapter 3

Defects and Chemical Stability in the Alkaline-Earth Zirconates

3.1 Permissions and Attributions

The content of Chapter 3 follows from work that has previously appeared in ACS Applied Energy Materials (Ref. [114]) and in Physical Chemistry Chemical Physics (Ref. [115]). This work was performed in collaboration with Drs. Leigh Weston and Michael Swift. The formation energy results presented on the cerates ($SrCeO_3$ and $BaCeO_3$), along with formation enthalpies for the cerates and CeO_2, were obtained from calculations performed by Michael Swift.

3.2 Overview of Proton-Conducting Oxides

As mentioned in Chapter 1, proton-conducting oxides (PCOs) are the most widely studied solid-state hydrogen electrolytes. Most PCOs are perovskite oxides of the form ABO_3, with either cubic or orthorhombic crystal structures. Of these, barium

zirconate, $BaZrO_3$ (BZO), is regarded as the best proton-conducting oxide in terms of chemical stability [20, 21, 23]. Its related compounds, calcium zirconate, $CaZrO_3$, (CZO) and strontium zirconate, $SrZrO_3$ (SZO), have also attracted interest as proton conductors [116], and CZO has been adopted for use in commercial hydrogen gas sensors [23, 117, 118]. These materials are readily compared with the cerates, specifically barium cerate, $BaCeO_3$ (BCO), and strontium cerate, $SrCeO_3$ (SCO), which also offer high ionic conductivity [119, 120]. BCO, in particular, is commonly cited as the most conductive PCO, although its stability is a concern [121, 122]. The crystal structures and methods of ionic conduction are similar for both categories of materials. Indeed, the similarities permit alloying between compounds of different families, and it has been suggested that $Ba\{Ce,Zr\}O_3$ alloys offer an optimal combination of stability and ionic conductivity for devices [120, 123–125]. Previous first-principles studies have examined some of the intrinsic and extrinsic defect properties of the alkaline-earth zirconates [126–132] and cerates [133, 134].

Protons are incorporated into PCOs by creating oxygen vacancies during synthesis and then exposing to water, leading to the reaction [23]:

$$V_{\mathrm{O}}^{+2} + \mathrm{H_2O} \rightarrow 2\mathrm{H}^{+}. \tag{3.1}$$

The as-grown material therefore needs to contain a high concentration of oxygen vacancies. However, other species, such as cation antisite defects or self-interstitials, could form as the dominant donor species and, in the process, suppress the formation of oxygen vacancies. As such, oxygen vacancies must have lower defect formation energies than any other donor species in PCOs.

Assuming that oxygen vacancies are the dominant donor species, extrinsic impurities that act as acceptor dopants are needed to promote their formation. Trivalent

group-IIIB metals such as Sc and Y are most commonly used [23]. When substituting on the tetravalent Zr site, these elements act as acceptors. However, there is some probability that they will incorporate on the divalent *A* (Ca, Sr, or Ba) site, where they act as donors, thus suppressing the intended formation of oxygen vacancies—such "wrong-site" incorporation was previously found to be problematic in SZO [135]. On the other hand, monovalent elements such as the alkali metals should act as acceptors when substituting for the *A*-site cation. Notably, some studies have reported that alkali metals such as K and Rb can enhance proton conductivity in BZO [131, 132, 136, 137]. On the oxygen site, carbon and nitrogen are candidate acceptors. It is also important to consider these elements because they are commonly present during synthesis and device operation. Carbon, in particular, has been cited as contributing to the low stability of the cerates with respect to CO_2.

In this chapter, we analyze the properties of native point defects, including vacancies, cation antisite defects, and self-interstitials. We find that cation antisite species (Zr_{Ca} and Ca_{Zr}) are low in energy in CZO. Under Zr-rich conditions, they also form in SZO. Thus, doping CZO with acceptors will not lead to formation of oxygen vacancies; rather, Zr_{Ca} antisite defects will form. In SZO, Sr-rich conditions are necessary to create oxygen vacancies preferentially.

Next, we examine acceptor doping by studying substitution on the *A*, *B*, and O lattice sites. For the alkali metals, and for carbon and nitrogen, we additionally consider incorporation on interstitial sites. We explicitly verify that alkali-metal incorporation on the *A* site (as opposed to the *B* site) is preferred. Alkali-metal interstitials will form as donors; however, their formation energy is high, meaning that they will not charge compensate with acceptor configurations. The trivalent metals Sc and Y form readily on the *B* site, substituting for Zr, but they can also form favorably on the *A* site as donors in CZO and SZO, thereby limiting the concentrations of oxygen vacancies. We

also examine the tendency of acceptor dopants to bind with protons. Alkali metals have lower binding energies with protons than do Sc and Y, suggesting that their use will improve proton conductivity.

In Section 3.5, we compare the energetics of carbon formation in the cerates and zirconates. In this way, we explain why carbon stability is traditionally cited as being higher in the zirconates [121, 122]. Carbon interstitials form more readily in the cerates and will compete with the formation of oxygen vacancies. The cerates also have lower chemical stability with respect to carbonate formation, which should prompt the consideration of non-carbonate precursor materials during synthesis. We also report on the mobility of carbon in the zirconates and cerates, finding that carbon interstitials migrate more readily in the cerates—this result suggests that the cerates will be more susceptible to carbon degradation during operation.

3.3 Methodology

To evaluate the properties of defects and impurities in the zirconates and cerates, we apply PAW pseudopotentials with a plane-wave cutoff of 400 eV. The following electrons are treated explicitly as valence: Ca $3s^2\ 3p^6\ 4s^2$, Sr $4s^2\ 4p^6\ 5s^2$, Ba $5s^2\ 5p^6\ 6s^2$, Zr $4d^2\ 5s^2$, Ce $5s^2\ 5p^6\ 6s^2\ 5d^1\ 4f^1$, and O $2s^2\ 2p^4$. For pseudopotentials corresponding to impurities, the valence electrons are as follows: C $2s^2\ 2p^2$, N $2s^2\ 2p^3$, Na $2s^2\ 2p^6\ 3s^1$, K $3s^2\ 3p^6\ 4s^1$, Rb $4s^2\ 4p^6\ 5s^1$, Sc $3s^2\ 3p^6\ 4s^2\ 3d^1$, and Y $4s^2\ 4p^6\ 5s^2\ 4d^1$. All other electrons are treated as core states. For the orthorhombic unit cells of CZO and SZO, which contain four formula units, a $4\times4\times3$ k-point grid is used to integrate over the Brillouin zone; for BZO, which has a cubic unit cell that contains one formula unit, we use a $6\times6\times6$ k-point grid.

To calculate defect properties, we construct supercells: for CZO and SZO, the supercells have dimensions $2a \times 2b \times 2c$, containing 8 unit cells and 160 atoms in total; for cubic BZO, the supercells have dimensions $3a \times 3b \times 3c$, containing 27 unit cells and 135 atoms. For calculations of stability with respect to carbon, 160 atom supercells are used for SZO, BZO, SCO, and BCO. For the supercell calculations in each material, a $2\times2\times2$ k-point grid is used. We examine the formation of alkaline-earth (V_{Ae}, Ae = {Ca, Sr, Ba}), zirconium (V_{Zr}), and oxygen vacancies (V_{O}), as well as cation antisite defects ($\mathrm{Ae_{Zr}}$ and $\mathrm{Zr_{Ae}}$) and self-interstitials (Ae_i, Zr_i, and O_i). To study the effect of doping, we consider substitutional impurities, where an extrinsic element replaces a host atom, for example, $\mathrm{Na_{Ca}}$ in CZO, $\mathrm{Y_{Zr}}$, or $\mathrm{N_O}$. Additionally, we calculate the formation energy of alkali metals (e.g., Na), carbon, and nitrogen in interstitial positions (Na_i, C_i, and N_i). We also consider interstitial (H_i) and substitutional ($\mathrm{H_O}$) hydrogen.

Enthalpies of formation for compounds pertinent to this study are listed in Table 3.1, alongside experimental values. These values are used to calculate chemical potentials for use in defect formation energy calculations. While these ΔH^f values are in reasonable agreement with experiment, some systematic deviations are evident. It may be possible to include correction terms [138]; however, the calculated values suffice for the purposes of our present work, in which we use them merely to establish limiting cases.

3.4 Defect Engineering in Zirconates

3.4.1 Bulk Properties

The unit cells of CZO, SZO, and BZO are shown in Fig. 3.1. The depiction of BZO in Fig. 3.1(c) is expanded in order to directly compare the structure with those of CZO

Table 3.1: Calculated and reported enthalpies of formation (in eV per formula unit) for compounds pertinent to this study.

Compound	ΔH^f (eV/f.u.) (calc.)	ΔH^f (eV/f.u.) (exp.)
$CaZrO_3$	–17.41	–18.42 [139]
$SrZrO_3$	–17.38	–18.28 [140]
$BaZrO_3$	–17.29	–18.28 [140]
$SrCeO_3$	–16.87	–17.49 [141]
$BaCeO_3$	–16.77	–17.52 [141]
CaO	–6.14	–6.58 [142]
SrO	–5.61	–6.14 [142]
BaO	–5.09	–5.68 [142]
$CaCO_3$	–11.92	–12.52 [142]
$SrCO_3$	–11.98	–12.65 [142]
$BaCO_3$	–11.91	–12.58 [142]
$Ca(OH)_2$	–9.84	–10.21[142]
$Sr(OH)_2$	–9.57	–9.94[142]
$Ba(OH)_2$	–9.30	–9.79[142]
ZrO_2	–10.99	–11.41 [142]
CeO_2	–11.61	–11.29 [142]
Sc_2O_3	–18.98	–19.79 [142]
Y_2O_3	–19.05	–19.75 [142]
Na_2O	–3.76	–4.29 [142]
K_2O	–3.00	–3.75 [142]
Rb_2O	–2.62	–3.51 [142]
Zr_3N_4	–11.19	–10.16 [143]

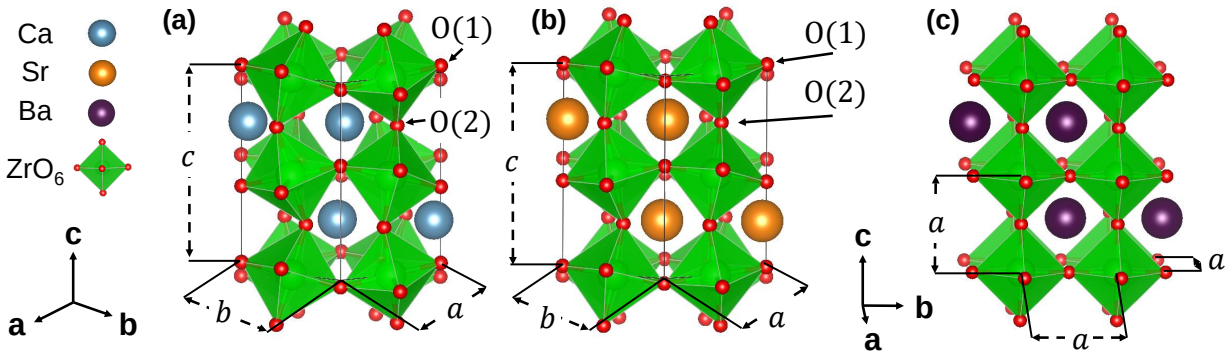

Figure 3.1: Unit cells of (a) $CaZrO_3$, (b) $SrZrO_3$, and (c) $BaZrO_3$. For $BaZrO_3$, multiple cubic unit cells are shown to facilitate comparison with the lower-symmetry structures of $CaZrO_3$ and $SrZrO_3$.

and SZO. CZO and SZO crystallize as distorted orthorhombic perovskites in the space group *Pbnm* (No. 62) with 20 atoms in their unit cells. BZO has higher symmetry and crystallizes as a cubic perovskite in the space group *Pm*-3*m* (No. 221); its unit cell can be described by five atoms. It is traditional to identify perovskite oxides with the generic formula ABO_3; thus, the alkaline-earth atoms (Ca, Sr, Ba) are *A*-site cations, while Zr is the *B*-site cation.

In CZO, tilts of the Zr–O_6 octahedra are slightly more pronounced than in SZO. These octahedra are also slightly anisotropic, such that two inequivalent O sites can be identified, one approximately in the *ab*-plane, which we label O(1), and one linking Zr atoms along the *c*-axis, which we label O(2). Calculated lattice parameters and band gaps are listed in Table 3.2, along with experimental values. The *a* and *b* lattice vectors in CZO and SZO connect next-nearest-neighbor Zr atoms, while the lattice vector in BZO connects nearest-neighbor Zr atoms. Thus, in order to directly compare unit cell sizes, the lattice constant *a* in BZO must be multiplied by $\sqrt{2}$, yielding a value of 5.93 Å, which matches the monotonic increase in lattice constants with increasing *A*-site cation size.

Table 3.2: Calculated and experimental bulk properties for $CaZrO_3$, $SrZrO_3$, and $BaZrO_3$.

Material	Method	a (Å)	b (Å)	c (Å)	Band Gap (eV)
$CaZrO_3$	HSE	5.60	5.80	8.05	5.4
	Exp. [144, 145]	5.59	5.77	8.02	5.7
$SrZrO_3$	HSE	5.81	5.87	8.24	5.2
	Exp. [146–148]	5.80	5.82	8.21	5.2, 5.6
$BaZrO_3$	HSE	4.20	4.20	4.20	4.5
	Exp. [149]	4.20	4.20	4.20	4.0

3.4.2 Chemical Potential Stability Regimes

Following the recipe outlined in Section 2.3.3, we construct chemical potential stability diagrams for the zirconates. Assuming conditions close to equilibrium, $\Delta\mu_{\mathrm{Ae}}$ (Ae={Ca,Sr,Ba}), $\Delta\mu_{\mathrm{Zr}}$, and $\Delta\mu_{\mathrm{O}}$ are related by:

$$\Delta\mu_{\mathrm{Ae}} + \Delta\mu_{\mathrm{Zr}} + 3\Delta\mu_{\mathrm{O}} = \Delta H^f(\mathrm{AeZrO_3}), \tag{3.2}$$

where $\Delta H^f(\mathrm{AeZrO_3})$ is the enthalpy of formation for $AeZrO_3$; the calculated enthalpies of formation are listed in Table 3.1.

Two limiting phases further restrict the permissible values of chemical potential, namely,

$$\Delta\mu_{\mathrm{Ae}} + \Delta\mu_{\mathrm{O}} \leq \Delta H^f(\mathrm{AeO}) \tag{3.3}$$

and

$$\Delta\mu_{\mathrm{Zr}} + 2\Delta\mu_{\mathrm{O}} \leq \Delta H^f(\mathrm{ZrO_2})\,. \tag{3.4}$$

Again, the relevant enthalpies of formation are also listed in Table 3.1. Along with the upper bounds imposed by the formation of the elemental references, Eqs. 3.3 and 3.4 define a stability region for $AeZrO_3$, shown graphically for each compound in

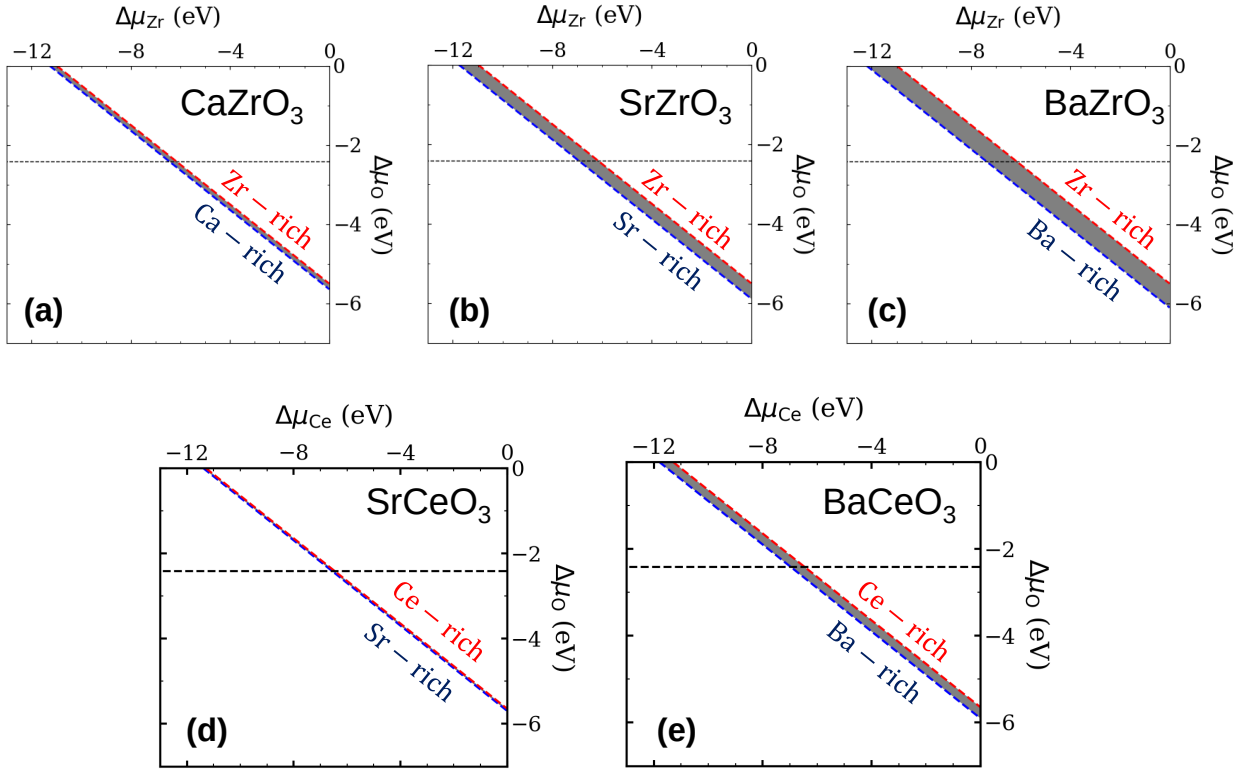

Figure 3.2: Stability regions for (a) $CaZrO_3$, (b) $SrZrO_3$, (c) $BaZrO_3$, (d) $SrCeO_3$, and (e) $BaCeO_3$, shaded in gray, in the $\Delta\mu_{Ce,Zr}$-$\Delta\mu_O$ phase space. The dashed line represents the choice of $\Delta\mu_O$ used throughout this study, $\Delta\mu_O = -2.42$ eV.

Figs. 3.2(a)–(c). An analogous procedure (replacing Zr with Ce) can be used to derive a thermodynamic stability region for the cerates SCO and BCO, which we show in Figs. 3.2(d) and (e), respectively. Note that we do not include lines corresponding to formation of Ca, Sr, or Ba metal in these figures, as we did in Fig. 2.1(b) (see Eqs. 2.26 and 2.29), as we have confirmed that these lines do not affect the chemical stability in the regions of interest for this study.

For the purposes of presenting our results, we will consider two particular chemical potential conditions; other conditions can always be examined by referring back to Eq. 3.2. For oxygen, we choose a value $\Delta\mu_O$=−2.42 eV, which corresponds to typical experimental conditions for SZO sintered in air at 1650 °C [135, 150]. These relatively

O-poor conditions favor V_O formation. Once $\Delta\mu_O$ is chosen, Eq. 3.2 fixes the sum of $\Delta\mu_{Ae}$ and $\Delta\mu_{Zr}$. Subsequently, we consider two extremes: Ae-rich and Zr-rich. Ae-rich conditions are determined by considering the bound expressed by Eq. 3.3, while Zr-rich conditions are determined by Eq. 3.4. These limits are labeled in Fig. 3.2.

For the impurity species under consideration, we again define the chemical potentials $\Delta\mu_X$ with respect to elemental references. An upper bound is placed on these chemical potentials by considering the formation of secondary phases, and for the purposes of presenting our results, we will set $\Delta\mu_X$ to its value at that bound. This limit represents the most favorable condition for impurity incorporation (i.e., the solubility limit) and permits us to compare the likelihood of various species to incorporate. For the majority of impurities considered here, the bounds are imposed by an oxide phase X_aO_b:

$$a\Delta\mu_X + b\Delta\mu_O \leq \Delta H^f(X_aO_b)\,. \tag{3.5}$$

The lack of dependence on $\Delta\mu_{Ae}$ and $\Delta\mu_{Zr}$ implies that our impurity chemical potentials are the same under Ae-rich and Zr-rich conditions.

Carbon, nitrogen, and hydrogen have limiting phases that are not binary oxides. For C, the limiting phases are the alkaline-earth carbonates; thus, the chemical potential of C is dependent upon the choice of $\Delta\mu_{Ae}$, or equivalently, $\Delta\mu_{Zr}$. Increasing $\Delta\mu_{Zr}$ decreases $\Delta\mu_C$ by the same amount, and vice versa, meaning that the substitutional configuration C_{Zr} has no net chemical potential dependence. For N, Zr_3N_4 is the limiting phase; therefore, $\Delta\mu_N$ is determined by $\Delta\mu_{Zr}$ and could, in principle, vary between Ae-rich and Zr-rich extremes. However, the magnitude of $\Delta\mu_{Zr}$ is large enough in both cases that $\Delta\mu_N$ is bounded by formation of N_2 ($\Delta\mu_N = 0$) rather than Zr_3N_4. Finally, for H, the limiting phases are the alkaline-earth hydroxides, $Ca(OH)_2$, $Sr(OH)_2$, and $Ba(OH)_2$; these compounds provide a stronger limit on H incorporation

than does water. The calculated enthalpies of formation for the limiting phases are listed in Table 3.1.

3.4.3 Defects in Zirconates

As previously mentioned, the primary goal of materials synthesis for PCOs is to create high concentrations of V_O in order to enable proton uptake via Eq. 3.1 [23]. As shown in Eq. 2.16, concentrations increase exponentially as E^f is decreased; thus, to promote V_O formation, $E^f(V_O)$ should be as small as possible. Understanding how to do so requires a precise knowledge of defect formation energies.

Native Point Defects

Our calculated formation energies for native point defects are shown in Fig. 3.3. V_O incorporates with the lowest formation energy in the $+2$ charge state. Therefore, as discussed in Section 2.3.4, a compensating negatively charged defect or impurity is needed to maintain overall charge neutrality in the system. The Fermi level will be pinned near the point where the formation-energy lines for the lowest-energy positively and negatively charged defects intersect. Forming V_O^{+2} in high concentrations thus requires acceptor species with low formation energy. Among native defects, the most likely candidate acceptors are V_{Zr}^{-4}, V_{Ae}^{-2}, and Ae_{Zr}^{-2}. However, as seen in Fig. 3.3, these defects have relatively high formation energies near the intersection point with V_O^{+2}, meaning that the resulting concentrations will be low. Extrinsic acceptor dopants are needed to form V_O^{+2} at lower formation energies and in higher concentrations.

Importantly, we find that V_O^{+2} is not necessarily the primary native donor defect. In CZO, the antisite defect Zr_{Ca}^{+2} has a lower formation energy than V_O^{+2} under both Ca-rich and Zr-rich conditions, irrespective of the oxygen chemical potential. Thus,

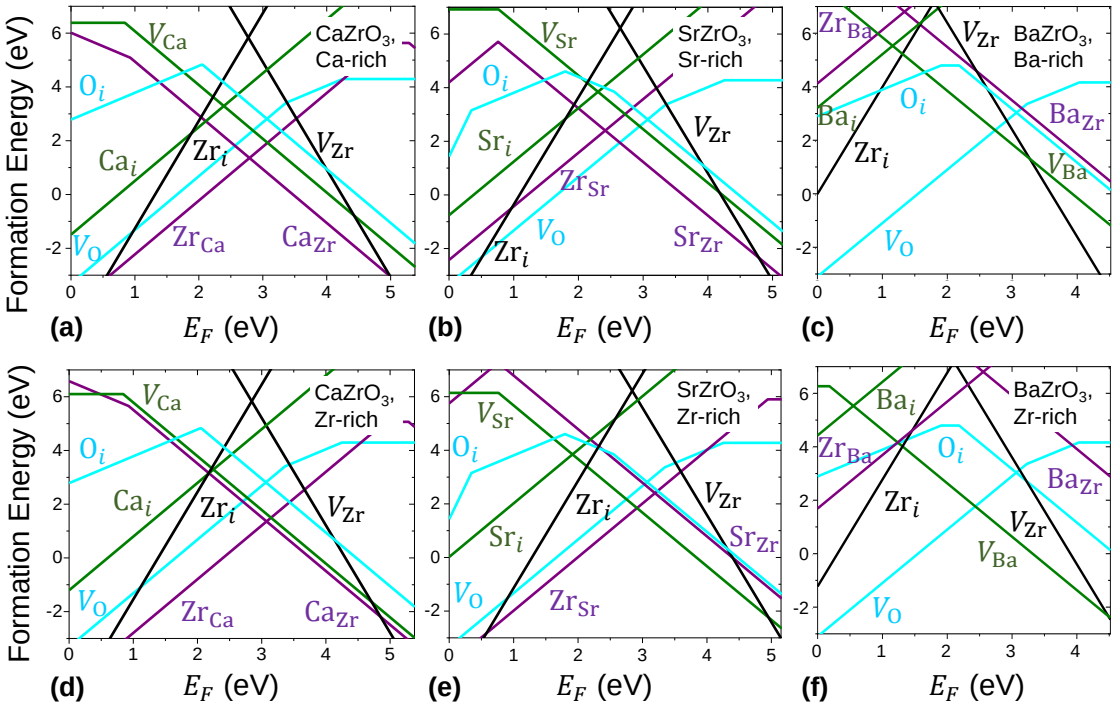

Figure 3.3: Formation energies of native defects as a function of Fermi level in $CaZrO_3$, $SrZrO_3$, and $BaZrO_3$ (a–c) under Ae-rich conditions and (d–f) under Zr-rich conditions.

Table 3.3: Ionic radii of native cations (Ca, Sr, Ba, and Zr) in Å. Values are listed for 6-fold (Zr-site) and 12-fold (Ae-site) ionic coordination environments. (From Ref. [151]).

Host Cation	Ionic Radius 6-fold Coordination	Ionic Radius 12-fold Coordination
Ca	1.00	1.34
Sr	1.18	1.44
Ba	1.35	1.61
Zr	0.72	–

the primary effect of doping CZO with acceptors will be to increase the concentration of Zr_{Ca}^{+2}, not V_O^{+2}. It can readily be shown that the difference in formation energy between Zr_{Ca} and V_O does not depend on oxygen chemical potential; thus, more oxygen-rich conditions (as could, e.g., result from exposure to water) will not affect the Zr_{Ca} concentration relative to V_O. In SZO, Zr_{Sr}^{+2} is also more stable than V_O^{+2}, but only under Zr-rich conditions; incorporation of V_O^{+2} therefore requires Sr-rich growth conditions. Only in BZO is V_O^{+2} the lowest-energy native donor under all growth conditions. These trends closely follow cation ionic radii, as seen in Table 3.3: among the alkaline-earth cations, Ca is most similar in size to Zr, which means that antisite defects will be most favorable in CZO.

Group-IIIB Dopants

The dopants most commonly used in the zirconates are group-IIIB metals such as Sc and Y, which are trivalent and therefore act as acceptors when substituting for tetravalent Zr on the *B* site. However, there is a risk that these dopants may also replace divalent alkaline-earth atoms on the *A* site and act as donors [135].

The pertinent formation energies are plotted in Fig. 3.4. Taking Sc as an example, we examine the intersection of the Sc_{Zr}^{-} formation-energy line with that of the domi-

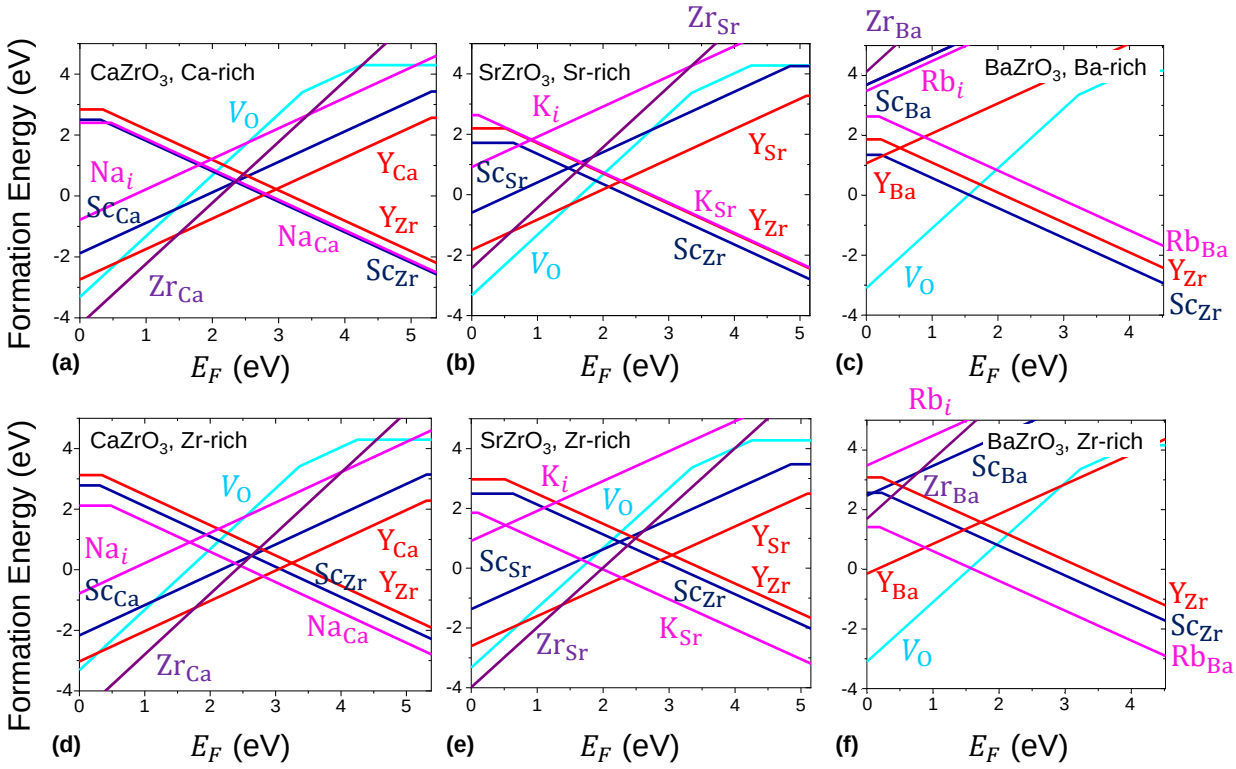

Figure 3.4: Formation energies of oxygen vacancies and dopant species in $CaZrO_3$, $SrZrO_3$, and $BaZrO_3$ (a–c) under Ae-rich conditions and (d–f) under Zr-rich conditions.

nant donors. If it intersects with V_O^{+2} at a lower formation energy than it does with Sc_{Ae}^{+} or Zr_{Ae}^{+2}, then formation of V_O will be favored; otherwise, formation of V_O will be suppressed. We note that our results on self-compensation are independent of the choice of $\Delta\mu_O$: it can be shown that the formation energies at the intersection points are independent of $\Delta\mu_O$ (although the Fermi-level value at which the crossing occurs will change). Similarly, the formation energy at the intersection point where Sc_{Zr}^{-} or Y_{Zr}^{-} compensate with their corresponding A-site donors does not depend on $\Delta\mu_{Zr}$ or $\Delta\mu_{Ae}$.

As already noted, V_O^{+2} is not the lowest-energy donor defect in CZO. Inspection of Figs. 3.4(a) and (d) shows, however, that even in the absence of Zr_{Ca}^{+2}, Sc and Y would

Table 3.4: Differences ($r_{\text{Dopant}} - r_{\text{Host}}$) in ionic radii between host cations and dopants in Å. For Zr, a 6-fold coordination is assumed; for the alkaline-earth cations (Ca, Sr, Ba), a 12-fold coordination is assumed. (From Ref. [151]).

Host Cation	Sc	Y	Na	K	Rb
Zr	0.03	0.18	0.30	0.66	0.80
Ca	–0.25	–0.10	0.06	0.39	0.49
Sr	–0.39	–0.24	–0.08	0.25	0.35
Ba	–0.55	–0.40	–0.34	0.09	0.19

prefer to self-compensate rather than generate V_{O}^{+2}. In SZO, Zr-rich conditions favor $\text{Zr}_{\text{Sr}}^{+2}$ over V_{O}^{+2}. For Sr-rich conditions, Y will preferentially self-compensate, but Sc will be effective at generating V_{O}^{+2}. Our values for V_{O} in Figs. 3.4(b) and (e) differ somewhat from those in a previous report [135]; we attribute this discrepancy to a different value of the μ_{O} reference. Finally, in BZO, no self-compensation occurs for either dopant due to the high formation energies of the $\text{Sc}_{\text{Ba}}^{+}$ and Y_{Ba}^{+} donors.

These trends can be explained by relative atomic size, as shown in Table 3.4. The ionic radii of Sc and Y are close to that of Zr, and they therefore readily incorporate on the Zr site. For incorporation on the A site, Sc and Y are closest in size to Ca, explaining why both dopants can readily substitute for Ca in CZO. In SZO, Y is closer in size to the Sr cation, while the smaller Sc ion is a worse fit. Finally, in BZO, both Sc and Y have a large size mismatch with Ba, and hence they will not incorporate on the A site.

These arguments are not sufficient to explain the experimental observation that, in BZO, Y is a significantly superior dopant compared to Sc [23]. Our results show that Sc leads to higher concentrations of V_{O}^{+2}. Clearly, there are other factors to consider when identifying optimal dopants; in Section 3.4.4, we will discuss the binding energies

between protons and acceptor dopants, which will provide an explanation for the superior characteristics of Y.

Group-IA Dopants

We now examine the effectiveness of *A*-site alkali-metal dopants. Previous computational studies have examined alkali-metal incorporation from the perspective of material stability and proton mobility [131, 132]; however, those studies did not directly address the difference with Y- or Sc-doped material, or how the improvements are influenced by growth conditions or by "wrong-site" incorporation. Experimental studies [136, 137] have also investigated alkali metal doping, showing that it increases the water uptake in BZO compared to Y-doping [137], but a microscopic explanation for this observation has not been provided. All these issues are comprehensively addressed here. We calculated the formation energies of Na, K, and Rb acceptors on the *A* site in each material (Fig. 3.4). In CZO, Na_{Ca}^{-} incorporates most readily; in SZO, K_{Sr}^{-} is lowest in energy; and in BZO, we find that Rb_{Ba}^{-} is most favored. These specific dopants are indeed similar in size to their host *A*-site cations, although, as can be seen by comparing Fig. 3.4 and Table 3.4, ionic size is not a perfect predictor of relative formation energies.

For alkali metals, "wrong-site" incorporation (i.e., incorporation on a Zr site) is expected to be less of a problem, because of the greater mismatch in both size and valence. Indeed, our calculated formation energies for these configurations are all very high. We also consider incorporation on interstitial sites, where the alkali metals act as donors. Our results in Fig. 3.4 show, however, that the Na_i, K_i, and Rb_i interstitials have high formation energies, and thus self-compensation is not a problem.

Figs. 3.4(a) and (d) again show that, in CZO, V_O is suppressed due to preferential formation of Zr_{Ca}^{+2}. The same problem arises in SZO under Zr-rich conditions

[Fig. 3.4(e)]; however, at approximately 60% Zr-rich/40% Sr-rich conditions (independent of $\Delta\mu_O$), the formation energy of Zr_{Sr}^{+2} is approximately equal to that of V_O^{+2}. Under Sr-rich conditions, Sc_{Zr} is the lowest-energy acceptor dopant in SZO [Fig. 3.4(b)]. We observe, however, that K_{Sr} is only slightly higher in energy, and K_{Sr} becomes increasingly favored over Sc_{Zr} as conditions become more Zr-rich. At a point defined by 40% Zr-rich/60% Sr-rich, K_{Sr} becomes the lowest-energy acceptor. BZO, finally, will see the highest V_O^{+2} concentrations when using Rb_{Ba} as the acceptor and growing toward the Zr-rich limit. This increase in V_O concentration explains the experimental observation of improved water uptake with alkali-metal doping [137]. Overall, our findings suggest that alkali metals are excellent choices to incorporate V_O in SZO and BZO, and synthesis at intermediate conditions for SZO and at the Zr-rich limit for BZO will maximize the V_O concentration.

Carbon and Nitrogen

Finally, we consider the incorporation of carbon and nitrogen. It was previously found that both species incorporate readily in ZrO_2 [152]. Formation energies of various configurations are plotted in Fig. 3.5. For N_O, N_i, and C_{Zr}, these formation energies do not vary between Ae-rich and Zr-rich conditions. For N_{Zr}, we plot the formation energies at the Ae-rich limit, while for C_i, C_O, and $(2C)_{Zr}$, we plot the formation energies at the Zr-rich limit; in both cases, our intent is to depict conditions for maximum incorporation. For reference, we also included the lowest-energy group-IA and group-IIIB dopants for Ae-rich and Zr-rich conditions.

We show the most favorable C configurations in BZO in Fig. 3.6; the configurations in CZO and SZO are analogous. C_O^{-2} is a candidate O-site acceptor; however, our calculations show its formation energy to be prohibitively large. We find that C_i^{+4}, shown in Fig. 3.6(a) adopts a threefold coordination with neighboring O atoms; this

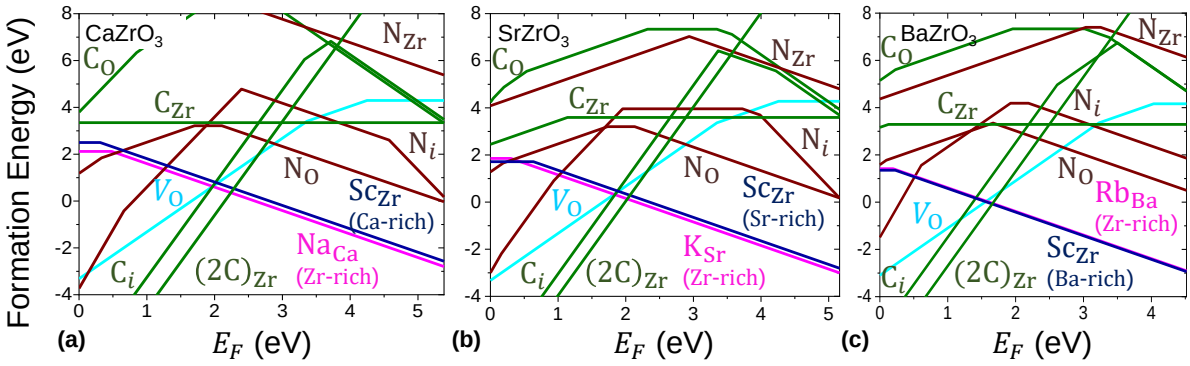

Figure 3.5: Formation energies of various configurations for C and N incorporation in (a) $CaZrO_3$, (b) $SrZrO_3$, and (c) $BaZrO_3$. N_{Zr} is plotted under Ae-rich conditions, while C_i, C_O, and $(2C)_{Zr}$ are plotted at Zr-rich conditions. Values for the lowest-energy acceptors under Ae-rich and Zr-rich conditions and for V_O are also included.

configuration is also very similar to that of C_i^{+4} in ZrO_2 [152] and other oxides [153]. Structurally, this configuration mimics that of the carbonate ion (CO_3^{-2}) in terms of C–O bond lengths (∼1.29 Å) and bond angles (∼120°). C_{Zr}, shown in Fig. 3.6(b), occurs in the neutral charge state over almost the entire range of Fermi levels, consistent with C being isoelectronic with Zr. Mirroring its behavior in ZrO_2 [152, 154], we find that carbon undergoes a large lattice relaxation away from the Zr site, becoming threefold coordinated with a subset of the oxygen nearest neighbors in a similar fashion to C_i^{+4}.

Both C_i^{+4} and C_{Zr}^{0} are relatively stable configurations, but the energy can be lowered further by forming a complex between them, which we call $(2C)_{Zr}$, shown in Fig. 3.6(c); this configuration amounts to two C atoms replacing one Zr atom in the lattice. Both C atoms adopt the same threefold coordination with nearby O atoms as C_{Zr}, with the C atoms being located in the center of three oxygen atoms on opposite faces of the octahedron surrounding the nominal Zr site. The formation energies of C_i and $(2C)_{Zr}$ can be low enough to potentially suppress the formation of oxygen vacancies; in addition, these configurations could provide a means for carbon incorporation, thus undermining the stability of the material. We remind the reader that

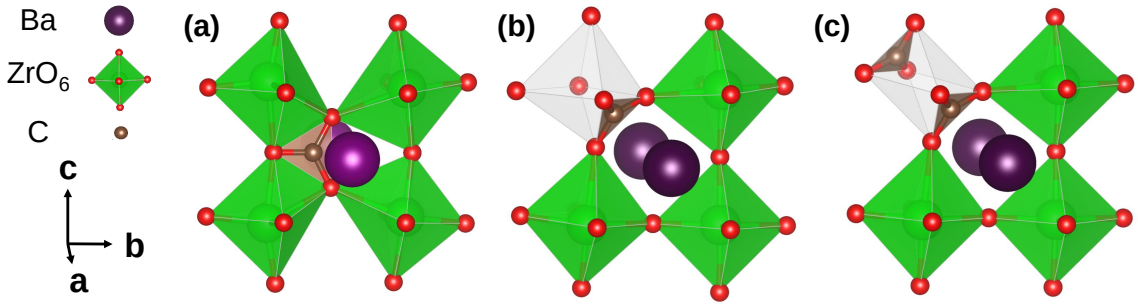

Figure 3.6: Atomic configurations of C in $BaZrO_3$: (a) C_i^{+4}, (b) C_{Zr}, and (c) $(2C)_{Zr}$. In (b) and (c), the octahedra consisting of the nominal Zr site and its six surrounding O atoms are indicated by the transparent gray regions.

our formation-energy plots assume that carbon is present at the solubility limit, i.e., a worst-case scenario in terms of unintentional carbon incorporation. Still, our results highlight the importance of limiting exposure to carbon. Carbon contamination will be discussed in more detail in Section 3.5.

The same general trends hold for N. N_O can incorporate with lower formation energies than C_O but is still unfavorable. The formation energy of N_{Zr} is also high. N_i^{+5} is the most favored nitrogen configuration, forming most readily in a threefold coordination environment with O atoms. However, the formation energy of N_i^{+5} is not low enough to play any role in acceptor compensation, even at the solubility limit.

Hydrogen

In Fig. 3.7, we show the calculated formation energies of hydrogen in both interstitial and substitutional configurations (on O lattice sites). We present energies of hydrogen configurations at the Zr-rich limit, which represents the most energetically favorable limit for hydrogen incorporation. At the Ae-rich limit, formation energies are between 0.1 eV and 0.6 eV higher, which does not affect our conclusions. Hydrogen interstitials can be present either as acceptors (H_i^-) or donors (H_i^+). Given the applications of the zirconates, the interstitial proton, H_i^+, is most pertinent to our

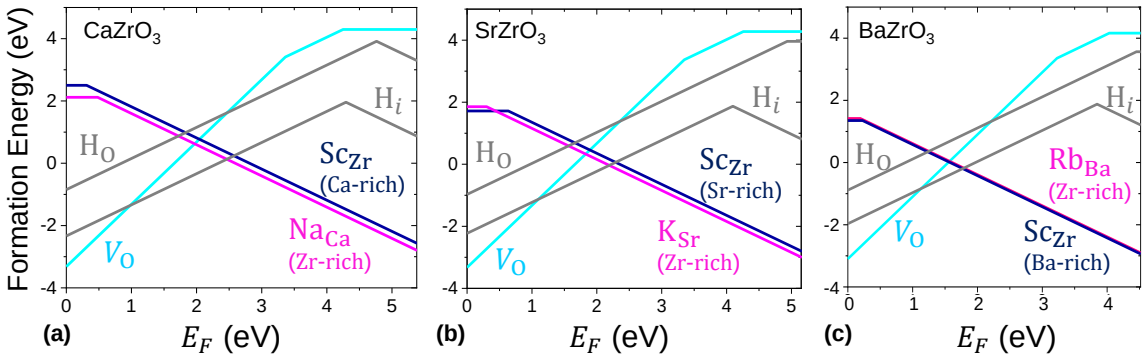

Figure 3.7: Formation energies of hydrogen configurations at the Zr-rich limit in (a) $CaZrO_3$, (b) $SrZrO_3$, and (c) $BaZrO_3$. Also included are the lowest-energy acceptors under Ae-rich and Zr-rich conditions, along with the oxygen vacancy and cation antisite formation energies.

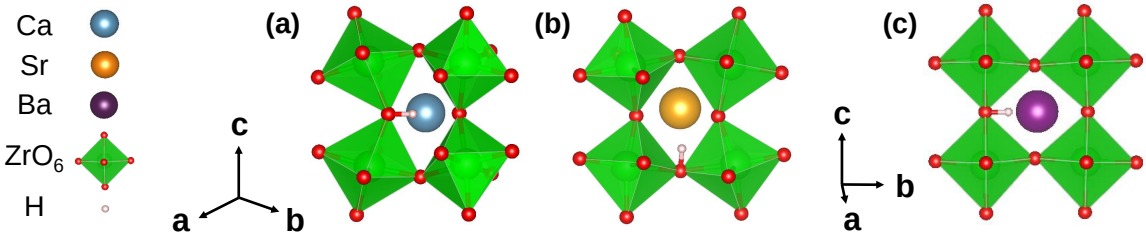

Figure 3.8: Atomic configurations of the lowest-energy positions for H_i^+ in (a) $CaZrO_3$, (b) $SrZrO_3$, and (c) $BaZrO_3$.

study. The lowest-energy configurations for H_i^+ in CZO, SZO, and BZO are shown in Fig. 3.8. Consistent with previous studies [130], we find the lowest-energy site for H_i^+ to be coordinated closely with an O atom and in close proximity to another O atom to which it can jump. In CZO, the lowest-energy site sees H_i^+ bonded to an O(2), while in SZO, H_i^+ bonds to an O(1); this difference leads to the distinct configurations seen in Figs. 3.8(a) and (b). H_i^- has fairly high formation energies and is unlikely to form.

Hydrogen on a substitutional oxygen site has been shown to be stable in oxides [155]. We find that H_O^+ adopts a multicenter bonding configuration such that it is roughly equidistant from nearby Zr cations. However, its formation energy indicates that it is less likely to incorporate than other donor species.

Table 3.5: Binding energies for complexes between H_i^+ and acceptor dopants in $CaZrO_3$, $SrZrO_3$, and $BaZrO_3$.

	E_{bind} (eV)		
Acceptor	$CaZrO_3$	$SrZrO_3$	$BaZrO_3$
Sc_{Zr}^-	0.31	0.39	0.36
Y_{Zr}^-	0.38	0.30	0.26
Na_{Ae}^-	0.40	0.32	0.49
K_{Ae}^-	0.19	0.17	0.25
Rb_{Ae}^-	0.04	0.09	0.20

3.4.4 Dopant Interactions with Protons

Trapping is an important consideration with respect to proton mobility in oxides. Protons experience Coulombic attraction to negatively charged acceptors; thus, while acceptor dopants help to incorporate protons, they also hinder the mobility of protons during device operation. We calculate the binding energy E_{bind} of a proton H_i^+ to an acceptor A^- as discussed in Chapter 2 as

$$E_{\text{bind}}(H_i^+ A^-) = E^f(H_i^+) + E^f(A^-) - E^f(H_i^+ A^-)\,. \tag{3.6}$$

We list our calculated binding energies for all the group-IA and group-IIIB dopants in Table 3.5.

Our results indicate that, in SZO and BZO, our chosen alkali metal dopants have the lowest proton binding energies. It is also worth noting that Y_{Zr} has a lower binding energy than Sc_{Zr} in SZO and BZO, consistent with other reports [135, 156]. The lower binding energy of Y indicates that it will be less of an impediment to proton conductivity, thereby helping to explain why Y is a superior dopant to Sc, as is observed experimentally [23].

Our calculated binding energies are on the same order as—or even larger than—reported proton migration barriers in the zirconates [127, 128]; therefore, proton mobility will be significantly hindered in heavily doped systems. To this end, doping BZO with Rb, which has a small proton binding energy, should provide improvements compared to doping with Y or Sc, which have higher binding energies. In general, Rb has the smallest proton binding energy among the elements considered here, which is consistent with other results on alkali metal doping [132]. For that reason, gains may be achieved through doping SZO with either K, which has the lowest formation energy, or Rb, which has the lowest binding energy and only a slightly greater formation energy. For CZO, Rb has the lowest binding energy but also a prohibitively high formation energy; Sc incorporates more readily and has a low binding energy, but its propensity to self-compensate renders it a poor option compared to Na.

3.5 Relative Carbon Stability in the Cerates and Zirconates

As mentioned at the start of the chapter (Section 3.2), the proton-conducting cerate BCO is often cited for having higher proton conductivities than BZO [119, 120], while BZO is known to be more chemically stable, particularly against CO_2 [121, 122]. As we observed in Fig. 3.6, carbon configurations in the zirconates can interfere with the incorporation of V_{O}^{+2}, which is necessary for proton uptake; thus, this same problem may be expected to manifest in the cerates. In addition, carbon can be detrimental because the cerates are prone to decomposing in carbon-rich atmospheres [117]. Several studies have shown that fuel cells based on BCO must be operated within a narrow temperature window in order to stave off decomposition when exposed to CO_2 [125, 157–159]. The stability of BCO has been improved demonstrably through alloying with BZO, with approximately equal concentrations of Zr and Ce providing the best

balance of stability and conductivity [120, 123–125]. Similar results have been demonstrated for Zr-doped SCO [160].

Previous work in our group showed that the cerates possess poor overall thermodynamic stability, and that SCO has lower stability than BCO [133, 134], which agrees with experimental observations [160, 161]. However, we are unaware of any studies aimed at uncovering the atomic-scale reason for these materials' susceptibility to carbon. Thus, we recently sought to explain this observation using our first-principles approach.

We focus now specifically on two C configurations: interstitial carbon (C_i) and the substitutional species $C_{\{Ce,Zr\}}$, shown in Fig. 3.6(a) and (b). $(2C)_{\{Ce,Zr\}}$ will not factor into the present discussion, as we choose to focus solely on the most basic forms of carbon contamination that can also likely enter the system after synthesis. We focus on {Sr,Ba}-poor ({Ce,Zr}-rich) values, where $\Delta\mu_{\{Ce,Zr\}}$ is maximized through equilibrium with $\{Ce,Zr\}O_2$. These conditions lead to higher carbon concentrations and therefore reflect a worst-case scenario at the chosen oxygen chemical potential ($\Delta\mu_O = -2.42$ eV, as previously discussed in Section 3.4.2). Choosing a specific set of chemical potential conditions is important for purposes of presenting our results; however, other conditions can easily be examined by referring to Eq. 2.15. Importantly, our results comparing relative formation energies are not affected by the particular choice of chemical potentials. We limit ourselves for the time being to $Y^{-}_{\{Ce,Zr\}}$ as the acceptor dopant, since it is the most commonly used dopant in both the cerates and the zirconates [23].

As before, we focus on values for $\Delta\mu_C$ corresponding to the solubility limit by referring to the limiting condition of carbonate formation:

$$\Delta\mu_{\{Sr,Ba\}} + \Delta\mu_C + 3\Delta\mu_O \leq \Delta H^f(\{Sr,Ba\}CO_3). \tag{3.7}$$

Table 3.6: Maximum carbon chemical potentials (at the {Sr,Ba}-poor limit) in the cerates and zirconates under selected oxygen chemical potential conditions.

Compound	$\Delta\mu_C$ (eV) ($\Delta\mu_O = -2.42$ eV)	$\Delta\mu_C$ (eV) ($\Delta\mu_O = -1$ eV)
$SrCeO_3$	–1.43	–4.27
$BaCeO_3$	–1.47	–4.30
$SrZrO_3$	–0.75	–3.59
$BaZrO_3$	–0.77	–3.61

Considering that $SrCO_3$ and $BaCO_3$ are often used as precursors in synthesis of the cerates and zirconates [117, 119, 125], this limiting condition is appropriate. For higher values of $\Delta\mu_C$, the carbonate phases will form preferentially to the zirconates and cerates; thus, for any choice of $\Delta\mu_{\{Sr,Ba\}}$ and $\Delta\mu_O$, this condition determines the maximum allowed carbon chemical potential. For more oxygen-rich conditions, the limiting value for $\Delta\mu_C$ will decrease; as a result, more oxygen-rich conditions require lower carbon chemical potentials (less carbon in the environment) to avoid destabilizing the zirconates and cerates against their respective carbonate phases.

3.5.1 Carbon Point Defects and Impurities

In Table 3.6, we list the maximum values of $\Delta\mu_C$ for $\Delta\mu_O = -2.42$ eV, which reflects typical synthesis conditions, and for $\Delta\mu_O = -1$ eV, which represents more O-rich conditions. Values of $\Delta\mu_C$ will vary linearly within this range. The values in Table 3.6 show that greater values of $\Delta\mu_C$ are permitted in the zirconates as compared to the cerates, which means that the zirconates are stable with respect to carbonates under a broader range of environments. Moving to more O-poor synthesis (i.e., lowering $\Delta\mu_O$) will increase this limit and, correspondingly, the permissible range of carbon conditions.

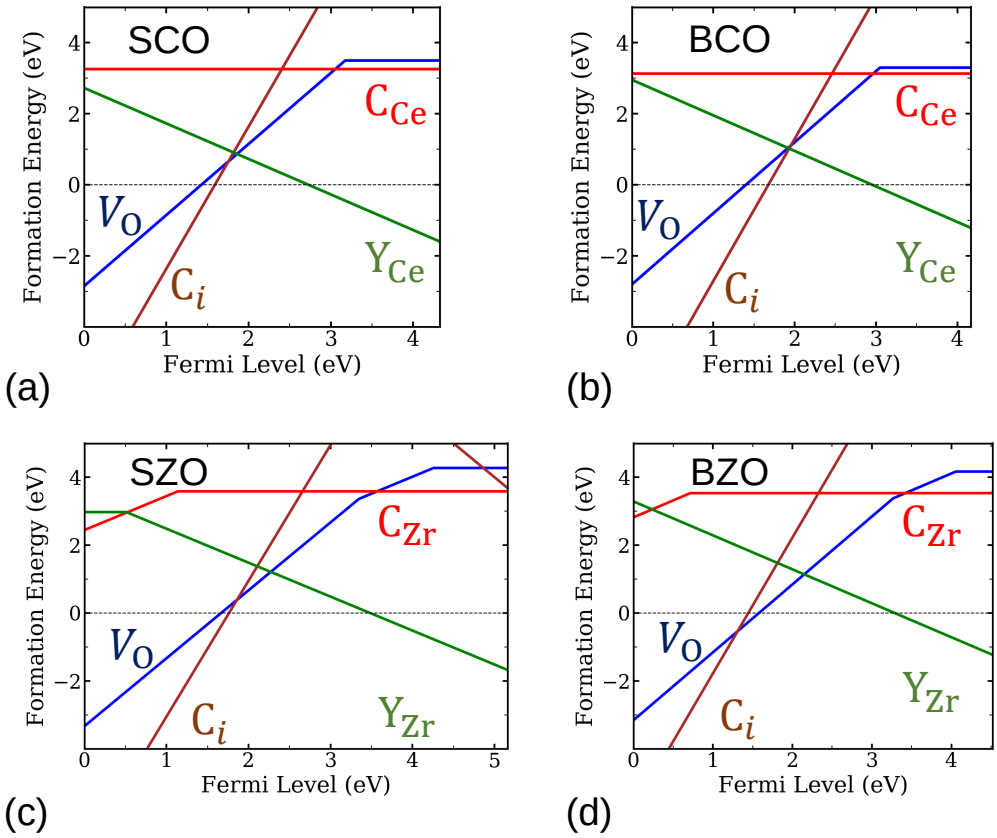

Figure 3.9: Formation energies for oxygen vacancies, yttrium dopants, and carbon impurities in (a) $SrCeO_3$, (b) $BaCeO_3$, (c) $SrZrO_3$, and (d) $BaZrO_3$ under C-rich, {Sr,Ba}-poor conditions, and with $\Delta\mu_O = -2.42$ eV.

Using the chemical potential conditions identified in Table 3.6 for $\Delta\mu_O = -2.42$ eV, we plot defect formation energies for C_i, $C_{\{Ce,Zr\}}$, V_O, and $Y_{\{Ce,Zr\}}$ in the cerates and zirconates in Fig. 3.9. Note that results for other chemical potentials can readily be obtained by referring to Eq. 2.15. Much like in the zirconates (see Section 3.4.3), C_i^{+4} is a very favorable carbon configuration, while C_{Ce}^0 is higher in energy. In each case, carbon atoms bond with three neighboring oxygen atoms, with C–O bond lengths ranging from 1.28 Å to 1.30 Å, which matches the geometry of the CO_3^{2-} ion (see Fig. 3.6).

We turn our attention to the Fermi level corresponding to charge neutrality in each system. For SCO, SZO, and BZO, charge neutrality will be determined by compensation between $Y^{-}_{\{Ce,Zr\}}$ and V_O^{+2}. In BCO, C_i^{+4} will actually be the compensating donor species, and in SCO, the formation energy of C_i^{+4} is very close to that of V_O^{+2} at the position of charge neutrality, meaning that a large concentration of C_i^{+4} will be present. In SZO and BZO, C_i^{+4} has a much higher formation energy at the Fermi level corresponding to charge neutrality. The C_i^{+4} species in BZO has a particularly high formation energy, helping to explain why low-energy acceptor dopants will not promote carbon contamination [131]. Thus, we expect the cerates to contain higher concentrations of C_i species, even when carbonate formation is not thermodynamically favored. Dopants with lower formation energies than Y^{-}_{Ce} would actually compensate with C_i^{+4} in SCO. Choosing a dopant with a *higher* formation energy will decrease the carbon concentration, albeit at the expense of also decreasing the concentration of oxygen vacancies.

Choosing more carbon-poor conditions—as could be accomplished by avoiding the use of carbonate precursors during synthesis—increases the formation energy (and hence decreases the concentration) of both carbon species relative to the other defects. Changing the chemical potentials of host species ({Sr,Ba}, {Ce,Zr}, or O), however, will not qualitatively affect our observations. Indeed, we have checked that formation energies shift only modestly (by at most 0.2–0.3 eV) when moving from {Sr,Ba}-rich to {Sr,Ba}-poor conditions. This finding is directly related to the narrow windows of chemical stability in each compound, which are particularly narrow for the cerates, as seen in Figs. 3.2(d) and (e). Furthermore, while changing $\Delta\mu_O$ moves each individual formation energy line, it does not change the formation energies of species at the charge neutrality point; it simply has the net effect of shifting the position of the Fermi level.

This point is important to emphasize: carbon incorporation will not be affected by changing native chemical potentials unless equilibrium with the carbonate species is broken. Using a synthesis route that does not involve carbonate phases is thus essential to limit carbon incorporation. One possible method involves the use of nitrate precursors [$Sr(NO_3)_2$, $Ba(NO_3)_2$, $Ce(NO_3)_3$, and $ZrO(NO_3)_2$], which have previously been used for synthesis of both cerates [162, 163] and zirconates [164, 165]. Given that nitrogen impurities have high formation energies in the zirconates (Section 3.4.3), it follows from the results we have just presented for carbon impurities that they will also have high formation energies in the cerates. As a result, nitrate precursors would be less deleterious for chemical stability.

3.5.2 Carbon Migration

To further understand carbon contamination, we study carbon mobility in the cerates and zirconates. To do so, we calculate migration barriers for carbon motion using the NEB method. The carbon interstitial will be the most mobile species. C_i^{+4} typically prefers to be nestled between two {Ce,Zr}–O_6 octahedra, which share one oxygen atom to which a C–O bond is formed. The other two C–O bonds connect C_i^{+4} with one additional oxygen atom in each of the same two octahedra (left panel of Fig. 3.10). We investigate two primary pathways for C_i^{+4} migration, which differ in the manner by which the C_i^{+4} species moves past these nearby oxygen atoms: passing directly between them in a straight line, or swinging around them by moving out-of-plane. These two possible pathways are shown schematically in Fig. 3.10. We find that the "swinging" mechanism (the lower pathway in Fig. 3.10) is much more favorable, even though several new C–O bonds are formed and broken during the process. In the higher-energy "passing-between" pathway (the upper pathway of Fig. 3.10), the

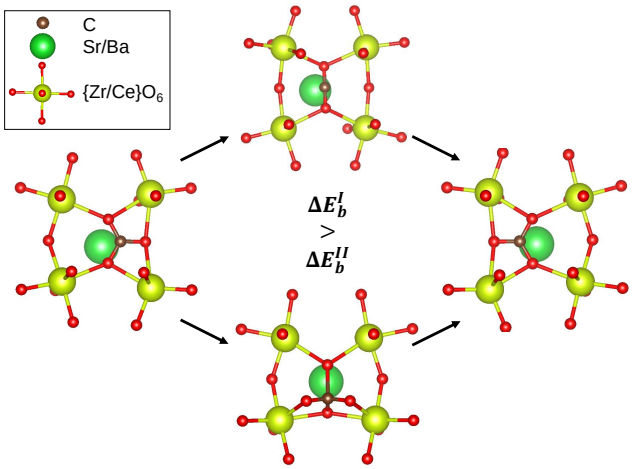

Figure 3.10: Migration pathway for the carbon interstitial (C_i^{+4}) in the cerates and zirconates. The top pathway has a higher energetic barrier than the lower pathway.

saddle-point configuration forces carbon to adopt a two-fold coordination with oxygen, which is unfavorable in light of carbon's energetic preference to be coordinated with at least three oxygen atoms.

In Table 3.7, we list migration barriers for the lowest-energy pathways we have calculated for C_i in each material. For materials sharing an *A*-site cation, the zirconates have larger barriers for migration. It has been suggested that the cubic symmetry of BZO is related to its stability with respect to carbon [123]; however, it is clear that migration barriers alone do not bear out that supposition. The migration barrier for BZO is slightly larger than that of the other materials, but its barrier relative to SZO is in line with the same trend in the cerates, making it difficult to point to symmetry as a determining factor. Overall, the barriers are such that we expect C_i^{+4} to be mobile during synthesis, and possibly also during device operation, which is typically at temperatures on the order of 1000 K.

An additional important consideration for mobility is the binding energy of complexes between acceptor dopants and carbon impurities. As acceptors like Y_{Zr}^{-} have an

Table 3.7: Calculated migration barriers E_b and binding energies (with the yttrium acceptor dopant) E_{bind} for carbon interstitials in proton-conducting oxides.

Material	C_i^{+4} (eV)	$E_{\text{bind}}[C_i^{+4}\text{-}\ Y^{-}_{\{Ce,Zr\}}]$ (eV)
$SrCeO_3$	1.03	0.52
$BaCeO_3$	2.13	0.60
$SrZrO_3$	1.87	0.95
$BaZrO_3$	2.39	0.98

opposite charge to C_i^{+4}, there will be a Coulombic binding energy hindering the movement of carbon in highly doped samples. Dopants may in fact trap carbon impurities as they move within the material, potentially decelerating decomposition reactions.

We calculate the binding energy between an acceptor A^- and a donor D^+ following the discussion in Section 2.4.2. Given that C_i^{+4} is the most significant mobile defect species, we calculate its binding energy with Y acceptors in the cerates and zirconates. These energies will need to be overcome, in addition to the migration barriers previously calculated, for carbon to be mobile.

Our calculated binding energies are listed in the second column of Table 3.7. Clearly, binding energies are significantly smaller in the cerates than in the zirconates, which, coupled with our results for migration barriers, further demonstrates that carbon will be more mobile in the cerates. Combining these binding energies with the calculated migration barriers, we conclude that carbon will be largely immobile in the zirconates at typical operating temperatures, but can relatively easily penetrate the cerates. Alloying the cerates with the zirconates will increase binding energies and migration barriers, which helps to explain the better stability observed in alloyed materials [122–125, 160].

3.6 Conclusions

Based on our results, we can offer engineering recommendations to improve the performance of the alkaline-earth zirconate solid-state proton conductors. In CZO, the Zr_{Ca}^{+2} antisite defect is lower in energy than V_O^{+2}, making it difficult to form useful concentrations of oxygen vacancies through doping. Acceptor doping does increase V_O^{+2} concentrations in SZO and BZO, and we have focused on identifying optimal dopants and growth conditions. Our results show that alkali metal doping is highly promising. Alkali metal doping leads to high concentrations of V_O^{+2}, and it avoids the self-compensation effects associated with Y doping in SZO. Alkali metal dopants also exhibit the smallest binding energies for protons in SZO and BZO, thus reducing the impact of proton trapping. We have identified the lower proton binding energy of Y as a reason for its demonstrated superiority over Sc; thus, it is significant that the alkali-metal binding energies are even lower. The incorporation of alkali metals proceeds most readily under Zr-rich conditions; therefore, we generally recommend synthesis in a Zr-rich environment. A limitation occurs in SZO, however, as Zr_{Sr}^{+2} defects will preferentially form instead of V_O^{+2} at the Zr-rich limit; to avoid these antisites, one should not go further than 60% toward the Zr-rich limit during growth.

Rb-doped BZO is the best solid-state proton conductor among the zirconates studied here: Rb is the optimal dopant to increase the concentration of V_O^{+2}, and it also exhibits a lower proton binding energy than Y, long considered the state-of-the-art acceptor dopant [23]. Experimental studies of K- and Rb-doped SZO are also called for to confirm our predicted enhancement in V_O^{+2} formation.

In addition, we have examined and compared the formation and mobility of carbon impurity species in the cerates and zirconates. Carbon is the impurity element most likely to incorporate in the zirconates; nitrogen and hydrogen configurations are

higher in energy. We showed that the cerates have lower chemical stability with respect to carbonates at specific oxygen chemical potentials, and that synthesis at more oxygen-poor conditions will permit a wider range of carbon chemical potentials while avoiding carbonate formation. But carbonate formation is not the only concern: we find that interstitial C_i^{+4} can incorporate in both the cerates and the zirconates, and it competes with V_O^{+2}, thus hindering prospects for proton conduction. Carbon contamination is particularly severe for the cerates, because of both the lower formation energy of C_i as well as the higher mobility of interstitial carbon, which allows carbon to penetrate into the cerates at typical operating temperatures. Choosing dopants other than Y can suppress carbon incorporation, but at the expense of lowering V_O concentrations.

We also find that simply changing host-atom chemical potentials during synthesis cannot suppress carbon incorporation, and thus avoiding exposure to carbon is essential for the cerates; use of precursors other than carbonates could be a promising route. Exposure to carbon during operation will also be detrimental for cerates. Overall, the zirconates are less sensitive to all of these deleterious effects, and therefore, alloying cerates with zirconates will improve stability. For pure cerates, completely avoiding carbon contamination will be crucial for unlocking their performance in proton-conducting applications.

Chapter 4

Defect Engineering in the Alkaline-Earth Hydrides

4.1 Permissions and Attributions

The content of Chapter 4 follows from work that has previously appeared in Chemistry of Materials (Ref. [166]). This work was performed in collaboration with Dr. Leigh Weston.

4.2 Metal-Hydride Electrolytes

Hydride-ion conductors, in comparison with proton conductors like those described in Chapter 3, are relatively unexplored. While they are not as mobile as protons, hydride ions are still quite mobile, more so than any other anion. Protons also tend to form strong covalent bonds, particulaly in oxides, whereas hydride ions form weaker bonds that are more ionic in nature [167]. Hydride-ion conductors also tend to be

stable in different synthesis environments than do proton conductors, thereby filling new niches for operation.

Certain metal hydrides are among the materials recently gaining attention for their hydride-ion conductivity. Metal hydrides have long shown promise for hydrogen storage, due to their high gravimetric densities of hydrogen [17, 54]. Conductivity in these systems was not widely examined until Verbraeken *et al*. [28] showed that BaH_2 exhibits hydride ionic conductivity rivaling that of the best-known solid-state proton conductors. Previously, reports on CaH_2 and SrH_2 had shown promising conductivity as well [168]. CaH_2, SrH_2, and BaH_2 are highly thermodynamically stable [169] and operate under a wide range of temperature and pressure conditions. Unintended oxygen incorporation does not significantly affect their properties [28, 168]. For these reasons, they may be attractive alternatives to less-stable proton-conducting oxides, especially if their ionic conductivity can be optimized.

Improving ionic conductivity requires a thorough understanding of the diffusion process in CaH_2, SrH_2, and BaH_2. Their observed hydride diffusion [28] can be explained either by motion of an interstitial hydride ion (H_i^-) or of a hydrogen vacancy (V_H). Experimental studies [28, 168, 170] have surmised the latter based on large observed concentrations of hydrogen vacancies. It has been reported that Na doping impacts the ionic conductivity, particularly in SrH_2 [168]; this effect is likely connected to the materials' defect chemistry.

In this chapter, we report on results from DFT calculations that provide direct microscopic evidence for the dominant transport mechanism in the alkaline-earth hydrides. We also investigate avenues for enhancing the ionic conductivity, particularly through doping. Consistent with experiments, we find that hydrogen vacancies (V_H) can form in large concentrations, particularly in the positive charge state. The charge state strongly impacts the migration barrier of V_H, which can be as low as 0.16 eV for

the positive charge state (V_H^+) but much higher (up to 0.95 eV) for the neutral and negative charge states. Based on our calculations, we offer a physical explanation for this trend.

We find that the V_H^+ defect is more mobile than in other metal hydrides [32, 33, 171, 172]. In order to lower the overall activation energy of hydride-ion diffusion, we introduce acceptor impurities, such as alkali metals, to reduce the formation energy of V_H^+. We show that doping significantly improves ionic conductivity, and in BaH_2, the resultant conductivity is equivalent to proton conductivities in some of the best proton-conducting oxides. Our results thus provide a route toward improving hydride-ion conductivity in the heavy alkaline-earth hydrides, to the point of positioning them as compelling alternatives to more traditional solid-state proton conductors.

4.3 Methodology

PAW pseudopotentials [90, 91] are used with a plane-wave cutoff of 400 eV. The Ca $3s^2\ 3p^6\ 4s^2$, Sr $4s^2\ 4p^6\ 5s^2$, Ba $5s^2\ 5p^6\ 6s^2$, Na $2s^2\ 2p^6\ 3s^1$, K $3s^2\ 3p^6\ 4s^1$, Rb $4s^2\ 4p^6\ 5s^1$, and Cs $5s^2\ 5p^6\ 6s^1$ electrons are treated explicitly as valence. For the bulk primitive cells, a $5\times5\times3$ k-point grid is used to integrate over the Brillouin zone of the orthorhombic lattice; for the supercell calculations, a $2\times2\times2$ grid is used.

To calculate defect properties, supercells are constructed with dimensions $3a \times 2b \times 2c$, containing 12 primitive cells and 144 atoms in total. These supercells are used to simulate one of several point defects: H vacancies (V_H), alkaline-earth cation vacancies (e.g., V_{Ba}), H interstitials (H_i), and extrinsic substitutional species with one of four alkali metals (Na, K, Rb, and Cs) located on cation sites (e.g., Na_{Ba}).

We follow the procedure described in Section 2.3.3 to calculate defect formation energies. First, the stability condition for AeH_2 (Ae={Ca,Sr,Ba}) in thermodynamic

Table 4.1: Calculated enthalpies of formation (in eV per formula unit) for three alkaline-earth hydrides (AeH_2) and four alkali-metal hydrides (AH).

AeH_2	ΔH^f (eV)	AH	ΔH^f (eV)
CaH_2	–1.84	NaH	–0.47
SrH_2	–1.80	KH	–0.44
BaH_2	–1.69	RbH	–0.36
–	–	CsH	–0.27

equilibrium requires that

$$\Delta\mu_{\mathrm{Ae}} + 2\Delta\mu_{\mathrm{H}} = \Delta H^f(\mathrm{AeH_2}), \tag{4.1}$$

where $\Delta H^f(\mathrm{AeH_2})$ is the enthalpy of formation. An upper bound on the alkaline-earth chemical potential is determined by equilibrium with the solid-phase metal, corresponding to $\Delta\mu_{\mathrm{Ae}} = 0$; combined with Eq. 4.1 this sets a lower bound on the hydrogen chemical potential, namely $\Delta\mu_{\mathrm{H}} = \Delta H^f(\mathrm{AeH_2})/2$, which we will call the H-poor limit. Similarly, we define an H-rich limit based on $\Delta\mu_{\mathrm{H}} = 0$, corresponding to $\Delta\mu_{\mathrm{Ae}} = \Delta H^f(\mathrm{AeH_2})$. The calculated enthalpies of formation are listed in Table 4.1; these values are in reasonable agreement with other reports, both experimental and computational [173–175].

We also define chemical potentials for impurity species that are used as dopants. The chemical potential of each alkali-metal dopant is referenced to the total energy of a single atom in the solid alkali-metal phase. An upper bound is placed on these impurity chemical potentials prevent the formation of secondary alkali-metal hydride phases (AH),

$$\Delta\mu_{\mathrm{A}} + \Delta\mu_{\mathrm{H}} \leq \Delta H^f(\mathrm{AH}). \tag{4.2}$$

For the purposes of presenting our results, we choose the chemical potentials for the impurity species to correspond to this upper bound, i.e., the solubility limit. The calculated enthalpies of formation for the AH compounds are also listed in Table 4.1.

4.4 Defect Engineering in the Alkaline-Earth Hydrides

4.4.1 Bulk Properties

At room temperature and ambient pressure CaH_2, SrH_2, and BaH_2 all crystallize in the cotunnite crystal structure, which has orthorhombic symmetry and is identified with the space group *Pnma* (No. 62). This structure is shown in Fig. 4.1 for the case of BaH_2. There are two symmetrically inequivalent sites for H atoms on the lattice that are arranged about the alkaline-earth atom in a distorted square pyramidal configuration. One of the sites, hereafter referred to as H1, is coordinated to nearby alkaline-earth atoms through shared corners of neighboring pyramids, while the other site, H2, is located on the remaining unshared vertex of the BaH_5 pyramids. These sites are present in equal concentrations in the crystal.

Our calculated bulk properties of orthorhombic CaH_2, SrH_2, and BaH_2 are listed in Table 4.2, along with experimental data. Our results are in good agreement with experimental values. Table 4.2 also summarizes our calculated band-gap values for each material.

4.4.2 Defect Formation

We conducted a comprehensive study of point defects in CaH_2, SrH_2, and BaH_2. The defect formation energies are plotted as a function of the Fermi level in Fig. 4.2.

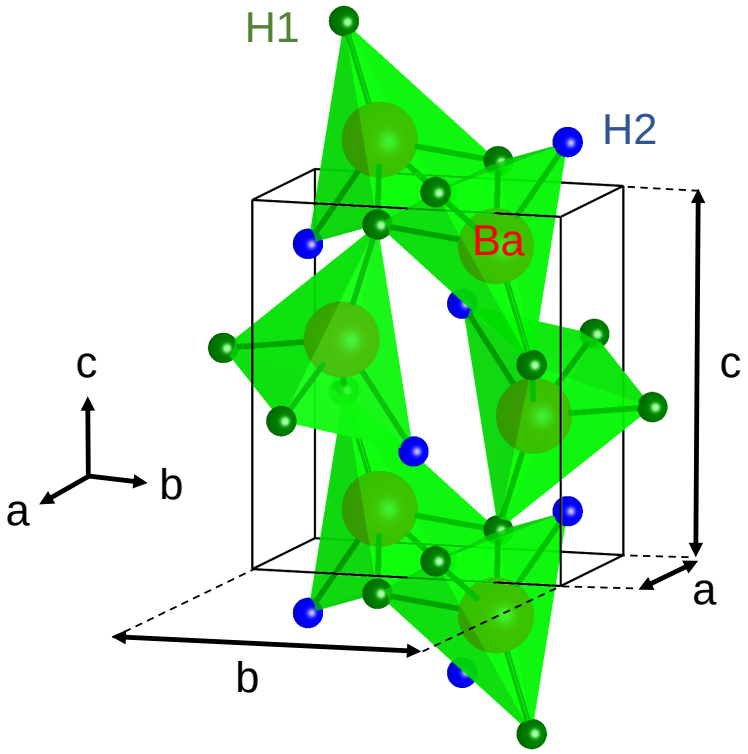

Figure 4.1: The cotunnite crystal structure of BaH_2.

Table 4.2: Calculated and experimental bulk properties for CaH_2, SrH_2, and BaH_2.

Material	Method	a (Å)	b (Å)	c (Å)	Band Gap (eV)
CaH_2	HSE	5.90	3.57	6.77	4.09
	Exp. [168]	5.95	3.59	6.80	–
SrH_2	HSE	6.35	3.85	7.29	4.18
	Exp. [168]	6.37	3.86	7.31	–
BaH_2	HSE	6.84	4.17	7.87	3.85
	Exp. [28]	6.78	4.16	7.84	–

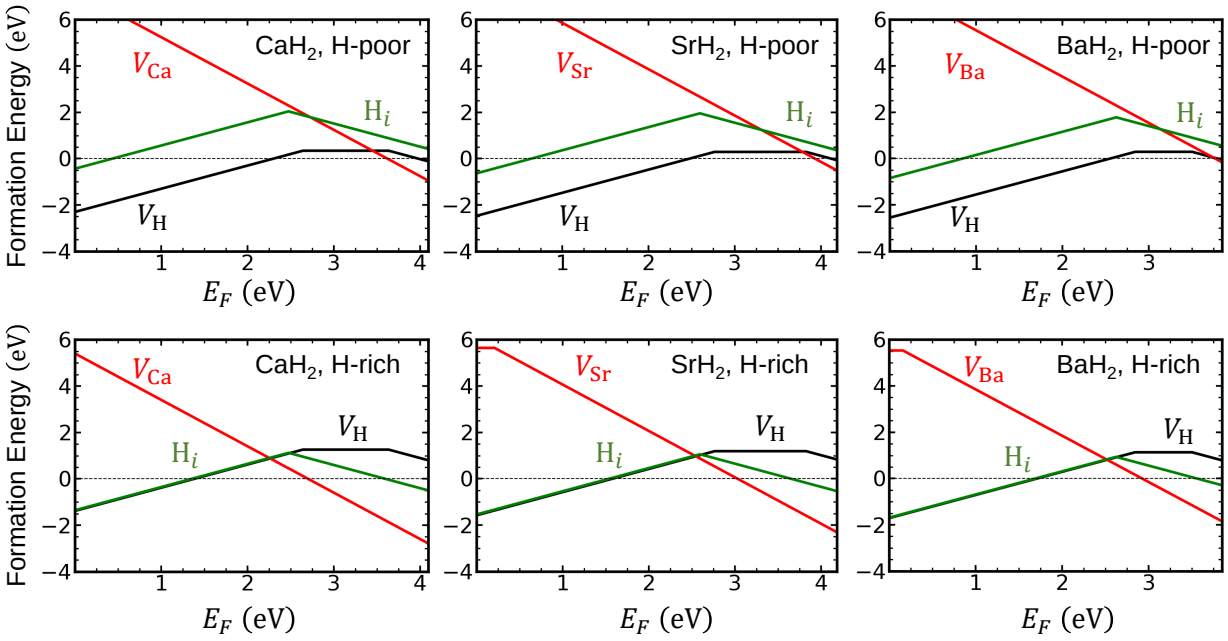

Figure 4.2: Defect formation energies for (a) CaH_2, (b) SrH_2, and (c) BaH_2 under H-poor (Ae-rich) conditions, and (d) CaH_2, (e) SrH_2, and (f) BaH_2 under H-rich (Ae-poor) conditions. The slopes of the line segments for each defect correspond to the charge state.

Results are shown for chemical potentials representing H-poor (Ae-rich) and H-rich (Ae-poor) conditions.

Beginning with CaH_2, we first consider the case of H-poor (Ca-rich) conditions (Fig. 4.2(a)). It is clear that V_H has a low formation energy, and this defect can be present as V_H^+, V_H^0, or V_H^-. The formation energies of the vacancies are very similar on the H1 and H2 sites, differing by less than 150 meV; therefore, for ease of presentation, we will only plot the formation energy for the most favored site. V_H^+ (on the H1 site) is the lowest energy positive defect, and V_{Ca}^{-2} is the lowest energy negatively charged defect. Near the crossing point of their formation energies (at 3.25 eV above the VBM), a neutral defect (V_H^0, preferring the H2 site) has a lower formation energy (equal to 0.34 eV). The Fermi level can thus be located anywhere in the range where V_H^0 is the lowest-energy defect, and given its low energy, we expect this defect to form in large

concentrations. Similar conclusions can be reached by inspecting the formation energy curves for SrH_2 and BaH_2 under H-poor conditions (Figs. 4.2(b) and (c)); in both cases, the formation energy of V_H^0 is 0.29 eV. In SrH_2, V_H^0 favors the H2 site, while V_H^- favors H1. In BaH_2, V_H^0 and V_H^- both favor H1.

Under H-rich (Ca-poor) conditions, the formation energy of V_H in CaH_2 is increased, while the formation energy of V_{Ca} is decreased [Fig. 4.2(d)]. As a result, the intersection point of the formation-energy curves is shifted to lower values, namely 2.33 eV above the VBM, where the formation energy of V_H^+ is 0.94 eV. In contrast to H-poor (Ca-rich) conditions, the formation energy of V_H^0 now lies above this intersection, implying that charge neutrality can now be achieved with a mixture of V_H^+ and V_{Ca}^{-2}. It should be noted that H_i^+ has a very similar formation energy as V_H^+ under these conditions. However, actual growth or operating conditions will tend to be below the H-rich limit, and therefore we do not expect H_i^+ to be present in large concentrations in these materials. Again, the situation is very similar in SrH_2 and BaH_2. In SrH_2, the formation energy of V_H^+ is 0.97 eV, and in BaH_2, it is 0.81 eV. We will return to the formation energies when discussing activation energies for hydrogen migration.

4.4.3 Defect Migration

We now use the NEB method to determine the barriers for vacancy migration. By comparing several different migration pathways, we determined that the most energetically favorable path for vacancy migration involves hopping from a H1 site to a nearest neighbor H2 site, followed by a subsequent hop to the next-nearest neighbor H1 site, as shown in Fig. 4.3(a) for BaH_2; the general behavior is the same for CaH_2 and SrH_2. V_H^+ has an energetic preference to reside on H1 (by 66 meV for CaH_2, 29 meV for SrH_2, and 60 meV for BaH_2); thus, the barrier is slightly higher for vacancies

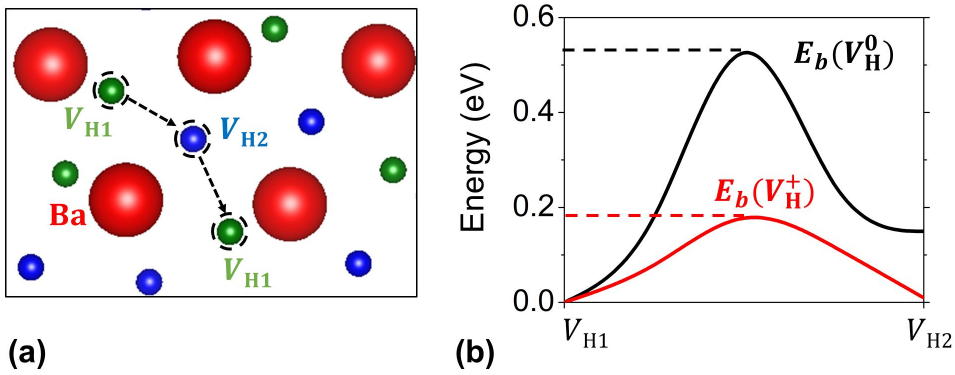

Figure 4.3: (a) Schematic pathway for V_H migration between H1 and H2 sites in BaH_2. (b) Potential energy change along the migration path for V_H^0 or V_H^+ in BaH_2.

Table 4.3: Migration barriers E_b for hydrogen vacancies in CaH_2, SrH_2, and BaH_2.

Material	$E_b(V_H^+)$ (eV)	$E_b(V_H)$ (eV)	$E_b(V_H^-)$ (eV)
CaH_2	0.16	0.70	0.95
SrH_2	0.16	0.72	0.87
BaH_2	0.18	0.53	0.66

migrating from the H1 site to H2 than from H2 to H1. We report the higher of the two barriers as the rate-limiting migration barrier. The potential energy pathway for migration between the H1 and H2 sites is shown in Fig. 4.3(b).

Table 4.3 summarizes our calculated results for migration barriers for vacancies in charge states $q = \{-, 0, +\}$ for all three hydrides. The migration barriers for V_H^0 are 0.70 eV in CaH_2, 0.72 eV in SrH_2, and 0.53 eV in BaH_2, and for the negatively charged vacancy the barriers are even higher. In contrast, the migration barriers are much lower for the positively charged vacancy: 0.16 eV in CaH_2 and SrH_2, and 0.18 eV in BaH_2. To the best of our knowledge, these migration barriers for V_H^+ are lower than any other calculated values for V_H migration in a metal hydride [32, 33, 171, 172].

The trend in the migration barrier for the various charge states can be explained by the occupation of the defect bonding state. For example, in BaH_2, the formation of a hydrogen vacancy creates dangling bonds derived from Ba *d* states, which combine to form a localized bonding state in the band gap and antibonding states above the CBM. Figure 4.4 shows a charge density plot for the neutral defect alongside a schematic band diagram showing the relative positions of the CBM, VBM, and defect levels formed by creating a hydrogen vacancy. Due to the bonding nature of the gap state, populating it strengthens the bonds between these Ba atoms and makes it energetically difficult for a nearby H atom to move into the vacancy. The Ba–Ba bonding is even stronger in the case of V_H^-, where the defect state is doubly occupied. This explains why the migration barrier for the hydrogen vacancy is relatively high for V_H^0, and even higher for V_H^-. In the case of V_H^+, however, the gap state is unoccupied, and the Ba atoms relax outward, making it easy for a neighboring H atom to move into the vacancy site: no Ba–Ba bonds need to be broken, and the Coulombic repulsion is reduced. The monotonic increase in migration barriers as the charge state changes from positive to negative, seen in Table 4.3, is well-supported by this physical explanation.

In the case of H-rich (Ae-poor) conditions, for which charge compensation between V_H^+ and V_{Ae}^{-2} is predicted, the binding energy of these two defects becomes an important factor in determining the mobility of V_H^+. Using the definition for binding energy in Eq. 2.36 and the formation energies for V_H^+ and V_{Ae}^{-2}, the binding energies are calculated as 0.23 eV for $[V_H V_{Ca}]^-$, 0.31 eV for $[V_H V_{Sr}]^-$, and 0.12 eV for $[V_H V_{Ba}]^-$ (see Table 4.4). For any V_H^+ that becomes trapped by a nearby V_{Ae}^{-2}, the binding energy must be overcome in order for V_H^+ migration to proceed. Therefore, hydride-ion transport under these conditions would be trap-limited.

Table 4.4: Binding energies for complexes between V_H^+ and either alkali-metal dopants or cation vacancies in CaH_2, SrH_2, and BaH_2. Differences in ionic radius between the host cation and each dopant are also listed (from Ref. [151]).

Material	Acceptor	E_{bind} (eV)	$\lvert r_A - r_{Ae} \rvert$ (Å)
CaH_2	V_{Ca}^{-2}	0.23	–
	Na	0.46	0.06
	K	0.55	0.41
	Rb	0.71	0.51
	Cs	1.02	0.60
SrH_2	V_{Sr}^{-2}	0.31	–
	Na	0.48	–0.07
	K	0.48	0.24
	Rb	0.59	0.38
	Cs	0.90	0.47
BaH_2	V_{Ba}^{-2}	0.12	–
	Na	0.38	–0.23
	K	0.27	0.08
	Rb	0.36	0.22
	Cs	0.66	0.31

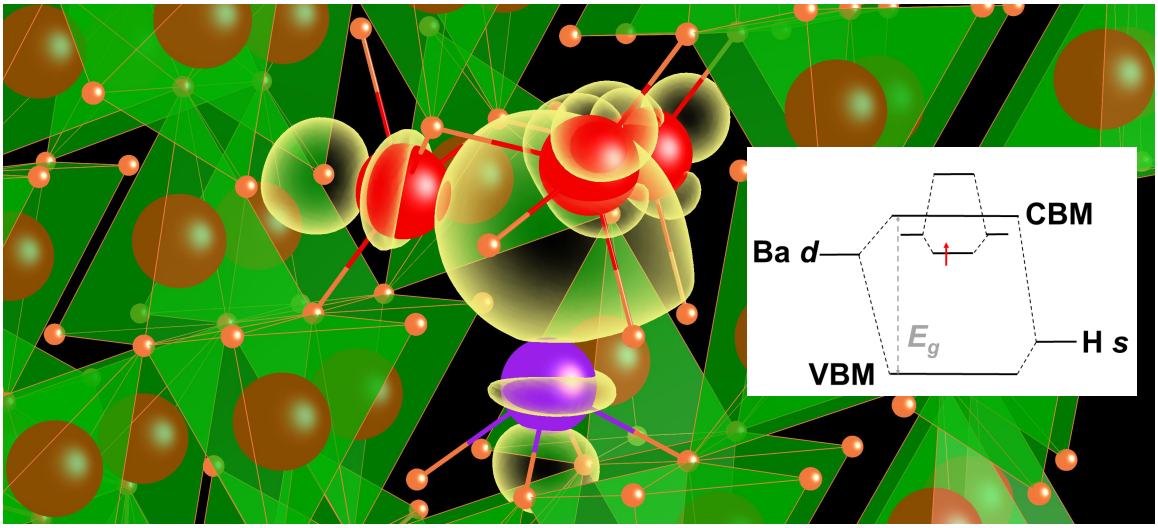

Figure 4.4: Charge density isosurface showing the overlap of Ba d orbitals (and/or K d orbitals) to form the occupied defect level of a V_{H}^{0} in BaH_2. Ba atoms are colored red, K purple, and H orange. Inset is a schematic showing the positions of the defect states relative to the VBM and CBM for the V_{H}^{0} defect. The bonding state is occupied by one electron in this case.

4.5 Ionic Conductivity

4.5.1 Theoretical Considerations

We can now proceed to calculate ionic conductivity in the alkaline-earth hydrides. To do so, we rely on the framework discussed in Section 2.4, which makes it clear that conductivity depends on both the migration barrier of V_{H} and the vacancy concentration, related to the formation energy via Eq. 2.16. We note that our estimates for diffusivity and conductivity represent an underestimate, as we choose to neglect the entropy term in Eq. 2.33.

Given that the lowest-energy charge state depends on the hydrogen chemical potential, and that the migration barriers strongly depend on the charge state, it is important to note how the activation energies (Eq. 2.35) change under different conditions. In the H-poor limit, V_{H}^{0} dominates, and $E_a = E^f(V_{\mathrm{H}}^{0}) + E_b(V_{\mathrm{H}}^{0})$ is 1.04 eV in CaH_2, 1.01

eV in SrH_2, and 0.82 eV in BaH_2. Under H-rich conditions, V_H^+ dominates; this defect has a lower migration barrier than V_H^0, but a higher formation energy, resulting in E_a values of 1.10 eV for CaH_2, 1.13 eV for SrH_2, and 0.99 for BaH_2. These considerations make clear that, while it is desirable to take advantage of the lower migration barrier of V_H^+, a strategy is needed to lower its formation energy. Formation energy can be decreased by lowering the Fermi level; thus, we propose to move the Fermi level closer to the VBM by doping with impurities that act as acceptors.

4.5.2 Conductivity Engineering through Alkali Metal Doping

The addition of acceptor impurities will shift the defect equilibrium, such that charge neutrality is achieved by balancing V_H^+ and negatively charged acceptors. This scheme will only work, of course, if the formation energy of the dopants is sufficiently low, something we can assess with our first-principles calculations. We consider four alkali metals as possible dopants: Na, K, Rb, Cs. These elements have only one valence electron, compared with two for the alkaline-earth cations, suggesting that they will act as acceptors when substituting at the cation site. Chemical potentials for these dopants were derived from the calculated formation enthalpies of corresponding alkali-metal hydrides, listed in Table 4.1, using Eq. 4.2.

The formation energies for the alkali-metal dopants are plotted in Fig. 4.5. Only the negative charge states of the dopants are shown; neutral charge states are stable close to the VBM (within 0.5 eV or less) but do not affect our conclusions. The formation energies of the acceptors depend on the host material; we have identified the driving factor to be the size match between the dopant and the host atom, as discussed below. For CaH_2 and SrH_2, the acceptor dopant with the lowest formation energy is Na; for BaH_2, the lowest-energy dopant is K.

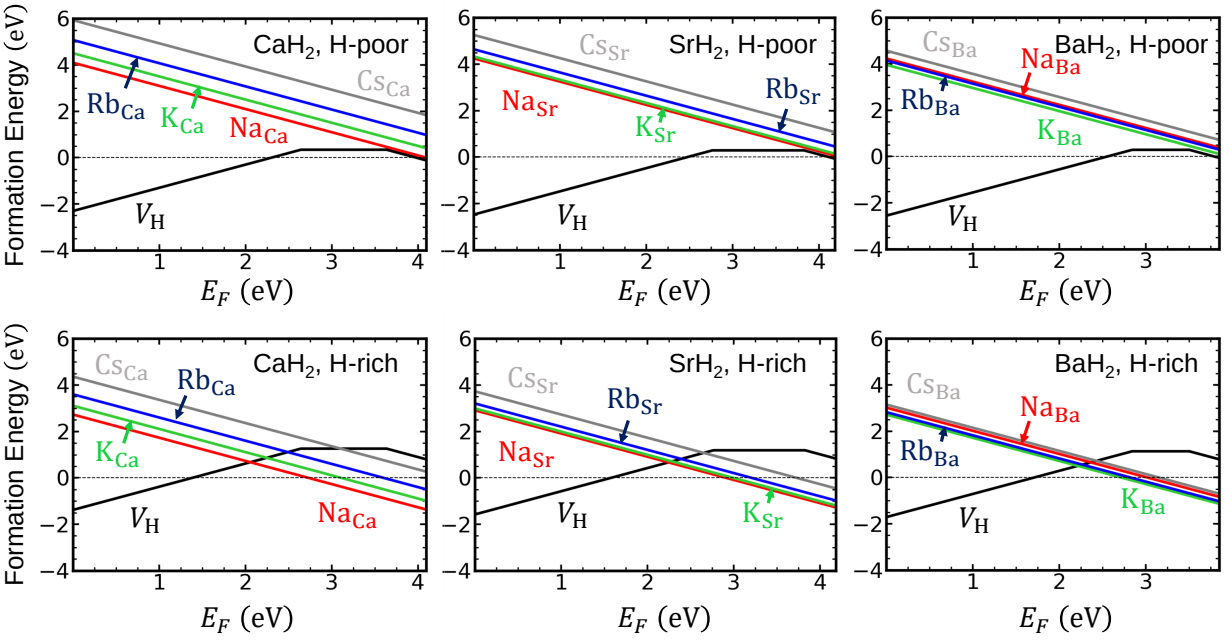

Figure 4.5: Formation energies of four alkali-metal dopants on the alkaline-earth site in the negative charge state, shown along with the formation energy of hydrogen vacancies, for (a) CaH_2, (b) SrH_2, and (c) BaH_2 under H-poor (Ae-rich) conditions; and (d) CaH_2, (e) SrH_2, and (f) BaH_2 under H-rich (Ae-poor) conditions.

Hydrogen-poor (Ae-rich) conditions make it difficult for the dopant to incorporate on the cation site, and hence lead to high formation energies. V_{H}^{0} remains the dominant defect for all three materials, as it is in the undoped case. In the H-rich (Ae-poor) case, the formation energies of the dopants are shifted to lower values and intersect those for V_{H}^{+} at Fermi-level positions that are closer to the VBM than when charge compensation was provided by cation vacancies [Fig. 4.2(d)–(f)]. With this shift, the formation energies for V_{H}^{+} are 0.67 eV for CaH_2, 0.68 eV for SrH_2, and 0.50 eV for BaH_2. In CaH_2 and SrH_2, we note that these formation energies correspond to dopant concentrations on the order of 0.01 mol% at typical synthesis temperatures (600 °C); experiments observed up to 0.1 mol% dopant incorporation [168], in reasonable agreement with our calculation. Higher dopant concentrations will increase the hydrogen vacancy concentrations. Our calculated formation energies are distinctly lower than in the absence of dopants, and they directly translate into lower activation energies for ionic conductivity: 0.83 eV for CaH_2, 0.84 eV for SrH_2, and 0.68 eV for BaH_2. We note that the activation energy for K-doped BaH_2 is comparable to the activation energies measured for proton conduction in the alkaline-earth zirconates, which range from 0.4 eV to 0.6 eV [117].

The effect on conductivity at characteristic operating temperatures is summarized in Table 4.5. In each case, doping under H-rich conditions improves the conductivity relative to undoped materials (for which we assume charge compensation by V_{Ae}^{-2}, and the lowest value of $\Delta\mu_{\mathrm{H}}$ that avoids formation of V_{H}^{0}). The highest conductivity is obtained in doped BaH_2, about 6×10^{-3} S cm^{-1} at $T = 673$ K; this conductivity is comparable to that of the best proton-conducting oxides [117]. In the following section, we will demonstrate that these conductivities can be optimized even further.

While synthesis at the H-rich limit incorporates alkali-metal dopants and V_{H}^{+} in their highest concentrations, doping still proves advantageous even under less H-rich

Table 4.5: Ionic conductivities for V_H^+ migration in doped AeH_2 under H-rich conditions and in undoped AeH_2 under conditions that maximize V_H^+ formation, at a typical operating temperature of 673 K. The results for doped compounds are taken from the most energetically favored dopants: Na in CaH_2 and SrH_2, and K in BaH_2.

	σ (S cm^{-1})	
	Doped	Undoped
CaH_2	4.73×10^{-4}	4.50×10^{-6}
SrH_2	3.72×10^{-4}	2.51×10^{-6}
BaH_2	5.85×10^{-3}	2.79×10^{-5}

conditions. The hydrogen chemical potential should be limited to values that promote formation of V_H^+ (as opposed to V_H^0), due to its low migration barrier. Taking BaH_2 as an example, V_H^+ will form through compensation with K_{Ba}^- for $\Delta\mu_H$ ranging from 0 eV to -0.57 eV. At $\Delta\mu_H = -0.57$ eV, the formation energy of V_H^+ is 0.56 eV. In the absence of doping, the formation energy of V_H^+ has a minimum value of 0.81 eV. Thus, even quite far away from the H-rich limit, doping lowers the activation energy by 0.25 eV, which correlates to an increase in conductivity by almost two orders of magnitude at 673 K. Clearly, significant improvements in device performance can be realized through alkali-metal doping for a wide range of growth conditions.

Just as we discussed in the case of compensation by cation vacancies, there will be an attractive interaction between V_H^+ and the alkali metal acceptors. We have calculated complexes (in the neutral charge state) consisting of H vacancies and each of the four dopants. Binding energies evaluated using Eq. 2.36 are tabulated in Table 4.4.

Notably, the lowest binding energies are obtained for those dopants that also exhibited the lowest formation energies (Fig. 4.5). This result is promising, because trapping of the vacancy at the dopant would limit diffusion. Our results thus show that the dopants that are most easily incorporated (and hence have the largest impact on V_H^+ concentrations) will also do the least harm in terms of trapping.

In Table 4.4, we list the difference in ionic radius between the dopants and the host cations. We observe a clear correlation between the binding energies and the size difference such that the most size-similar dopants lead to the smallest binding energies. The same correlation is evident for formation energies (Fig. 4.5). For the optimal impurities (Na in CaH_2 and SrH_2, and K in BaH_2) the ionic radius is within 0.1 Å of the ionic radius of the host cation. We therefore conclude that dopant size is an important consideration [176]: the dopants that exhibit the best size match to the host cation have both the lowest formation energy and the lowest vacancy binding energy.

4.5.3 Optimizing Hydrogen Transport in Doped Systems

The results discussed above clearly indicate that doping can lower the activation energy for hydride conductivity. However, there is room for further improvement by using optimal growth and operating conditions. We saw that alkali metal dopants are optimally incorporated under H-rich conditions (Fig. 4.5). Unfortunately, the formation energy of V_{H}^{+} under H-rich conditions is high and serves to limit the activation energy. Under H-poor conditions, V_{H}^{+} has a significantly lower formation energy, but the formation energy of alkali metal acceptors is much larger.

There is no reason, however, to insist that the chemical potential conditions for dopant incorporation need necessarily be the same as those for device operation. The two issues can be decoupled. Dopants are incorporated during synthesis of the material, which we can choose to perform under H-rich conditions to maximize the incorporation of the acceptor dopants [Fig. 4.5(d)–(f)]. Once dopants are incorporated, the device can be operated under the conditions that are most favorable for hydrogen transport; namely, H-poor conditions, which favor V_{H} formation [Fig. 4.5(a)–(c)].

The underlying assumption here is that, once incorporated, the dopant impurities are not affected by the change in hydrogen chemical potential. That is actually a safe assumption. Synthesis is typically performed at higher temperatures than device operation. At the lower operating temperatures, the diffusivity of dopant atoms is very low, and they will essentially be locked into the lattice. In other words, under operating conditions, the mobility of hydrogen-related species vastly exceeds the mobility of the dopants.

Moving to hydrogen-poor conditions during operation will increase hydrogen vacancy concentrations over and above the V_{H}^{+} concentration established by alkali-metal doping; however, charge neutrality still applies. Additional V_{H}^{+} could be compensated by V_{Ae}^{-2}, but such large point defects may not form readily at the temperatures used for device operation. Even if that is not a limitation, we estimate that only slight improvements in ionic conductivity (on the order of a few %) over the values listed in Table 4.5 can be obtained. While charged defects are necessary for electrolyte applications, V_{H}^{0}, which becomes the dominant defect under H-poor conditions, could actually benefit other applications such as hydrogen storage. In this case, the product of defect concentration and the diffusion coefficient is the relevant quantity to consider. Taking BaH_2 as an example, the formation energy of V_{H}^{0} under H-poor conditions (0.29 eV) is 0.21 eV lower than that of V_{H}^{+} under H-rich conditions with K-doping (0.50 eV), leading to a concentration of V_{H}^{0} $\sim$40$\times$ greater than that of V_{H}^{+}. However, the migration barrier of V_{H}^{0} (0.53 eV) is 0.35 eV larger than that of V_{H}^{+} (0.18 eV), leading to a $\sim$400$\times$ decrease in the diffusion coefficient. Overall, incorporating additional V_{H}^{0} under H-poor conditions will contribute to a 10% improvement in hydrogen transport in BaH_2. While in this particular case the improvement is modest, we still consider it an important insight from our study that different choices of chemical potential conditions can and should be made for synthesis versus operation.

4.6 Conclusions

We have used first-principles calculations to study hydride ion transport mechanisms in the alkaline-earth hydrides CaH_2, SrH_2, and BaH_2. We showed that ionic transport is mediated by hydrogen vacancies; their low formation energy and small migration barrier results in a low overall activation energy for ionic conductivity.

We propose that doping with alkali metals can lower the activation energy for ionic conductivity even further by lowering the formation energy of V_H^+, thereby increasing the defect concentration in the material. We have found that the optimal dopants (in terms of formation energy and low trapping energies for V_H^+) are those closest in size to the host cations. The activation energy for hydride diffusion can be optimized by incorporating the dopants under H-rich conditions before switching over to H-poor conditions to take advantage of the low formation energy for hydrogen vacancies.

Our results also allow us to compare these three hydrides and assess their prospects as hydride ion conductors. BaH_2 emerges as the clear winner: the hydrogen vacancies that mediate diffusion have significantly lower formation energies (Fig. 4.5) than in CaH_2 and SrH_2. In addition, these hydrogen vacancies have the lowest binding energies both to cation vacancies and to alkali metal dopants (Table 4.4), reducing the impact of trapping. The size of the migration barriers for V_H also favors BaH_2 (Table 4.3): in the positive charge state, the barriers are comparable (and very low) in the three hydrides, while in the other charge states, BaH_2 exhibits the lowest barriers. Combined with experimental reports showing its excellent thermal stability [28], we conclude that BaH_2 is an especially attractive choice for applications requiring high hydride-ion conductivity, and we identify K as the optimal alkali-metal dopant. Doped CaH_2 and SrH_2 (with Na as the optimal dopant) may also have applicability in cases for which higher gravimetric densities of hydrogen are required.

We find that optimal synthesis conditions can produce ionic conductivities for hydride conduction that are equivalent to proton conductivities in the best proton-conducting oxides [117]. Our results indicate that the alkaline-earth hydrides are promising candidates for hydrogen electrolytes, with the potential to match or surpass the performance of solid-state proton conductors. Their properties make them well-suited for energy applications in systems requiring fast hydrogen kinetics.

Chapter 5

Defect Chemistry in La/Sr-Based Oxyhydrides

5.1 Permissions and Attributions

The content of Chapter 5 follows from work that has previously appeared in The Journal of Physical Chemistry C (Ref. [177]). This work was performed in collaboration with Dr. Leigh Weston.

5.2 Oxyhydrides

Beyond the metal hydrides discussed in Chapter 4, several so-called "oxyhydrides" have demonstrated promise as solid-state hydride-ion conductors. These systems belong to an expanding class of mixed-anionic crystals that offer expanded functionality relative to single-anion materials [24]. The oxyhydrides that have been demonstrated as hydride conductors include $LaSrCoO_3H_{0.7}$ [27], $BaTiO_{3-x}H_x$ [178], LaHO [179], and $La_{2-x-y}Sr_{x+y}LiH_{1-x+y}O_{3-y}$ [29]. These systems mostly crystallize as single or layered

perovskites, but with a significant fraction of hydrogen on the nominal oxygen lattice sites. These hydrogen species are anionic and, as in the alkaline-earth hydrides, their conductivity is mediated by hydrogen vacancies [27, 178, 179].

Kobayashi *et al*. showed that oxyhydrides of the form $La_{2-x-y}Sr_{x+y}LiH_{1-x+y}O_{3-y}$ can be synthesized, and that ionic conductivity increases with increasing hydrogen content [29]. Recent computational studies have supported the notion that hydride ions are the primary charge carriers by finding low energetic barriers to vacancy-mediated hydride diffusion in the $x = 0$ series of oxyhydrides [180, 181]. Bai *et al*. used *ab initio* molecular dynamics simulations to show that the Sr-containing materials, $LaSrLiH_2O_2$ (LSLHO) and Sr_2LiH_3O (SLHO), were signficantly more conductive than La_2LiHO_3 (LLHO) [180]. However, stability is a concern: Liu *et al*. concluded, by studying defect formation under different synthesis conditions, that the oxyhydrides are inherently unstable [181].

In light of these materials' high hydride conductivity, it is important to determine how their structural and electronic properties relate to stability. In this chapter, we follow the methodology for defect calculations described in Section 2.3 and focus specifically on the $y = 0$ (LLHO) and $y = 2$ (SLHO) oxyhydrides, the stoichiometric endpoints of the $x = 0$ series. LLHO has been demonstrated in model hydride fuel cells and is the most stable [29, 182]. SLHO is more conductive; however, it is not as easily stabilized [29]. We show that LLHO is indeed stable under a range of typical synthesis environments, while SLHO can be synthesized as a metastable compound under carefully chosen synthesis conditions, which we identify. We also shed light on the most probable structure of SLHO, which we show to have a high degree of disorder. By optimizing synthesis conditions, we can maximize the concentration of H vacancies in SLHO and, hence, the ionic conductivity, thus rendering the material more attractive as a solid-state hydrogen electrolyte.

5.3 Methodology

Here, we utilize a plane-wave cutoff energy of 400 eV for our defect calculations. The PAW pseudopotentials used in our calculations treat the following electrons as valence states: La $5s^2\ 5p^6\ 6s^2\ 5d^1$, Sr $4s^2\ 4p^6\ 5s^2$, Li $2s^1$, and O $2s^2\ 2p^4$. For the bulk primitive cells, an $8\times8\times2$ k-point grid is used to integrate over the Brillouin zone of the orthorhombic lattice; for the supercell calculations, a single special k-point in a $2\times2\times2$ grid is used.

To calculate defect formation energies, supercells are constructed with dimensions $3a \times 3b \times 1c$, containing nine unit cells (18 formula units) and 126 atoms in total. These supercells are used to simulate one of several intrinsic point defects: anion vacancies (V_{H} and V_{O}), cation vacancies (V_{La}, V_{Li}, and V_{Sr}), hydrogen interstitials (H_i), and anionic antisite defects (H_{O} and O_{H}).

We derive the chemical potential stability for both quaternary oxyhydrides in Appendix A. There, we identify specific chemical potentials for the purposes of presenting our results; formation energies at other chemical-potential values can be readily obtained using the expression for formation energy (Eq. 2.15). In principle, the chemical potentials should be chosen to lie within the region of stability for the oxyhydride; however, since SLHO does not display such a region of stability in our chemical potential space, our choices of chemical potentials reflect regions of metastability.

5.4 Properties of Ordered Oxyhydrides

Figure 5.1 shows unit cells for the layered structures (a) LLHO and (b) SLHO. The bulk properties for ordered structures are summarized in Table 5.1; we note, however, that experimental reports suggest the presence of disorder on anion sites, particularly

in the case of SLHO [29]. Both structures are orthorhombic Ruddlesden-Popper (layered perovskite) phases with one intermediate offset perovskite layer. LLHO belongs to the space group $I4/mmm$ (No. 139) [29]; we find that the lowest energy unit cell for SLHO belongs to the $Cmm2$ (No. 35) space group. The octahedral units in both cells are comprised of Li atoms that are sixfold coordinated by O and H atoms; each octahedron contains four O atoms and two H atoms in LLHO, and one O atom and five H atoms in SLHO. In SLHO, unlike in LLHO, the apical (c-axis) coordination is mixed, with an O anion on one side and a H anion on the other. Additionally, the (ab-)planar sites in SLHO are fully occupied by H anions; energetically, this configuration is more stable than any in which O anions appear on planar sites. As a result, the octahedra are distorted such that the apical bond connecting the Li and O atoms is significantly shorter (≈ 1.89 Å) than that connecting Li to the apical H atom (≈ 2.49 Å). We note that the calculations of Liu *et al*. assume the higher-energy $I4/mmm$ structure of SLHO, in which the apical sites are solely occupied either by H or by O [181]. The La and Sr atoms occupy the A sites of the perovskite motifs in their respective structures. Notably, these two structures have vastly different enthalpies of formation per formula unit: –18.96 eV for LLHO and –2.19 eV for SLHO (see Appendix A, Table A.1). The increased hydrogen content of SLHO may account for this difference, along with the larger bond strength of Li–O bonds compared with Li–H bonds. LLHO has four Li–O bonds per octahedron, while SLHO only has one.

5.4.1 Defect Chemistry in LLHO

We plot defect formation energies for LLHO in Fig. 5.2. The species we consider are anion vacancies (V_{H} and V_{O}), cation vacancies (V_{La}, V_{Li}, and V_{Sr}), H interstitials (H_i), and anionic antisite defects (H_{O} and O_{H}). Our formation energies are based on

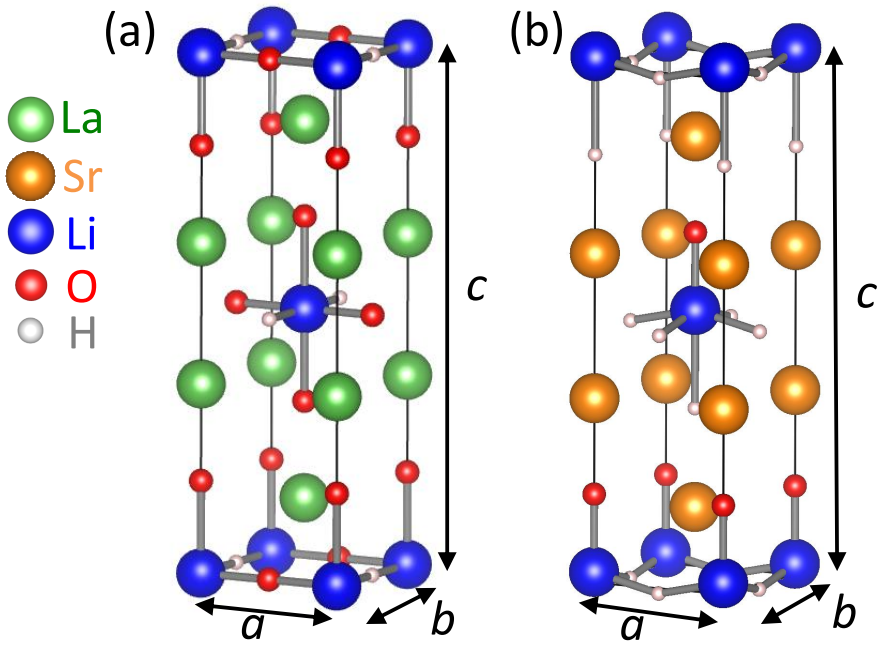

Figure 5.1: (a) Unit cells of (a) La_2LiHO_3 and (b) Sr_2LiH_3O.

Table 5.1: Calculated and Experimental [29] Bulk Properties for La_2LiHO_3 and Sr_2LiH_3O.

Material	Method	a (Å)	b (Å)	c (Å)	Band Gap (eV)
La_2LiHO_3	Calc.	3.56	3.77	12.84	3.19
	Exp.	3.58	3.76	12.97	–
Sr_2LiH_3O	Calc.	3.70	3.70	13.08	3.83
	Exp.	3.72	3.72	13.32	–

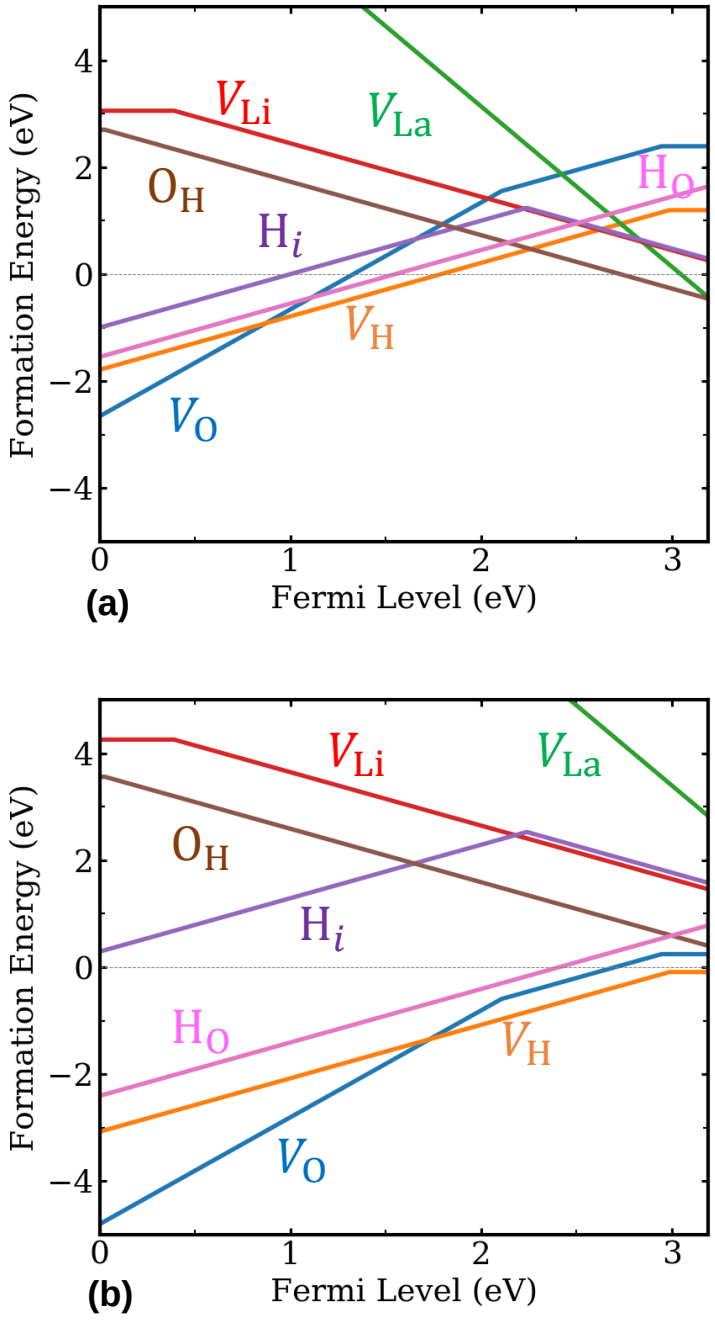

Figure 5.2: Formation energies of native point defects in La_2LiHO_3 as a function of Fermi level, as determined at the (a) H-rich and (b) H-poor conditions identified in Appendix A.

chemical potentials for H-rich and H-poor conditions, which are selected to reflect the range of possible growth conditions. We plot the formation energies as a function of Fermi level. For the conditions presented in Fig. 5.2(a), the Fermi level is pinned by the crossing of the formation-energy lines for V_{H}^{+} and $\mathrm{O}_{\mathrm{H}}^{-}$, about 2.3 eV above the VBM. In this case, the defect chemistry is dominated by large and approximately equal concentrations of V_{H}^{+} and $\mathrm{O}_{\mathrm{H}}^{-}$. Notably, V_{H} has a very low formation energy, despite the choice of H-rich chemical potentials. For choices of $\Delta\mu_{\mathrm{H}}$ just off the H-rich limit, $\mathrm{H}_{\mathrm{O}}^{+}$ can surpass V_{H}^{+} as the most-favorable donor defect.

Under the H-poor conditions depicted in Fig. 5.2(b), the lowest-energy defect is the hydrogen vacancy, V_{H}, which acts as a donor and is not compensated by any acceptor-type defects. The lowest-energy charge state of V_{H} at the CBM is neutral, with charge localized at the defect site, and the formation energy is slightly negative—as a result, the material will be unstable at the H-poor limit, but it can be stabilized by moving to slightly less H-poor conditions. The position of the (+/0) transition level for V_{H} indicates that it could give rise to *n*-type conductivity. Electrical conductivity will destroy the material's potential for ionic applications. Kobayashi *et al*. [29] showed that as-synthesized LLHO is exclusively an ionic conductor, suggesting that synthesis can indeed be performed under conditions that are closer to H-rich, for which the Fermi level is pinned well below the CBM.

5.4.2 Defect Chemistry in SLHO

Unlike LLHO, SLHO does not have a definite chemical potential stability window: for any choice of chemical potentials, at least one secondary phase will form preferentially to SLHO (see Section A.3). We therefore examine the defect chemistry under various chemical potential conditions corresponding to metastable regions. In

Fig. 5.3(a), we examine the change in defect chemistry for varying $\Delta\mu_{\mathrm{O}}$ while keeping $\Delta\mu_{\mathrm{H}}$ fixed at 0 eV. Our plot shows the formation energies of each defect in our system at the Fermi level determined by charge compensation of the lowest energy species. Therefore, at any value of $\Delta\mu_{\mathrm{O}}$, the two lines with the lowest formation energy indicate the dominant defect species. For $\Delta\mu_{\mathrm{O}} > -3.27$ eV, the Fermi level is pinned by defects having a negative formation energy, which implies that the ordered structure of SLHO will not be stable. Defect formation energies become positive for $\Delta\mu_{\mathrm{O}} < -3.27$ eV, at which point $\mathrm{O}_{\mathrm{H}}^{-}$ compensates with H_i^{+}. Moving to more O-poor conditions, at $\Delta\mu_{\mathrm{O}} < -3.56$ eV, $\mathrm{H}_{\mathrm{O}}^{+}$ replaces H_i^{+} as the compensating donor. These values of $\Delta\mu_{\mathrm{O}}$ require low oxygen partial pressures, even at synthesis temperatures above 1000 K [29]; however, such conditions are experimentally achievable [183, 184].

We can also consider more H-poor conditions. In Fig. 5.3(b), we plot defect formation energies for $\Delta\mu_{\mathrm{H}} = -1$ eV with the Fermi level again varying to maintain charge compensation. Here, defect formation energies will be pinned at positive values starting at $\Delta\mu_{\mathrm{O}} = -4.85$ eV, where V_{H}^{+} and $\mathrm{O}_{\mathrm{H}}^{-}$ are the dominant species present. At $\Delta\mu_{\mathrm{O}} = -5.15$ eV, $\mathrm{H}_{\mathrm{O}}^{+}$ becomes more energetically favored than V_{H}^{+}. The V_{H}^{+} species in question lies in the *ab*-plane; the apical species is about 30 meV per formula unit higher in energy. Previous studies show that hydride ion migration in plane proceeds favorably via diffusion of planar V_{H}^{+} [180, 181]; thus, growth conditions should be chosen to produce as many V_{H}^{+} defects as possible. It can be shown that V_{H}^{+} surpasses H_i^{+} as the dominant native donor species around $\Delta\mu_{\mathrm{H}} = -0.2$ eV, so partial pressures of H_2 or H_2O must be chosen to at least meet this chemical potential.

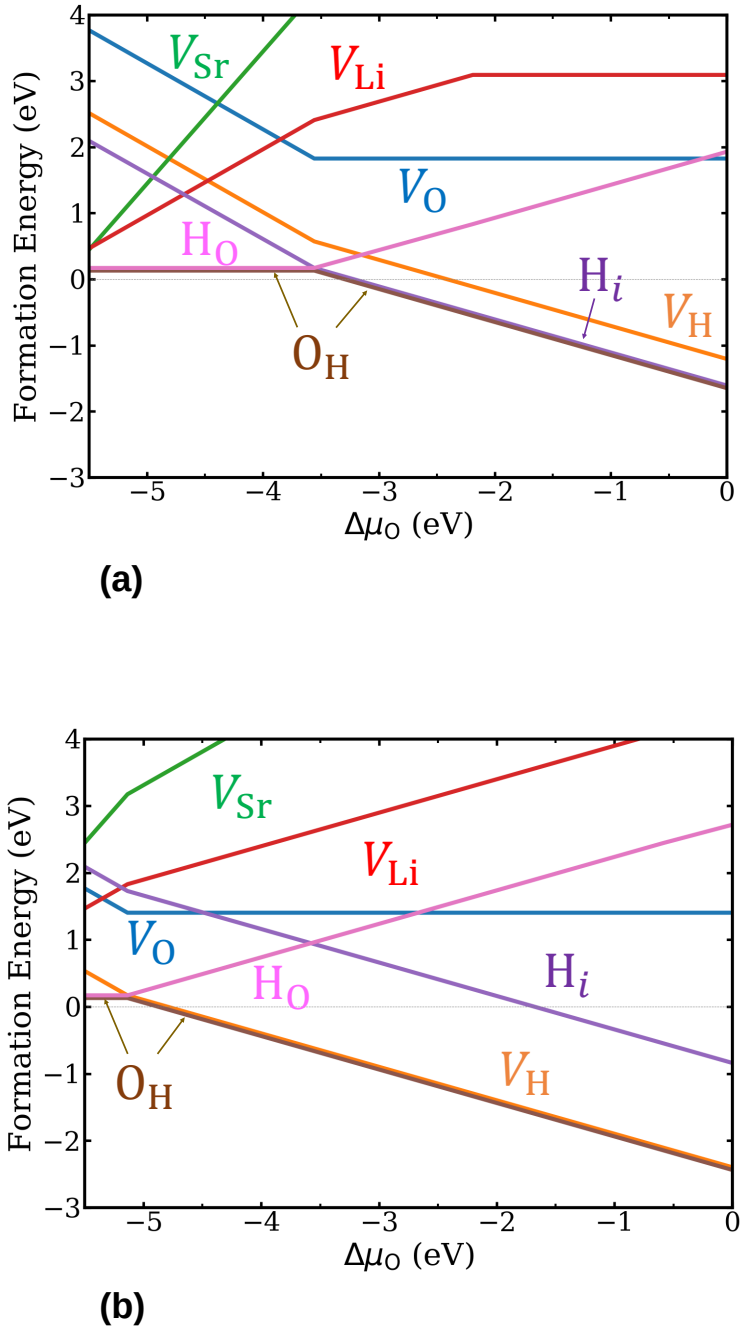

Figure 5.3: Formation energies of native point defects in Sr_2LiH_3O, determined at the Fermi level position corresponding to charge neutrality of the lowest energy defects, as a function of $\Delta\mu_O$ at (a) $\Delta\mu_H = 0$ and (b) $\Delta\mu_H = -1$ eV.

5.5 Disorder in SLHO

5.5.1 Disordered Supercells

The defect chemistry of SLHO implies that it will be considerably disordered. We first investigate this disorder by considering variations in the apical ordering of the SLHO octahedra, which amounts to forming pairs of O_H^- and H_O^+ defects. To this end, we considered fourteen characteristic supercells in which the positions of apical H and O atoms are swapped. Our selections were guided by several considerations. First, bringing too many O atoms close together—as can be accomplished by inverting one of the Ruddlesden-Popper layers—was unfavorable. Second, occupying both apical sites with O leads to higher-energy structures. Third, placing O anions on anionic sites in the *ab*-plane was also high in energy. This last observation agrees well with our calculations for defects in the ordered SLHO structure: we found that O_H defects are more stable on apical sites than in the *ab*-plane by between 20 and 30 meV per formula unit. By randomly selecting structures that took those findings into account, we identified a configuration with an energy more than 50 meV per formula unit lower than pristine SLHO. This disordered structure is shown in Fig. 5.4(a), with the ordered structure shown for comparison in Fig. 5.4(b).

5.5.2 Entropic Disorder

We can also consider this apical disorder from an entropic perspective. Configurational entropy is defined as $S = k_B \ln Z$, where k_B is Boltzmann's constant and Z is the number of possible configurations. At finite temperature, configurational entropy lowers the free energy by TS. Assuming that exactly one apical site must be occupied by O, there are two possible configurations for each octahedron; with N octahedra per

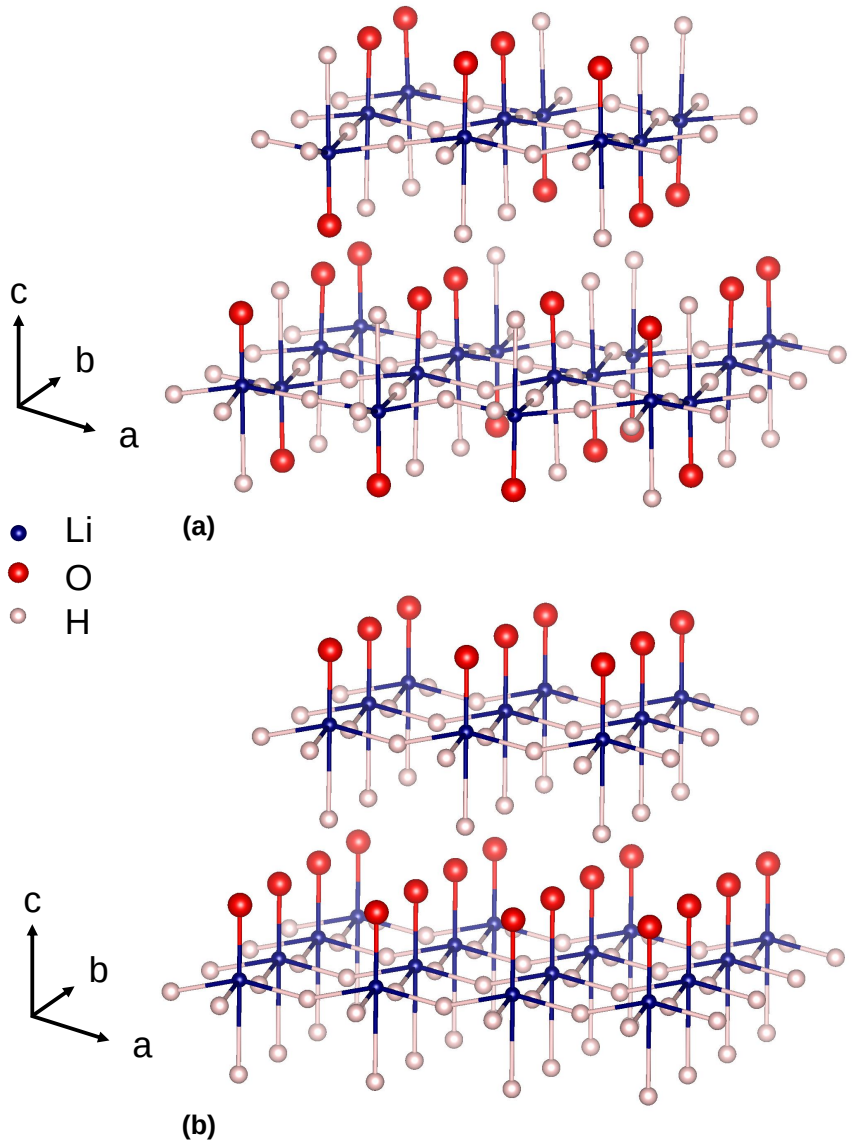

Figure 5.4: (a) The lowest-energy disordered supercell of Sr_2LiH_3O, in which apical H and O atoms have been swapped from their positions in (b) the pristine cell. Sr atoms are not shown.

supercell, $Z = 2^N$, and $S = k_B N \ln 2$. At typical synthesis temperatures, on the order of 1000 K [29, 185], the free energy will be lowered by about 60 meV per formula unit.

5.5.3 Defect-Assisted Stabilization

Our defect calculations, as summarized in Fig. 5.3, imply that SLHO will also experience disorder in the form of high quantities of V_{H}^{+}, and, at more H-rich conditions, H_i^{+}. We have calculated the formation energy of compensating planar V_{H}^{+} and apical $\mathrm{O}_{\mathrm{H}}^{-}$. At the O-rich, H-rich limit, this defect pair has a formation energy of -3.15 eV, or about -0.18 eV per formula unit. Such an energy change strongly suggests that the as-synthesized structure of SLHO will deviate considerably from the pristine structure.

Taking the configuration shown in Fig. 5.4(a), we calculate the formation energies of oxygen- and hydrogen-related defects. Our results are shown in Fig. 5.5(a) alongside comparison results for the pristine supercell [Fig. 5.5(b)]. For the chemical potentials, we choose $\Delta\mu_{\mathrm{O}} = -3.3$ eV and $\Delta\mu_{\mathrm{H}} = 0$, using Fig. 5.3(a) to identify a choice of chemical potentials for which the ordered SLHO structure has positive defect formation energies. The band gap widens by about 0.3 eV in the disordered structure, and some quantitative differences in formation energies and charge-state transitions occur. However, the qualitative conclusions remain the same, particularly for the defects most important for charge equilibrium. As in the pristine structure, V_{H}^{+} will be favored by roughly 30 meV per formula unit to form on planar sites compared with apical sites. $\mathrm{O}_{\mathrm{H}}^{-}$ will form more readily on apical sites by a similar energetic amount. Notably, the formation energy of the lowest-energy defects, H_i^{+} and $\mathrm{O}_{\mathrm{H}}^{-}$, increases in the disordered system relative to the pristine, which lends further weight to our conclusion that the disordered structure is more stable.

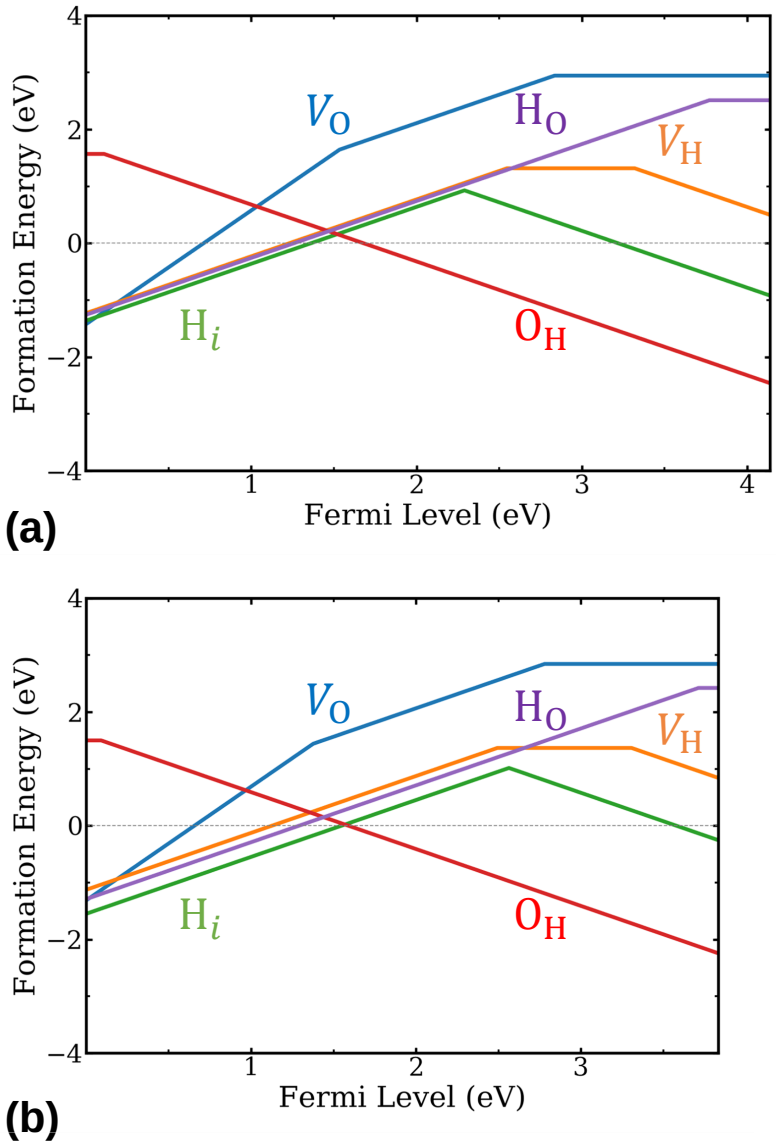

Figure 5.5: (a) Formation energy of oxygen- and hydrogen-related defects in the disordered structure of Sr_2LiH_3O shown in Fig. 5.4(a). (b) The same defects in the ordered supercell shown in Fig. 5.4(b). Both figures assume $\Delta\mu_H = 0$ eV and $\Delta\mu_O = -3.3$ eV.

5.6 Implications of Disorder for Hydride Conductivity

5.6.1 Structural Considerations

We can now consider what role the defect chemistry plays in determining the ionic conductivity in these systems. We have found LLHO to be stable over a definite range of chemical potentials, and our calculations of defect formation energies show that V_{H}^{+} and $\mathrm{O}_{\mathrm{H}}^{-}$ will be the most common defects for most chemical potential conditions. Previous studies have shown that hydride ion transport in LLHO proceeds via migration of V_{O}^{+2} onto lattice H sites, which leads to the formation of far more stable $\mathrm{H}_{\mathrm{O}}^{+}$ and V_{H}^{+} defects [181]. The converse reaction, where a V_{H}^{+} defect migrates to a nearby $\mathrm{H}_{\mathrm{O}}^{+}$ species, is far more energetically prohibitive, because it forms a high-energy V_{O}^{+2} defect. Either way, because half of all planar anion sites in LLHO are occupied by O atoms [Fig. 5.1(a)], high-energy V_{O} species must be involved in hydride diffusion. The high associated energy barriers will limit ionic conductivity, as previous studies have observed [180, 186].

SLHO, in contrast to LLHO, has a favorable structure for hydride conduction, because all of the planar octahedral sites are occupied by H, and the migration barrier for V_{H}^{+} is low. As outlined in Fig. 5.3, $\mathrm{O}_{\mathrm{H}}^{-}$ serves as a compensating acceptor for three different species depending on chemical potential: for very O-poor conditions, $\mathrm{H}_{\mathrm{O}}^{+}$, and at higher oxygen chemical potentials either V_{H}^{+} or H_{i}^{+}, depending on the hydrogen chemical potential. We note that Liu *et al*. [181] did not consider H_{O} in their defect study. The presence of apical antisite pairs provides a general stabilizing effect on bulk SLHO compared with the pristine structure. This result agrees with other analyses of anionic disorder in oxyhydrides [180].

Even more significant than anionic disorder is the impact of V_H^+ as a stabilizing defect when compensating with O_H^-. V_H^+ is the most important defect for ionic transport; specifically, the configuration of V_H^+ in the *ab*-plane has the lowest migration barrier [180]. Our calculations also show that the formation energy of planar V_H^+ is roughly 0.6 eV lower than that of apical V_H^+. These two effects combine to make diffusion in the *ab*-plane significantly faster than along the *c*-direction; this anisotropy was also observed by Bai *et al*. [180] In order to maximize the vacancy content, synthesis conditions should be away from the H-rich limit, where H_i^+ will form more readily. Additionally, very O-poor conditions, for which H_O^+ will be preferred over V_H^+, should be avoided.

5.6.2 Hydride Activation Energy

We now estimate how these different synthesis conditions affect the activation energies for hydride diffusion. Previous computational studies have used the NEB method to compute pertinent migration barriers in LLHO and SLHO. Liu *et al*. calculated an in-plane barrier for V_H^+ of 0.30 eV in SLHO [181], while Bai *et al*. determined the out-of-plane barrier to be between 0.68 eV and 0.93 eV [180]. For LLHO, Liu *et al*. calculated a barrier of 0.21 eV for V_O^{+2} to move to a nearby hydrogen lattice site, forming H_O^+ and V_H^+, and 0.78 eV for H_O^+ to move to a V_H^+ site, forming V_O^{+2}; alternatively, V_H^+ can move to an oxygen site with a barrier of 1.21 eV, forming V_O^{+2} and O_H^- [181]. Our own NEB calculations, based upon ordered supercells, agree well with these results. We expect that disordered structures for SLHO, like that of Fig. 5.4(a), should have nearly identical migration barriers, as the planar occupation is identical to that of the ordered structure.

For LLHO, under the H-rich conditions shown in Fig. 5.2(a) and at the Fermi-level position corresponding to charge neutrality, V_{O}^{+2} has a formation energy of 1.86 eV, and V_{H}^{+} has a formation energy of 0.47 eV. Either defect, with their corresponding migration barriers, can lead to hydride migration: V_{O}^{+2} has an activation energy of 2.07 eV, while V_{H}^{+} has an activation energy of 1.68 eV. These values are quite large and will remain so irrespective of changes in formation energy resulting from different choices of chemical potentials. In the case of SLHO, we can estimate the activation energy for V_{H}^{+} conduction under the conditions depicted in Fig. 5.3(b) ($\Delta\mu_{\mathrm{H}} = -1$ eV). For $\Delta\mu_{\mathrm{O}} = -5.15$ eV, the formation energy of V_{H}^{+} is 0.15 eV, corresponding to an activation energy of 0.45 eV. The formation energy of V_{H}^{+} under the same conditions remains the same in the disordered structure of Fig. 5.4(a); therefore, this activation energy should be representative of disordered structures as well. Out-of-plane migration, having a larger barrier, would have an activation energy of at least 0.83 eV, which explains the anisotropic hydride conduction. Because V_{H}^{+} can form quite readily under more O-rich conditions, it is likely that measured activation energies would actually be even lower, due to a decrease in formation energy. The resulting values for E_a in plane are on par with the activation energy for proton conduction in $BaZrO_3$, one of the best solid-state proton conductors (0.4–0.6 eV) [117], and superior to our calculated activation energies for hydride conduction in BaH_2 (0.68 eV, see Section 4.5.2).

5.7 Conclusions

In summary, we have used a first-principles approach to study the defect chemistry and stability of oxyhydrides of the form $La_{2-y}Sr_yLiH_{1+y}O_{3-y}$. LLHO ($y = 0$) has a well-defined region of stability. Its most prevalent defects are V_{H} and O_{H}. However,

high ionic conductivity in LLHO requires the creation of V_O, and due to their high formation energies, they will form in limited quantities.

SLHO ($y = 2$) suffers from poor chemical stability. However, disordered forms of SLHO are significantly more stable and will form more readily. We find that O_H^- serves as a stabilizing defect that compensates with one of several H donor species: H_O, H_i, and V_H. V_H is the most important defect for ionic conduction in SLHO, because it can migrate with low barriers, particularly within the *ab*-plane [180]. This defect can be stabilized by growing at O-rich conditions and below the H-rich limit. By properly characterizing the structure and stability of SLHO, and by identifying the synthesis conditions necessary for maximizing its ionic conductivity, our results can guide its adoption in solid-state hydrogen fuel cells.

Most likely, devices based on oxyhydrides will rely upon solid solutions of LLHO and SLHO [29, 180, 181]. These intermediate compositions will provide a tradeoff between stability and conductivity, and defect properties can be estimated by interpolating between the endpoints. The approach of using solid solutions to combine the desired properties of two endpoint compounds is similar to that discussed in Chapter 3 for the case of $BaZrO_3$–$BaCeO_3$ alloys, which marry the chemical stability of $BaZrO_3$ with the high proton conductivity of $BaCeO_3$ [122].

Chapter 6

Hydride Conductivity in Nitride Hydrides

6.1 Permissions and Attributions

The content of Chapter 6 follows from work that has has previously appeared in ACS Applied Energy Materials (Ref. [187]).

6.2 Nitride Hydrides: A New Frontier in Mixed-Anionic Crystals

One largely unexplored class of mixed-anionic materials are nitride hydrides (or "hydridonitrides" [188]), which containing nitrogen and hydrogen. Researchers have known about the high hydrogen storage capacity (up to 11.5 wt%) of the Li–N–H system for several decades [189], and efficient synthesis methods to generate Li_4HN are available [190]. Alkaline-earth nitride hydrides, such as Sr_2NH and Ba_2NH, have

also been synthesized [191, 192], and they have been shown to exhibit high hydride diffusion [193, 194].

Two groups have synthesized and characterized Sr_2LiH_2N (SLHN) [195, 196], though ion transport was not measured. This material has a very similar structure to the $La_{2-x}Sr_xLiH_{1+x}O_{3-x}$ oxyhydrides discussed in Chapter 5 (see Fig. 5.1). Kobayashi *et al*. noted that hydride conductivity increases as the Sr-to-La ratio increases in LSLHO [29]; however, as we have shown, the stability of the oxyhydride decreases with increasing Sr content (Section 5.4). Thus, it is encouraging that the first experimental reports on the analogous nitride hydride system center on the Sr-containing compound. The structure of SLHN also contains free space in the form of linear cavities for hydride ions to migrate through the crystal, potentially providing pathways for hydride diffusion [195]. These features suggest that it should exhibit high hydride conductivity.

In order to evaluate SLHN's prospects as a solid-state hydride electrolyte, we focus on a region of chemical potentials in SLHN for which defect formation energies are positive. We identify hydrogen interstitials and vacancies as the most common native defects in SLHN. These defects, interstitials in particular, mediate the hydride conductivity. Our calculated activation barrier for hydride diffusion is lower than the measured barrier in LaHO [179], the most conductive oxyhydride known. Among hydride conductors studied to date, SLHN is unusual in that interstitial hydrogen (rather than the hydrogen vacancy) is the primary defect driving hydride migration. We also assess the energetics of oxygen incorporation, highlighting the need to protect the material from oxygen. Finally, in analogy with the La/Sr oxyhydride system, we discuss the prospects of a hypothetical La-containing material with the chemical formula La_2LiHN_2 (LLHN), which could, in principle, marry the advantages of chemical stability and high hydride conductivity. However, we find LLHN to be both unstable

and less conductive than SLHN, making it less technological interesting. In sum, our results clearly show that SLHN is an excellent hydride conductor and one that merits further experimental exploration for use in solid-state hydride fuel cells.

6.3 Methodology

For the work described here, we apply PAW pseudopotentials with a plane-wave cutoff of 500 eV. The Sr $4s^2$ $4p^6$ $5s^2$, La $5s^2$ $5p^6$ $6s^2$ $5d^1$, Li $2s^1$, and N $2s^2$ $2p^3$ electrons are treated explicitly as valence. We simulate orthorhombic unit cells for SLHN and LLHN, each containing four formula units (see Fig. 6.1), using an $8\times4\times2$ k-point grid to integrate over the Brillouin zone. For our defect calculations, we construct $3\times2\times1$ supercells to ensure a length greater than 10 Å in each Cartesian direction. We use NEB calculations (see Section 2.4.1) to evaluate the energetic barriers associated with defect migration, using the PBE GGA functional with three intermediate images along the minimum energy path.

6.4 Results and Discussion

6.4.1 Structure

Experimental studies suggested two possible structures for SLHN, both with *a*-, *b*-, and *c*-axes oriented at right angles relative to one another. Both derive from fourfold-coordinated planar motifs of Li bonded to four anions, one N and three H, with Sr cations simply providing charge balance. In the Li–N–3H motifs, the N anion and one of the H anions are oriented apically along the long *c*-axis relative to Li. The other two H anions could be oriented either along the *a*- or *b*-axes relative to Li. In Ref. [195],

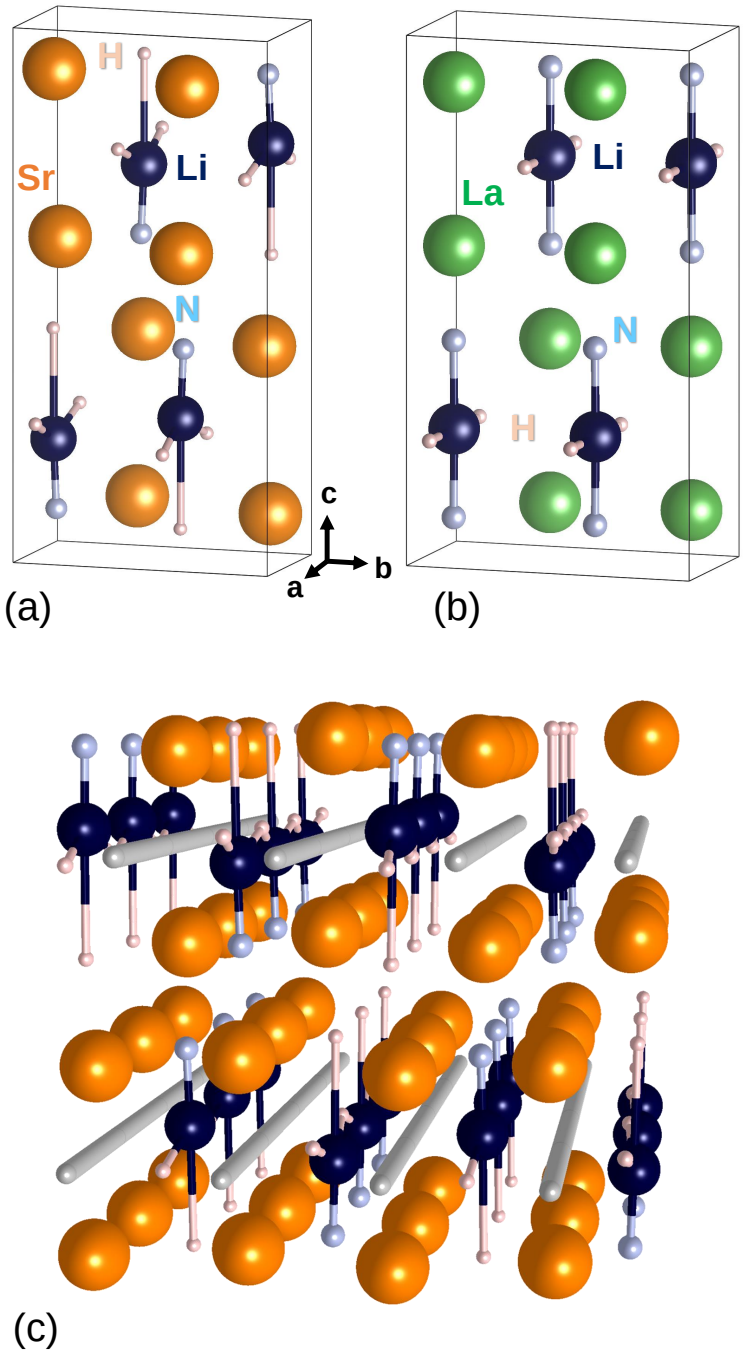

Figure 6.1: (a) Unit cells of (a) Sr_2LiH_2N and (b) La_2LiHN_2. (c) A 3×2×1 supercell of SLHN, with empty channels for hydride migration indicated with thick lines.

crystallographic analysis revealed a preference for these H anions to lie uniformly along one axis [chosen to be the *a*-axis in Fig. 6.1(a)], thereby forming chains of Li–N–3H motifs connected by shared H anions along the *a*-axis [see Fig. 6.1(c)]. That structure is orthorhombic, with a *Pnma* space group (No. 62). The authors of Ref. [196], on the other hand, proposed a tetragonal structure (space group $I4/mmm$, No. 139) with $a = b$. Their methods were not sensitive to the location of H atoms, but their structure would be consistent with the same apical H ordering, while the remaining two H atoms would be randomly oriented along the *a*- or *b*-axes relative to Li (i.e., the planar Li motifs lie either in the *ac*- or the *bc*-plane). Structural parameters for both experimental structures are listed in Table 6.1.

For our purposes, we assume the orthorhombic *Pnma* structure of Ref. [195] for both SLHN and the hypothetical material LLHN. We found the tetragonal structure of Ref. [196] difficult to be higher in energy in our calculations. We show the orthorhombic unit cells for SLHN in Fig. 6.1(a) and for LLHN in Fig. 6.1(b), and we list our calculated bulk parameters in Table 6.1 alongside experimental parameters for SLHN. Per unit cell, there are two Li–N–3H motifs centered at $0.25c$ and two centered at $0.75c$, each with a separation of $0.5b$. These groupings of two motifs are separated from each other by an offset of $(0.5a, 0.25b, 0.5c)$. As can be seen in Fig. 6.1(a), Li–N–3H motifs that lie in the same *ab*-plane but do *not* share a H anion have alternating apical order; i.e., if the N anion is above Li in one motif, it will be below Li in the other. The orthorhomic structure contains empty channels separating neighboring Li atoms along the *b*-axis, as shown schematically in Fig. 6.1(c).

Our calculated band structure for SLHN is shown in Fig. 6.2. We find the band gap to be indirect, with a value of 2.40 eV. The CBM is located at Γ, while the VBM is located between the U and R points in the Brillouin zone. The direct band gap at Γ (2.49 eV) is only slightly larger. The band gap is wide enough that suppressing

Table 6.1: Calculated and experimental bulk properties for Sr_2LiH_2N and La_2LiHN_2.

Material	Method	a (Å)	b (Å)	c (Å)	Volume (Å^3)	$E_{g,\mathrm{dir}}$ (eV)	$E_{g,\mathrm{ind}}$ (eV)
Sr_2LiH_2N	Calc.	3.79	7.23	14.69	402.81	2.49	2.40
	Ref. [195]	3.70	7.47	13.30	367.60		
	Ref. [196]	3.81	7.62	13.72	398.46		
La_2LiHN_2	Calc.	3.84	7.24	13.08	363.38		

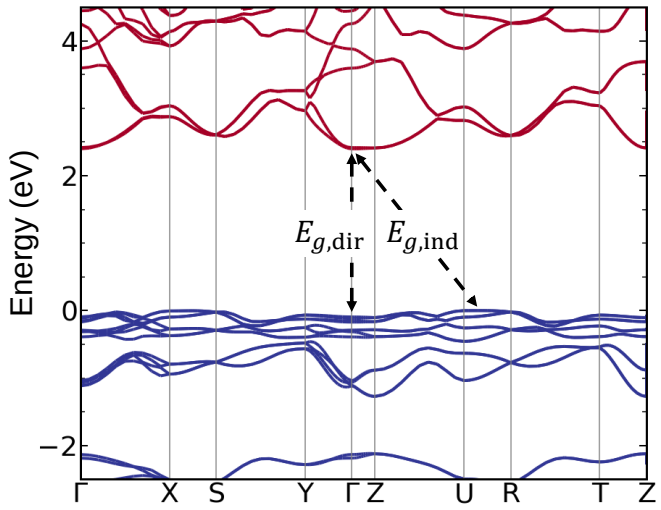

Figure 6.2: The band structure of SLHN.

electrical conductivity may be possible, which would enable SLHN to be used as an ionic electrolyte.

6.4.2 Stability

In Fig. 6.3, we plot the phase diagram for SLHN in the $\Delta\mu_{\mathrm{Sr}}$-vs.-$\Delta\mu_{\mathrm{H}}$ plane at three selected values of $\Delta\mu_{\mathrm{N}}$. Our procedure for obtaining these phase diagrams is discussed in Appendix A, Section A.4. Our calculated enthalpies of formation for SLHN and its limiting phases are listed in Table A.1, alongside experimental values where available. Our results show that, at T=0, SLHN is not stable: certain binary Sr–N

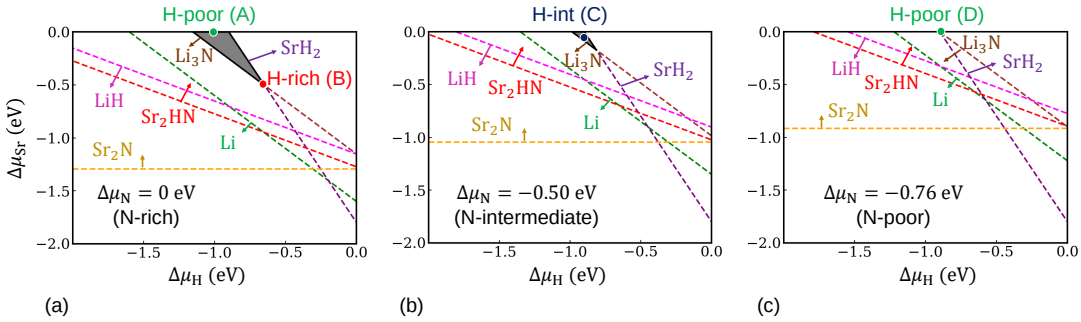

Figure 6.3: Phase diagram for Sr_2LiH_2N in $\Delta\mu_{Sr}$-vs.-$\Delta\mu_H$ phase space for three choices of $\Delta\mu_N$. N-rich conditions are shown in (a), N-poor conditions in (c), and in (b), an intermediate choice of $\Delta\mu_N$ is used. The dots indicate particular choices of chemical potentials, tabulated in Table 6.2, that are used to display the results of our defect calculations. The region encompassing our chosen chemical potentials is shaded in gray. In Fig. 6.3(c), this region collapses to a single point. Note that the conditions are labeled as (A), (B), (C), and (D) to correspond with the panels in Fig. 6.4.

compounds (such as Sr_2N) and also Sr_2HN will form preferentially at the chemical potentials where we would otherwise expect to observe the SLHN phase. Given that experimental reports have not observed Sr_2HN or any binary Sr–N phases during synthesis of SLHN [195, 196], we infer that careful synthesis techniques are able to create at least a metastable material. We hypothesize that the formation of other phases is kinetically suppressed, and/or the SLHN phase is entropically stabilized at finite temperature. We identify a region of metastability, shaded in gray in Fig. 6.3, where we will study the energetics of defect formation. For the purposes of displaying the results of the defect calculations we will refer to conditions indicated by dots in Fig. 6.3, for which we also tabulate values for $\Delta\mu$ in Table 6.2.

We also calculated the stability phase space for LLHN, again considering several binary and ternary compounds. Again, we found no chemical potentials for which LLHN will be stable. The main culprit in limiting LLHN's stability is LaN, which is

Table 6.2: Selected chemical potentials, labeled (A), (B), (C), and (D), referring to points indicated in the chemical potential stability diagrams in Fig. 6.3.

Condition	$\Delta\mu_{Sr}$ (eV)	$\Delta\mu_{Li}$ (eV)	$\Delta\mu_{H}$ (eV)	$\Delta\mu_{N}$ (eV)	$\Delta\mu_{O}$ (eV)
N-rich/H-poor (A)	0	–1.15	–1.03	0	–5.63
N-rich/H-rich (B)	–0.51	–0.90	–0.65	0	–5.13
N-int/H-int (C)	–0.09	–0.78	–0.88	–0.50	–5.54
N-poor/H-poor (D)	0	–0.65	–0.90	–0.76	–5.63

preferred to LLHN over a wide range of conditions. Coupled with the lack of experimental evidence of its existence, it appears unlikely that LLHN can be stabilized.

6.4.3 Defect Formation

Native Point Defects

We plot the formation energy for various point defects in Fig. 6.4, calculated using Eq. 2.15 as a function of E_F over the band gap for the four chemical potential conditions listed in Table 6.2. With regard to defects on H sites (vacancies and substitutional species), we have systematically investigated their formation on apical sites (collinear with Li along the *c*-axis) and on sites along the *a*-axis relative to Li. For all the defects we examined, the latter are lower in energy. As for H_i, its location depends on the charge state: H_i^- forms preferentially between two Li atoms along the *b*-axis, while H_i^+ bonds with a N anion. As can be seen in Fig. 6.4, the defect chemistry is highly dependent on the chemical potentials.

Under N-rich/H-poor conditions, shown in Fig. 6.4(a), Sr_{Li}, V_{Li}, and N_H have negative formation energies at the Fermi level determined by charge neutrality, indicating that SLHN will be unstable. However, at other conditions, the formation energy at which defect compensation occurs is positive. One commonality of these other con-

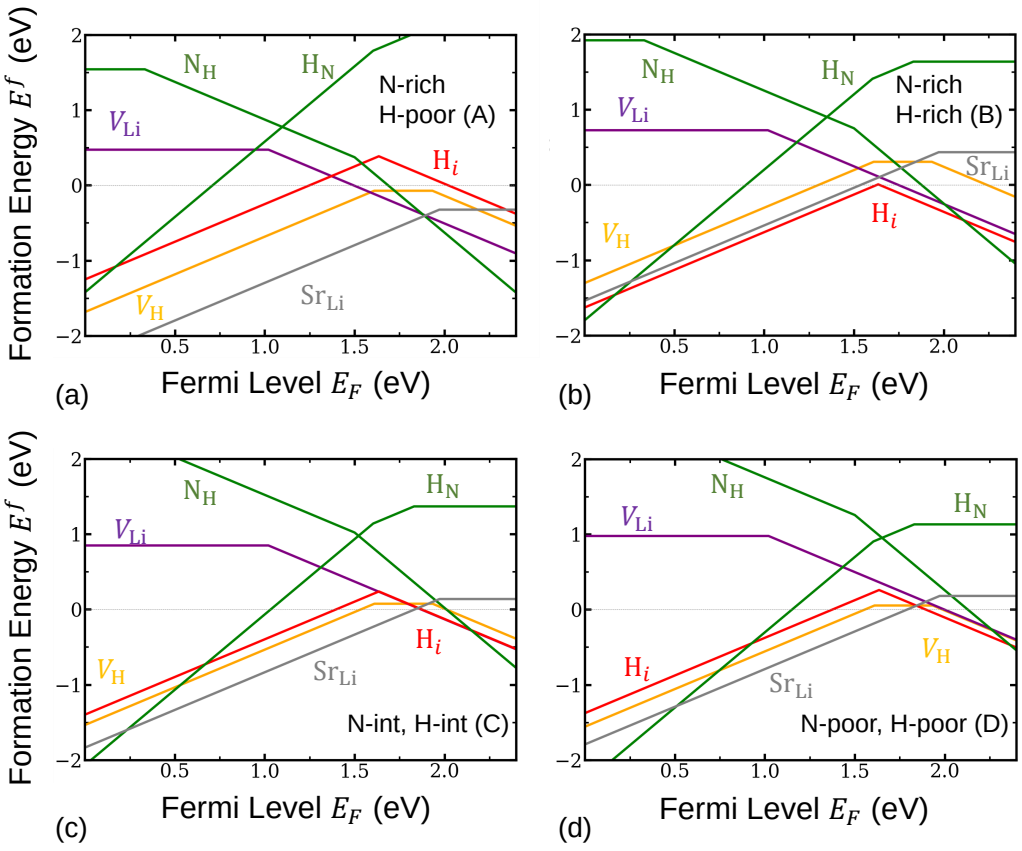

Figure 6.4: Defect formation energies as a function of Fermi level in Sr_2LiH_2N under (a) N-rich/H-poor, (b) N-rich/H-rich, (c) N-intermediate/H-intermediate, and (d) N-poor/H-poor chemical potential conditions, as defined in Fig. 6.3 and Table 6.2. Labels (A), (B), (C), and (D) used here correspond to those used in Fig. 6.3 and Table 6.2.

ditions is the ubiquity of H_i^- as the dominant acceptor species. Under N-rich/H-rich conditions [Fig. 6.4(b)], H_i^+ will compensate H_i^-, implying that SLHN may allow for simultaneous stabilization of protons and hydride ions, which is a highly unusual but scientifically interesting possibility [21]. However, as conditions evolve toward the N-poor/H-poor limit, the cation antisite Sr_{Li}^+ becomes the dominant donor defect. At the N-poor/H-poor limit [Fig. 6.4(d)], these species are accompanied by a large concentration of V_H^0, which, while not influencing the location of E_F, may contribute to the movement of hydrogen (see Section 4.5.3 for a discussion of how V_H^0 may increase hydrogen movement in BaH_2). In general, though, our observation of the favorability of H_i supports the experimental observation of a significant amount of excess hydrogen content in SLHN reported by Liu *et al*. [196]

Oxygen Impurities

Both experimental reports on SLHN reported a high sensitivity to moisture [195, 196]. We are therefore prompted to calculate the formation energy of several possible oxygen impurity configurations: substitutional O_N, O_H, and interstitial O_i. Doing so will allow us to set some limits on how much oxygen in the environment can be tolerated.

In Fig. 6.5, we plot the concentration of oxygen impurities as a function of $\Delta\mu_O$, which is correlated to experimental oxygen partial pressures. We use a typical synthesis temperature of $T = 900$ K to generate the plot [195]. We aim to identify oxygen chemical potential values for which the formation energy of oxygen defects remains positive; based on Eq. 2.16 and the calculated volume listed in Table 6.1, this requirement corresponds to an oxygen concentration just below 10^{22} cm^{-3}, indicated in Fig. 6.5 by a horizontal dashed line. O_H^- and O_N^+ turn out to be the dominant oxygen configurations; O_i^{-2} is much less prevalent, in comparison. Under N-rich/H-rich

conditions [Fig. 6.5(a)], oxygen impurities will cause the material to become unstable for $\Delta\mu_O > -4.75$ eV. We note that increasing concentrations of O_H^- will also cause the Fermi level to shift to lower energies, which suppresses the concentration of H_i^- and limits the hydride conductivity. The situation is worse for N-poor/H-poor conditions [Fig. 6.5(b)], for which the limiting oxygen chemical potential already occurs at $\Delta\mu_O = -5$ eV. Thus, N-rich/H-rich conditions make the essential task of avoiding oxygen contamination more achievable. Degradation upon oxygen exposure is common among many nitrides; fortunately, protective strategies such as encapsulation have shown great promise [197].

6.4.4 Hydride Migration in Sr_2LiH_2N

The favorability of H_i^- implies that it will be the most important defect for conductivity in SLHN. That makes SLHN unique compared to the other hydride conductors we have considered in Chapters 4 and 5, in which V_H^+ is the primary charge carrier. Therefore, we consider its mobility using the NEB method and calculate the activation energy as per Eq. 2.35.

For H_i^-, the formation energy ranges from approximately 0.01 eV under N-rich/H-rich conditions to 0.05 eV under N-poor/H-poor conditions—as a reminder, these are the chemical potential conditions under which SLHN remains stable with respect to native defects [as opposed to N-rich/H-poor conditions, Fig. 6.4(a)]. These low formation energies imply that the migration barrier will be the limiting factor for ionic conduction. A likely pathway for H_i^- diffusion is migration down the a-axis in the empty channels separating chains of Li–N–3H motifs [see Fig. 6.1(d)]; thus, we begin by calculating the energetic barrier to migration for this channel diffusion mechanism,

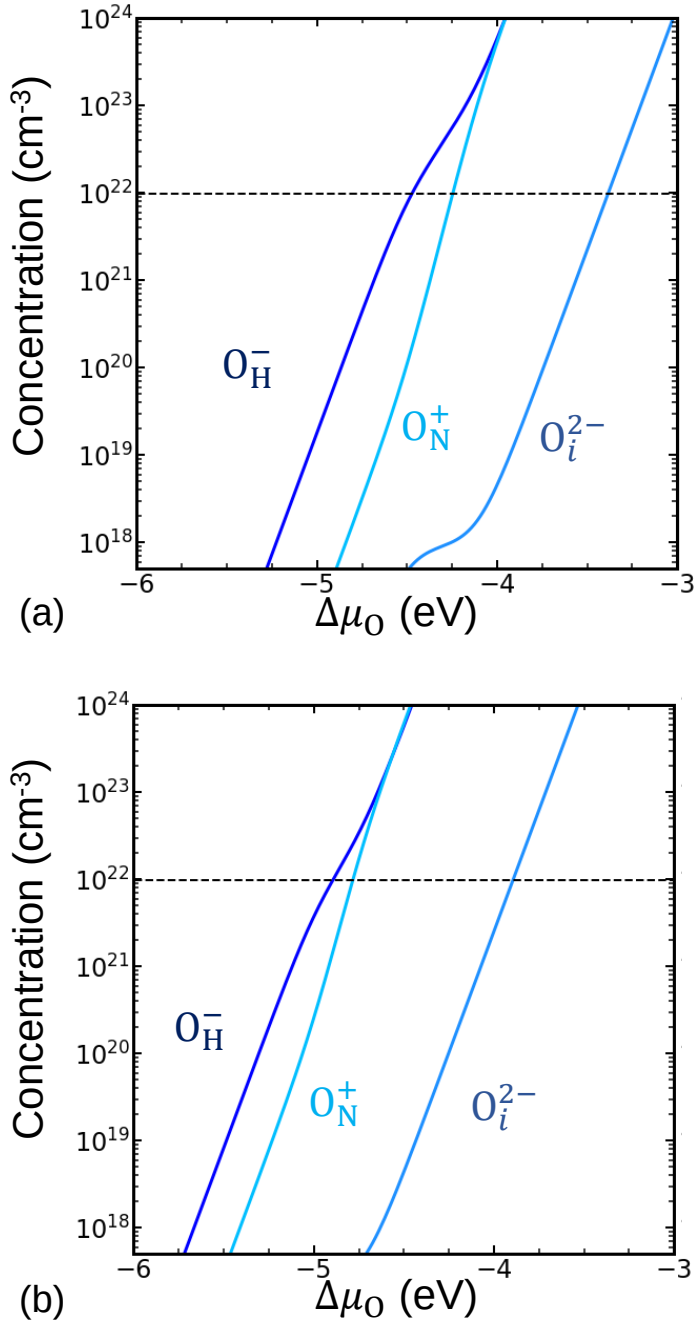

Figure 6.5: Concentrations of oxygen impurities and H_i^- in SLHN at $T = 900$ K as a function of $\Delta\mu_O$ for (a) N-rich/H-rich conditions (condition B in Table 6.2) and (b) N-poor/H-poor conditions (condition D in Table 6.2). The dashed horizontal line indicates defect concentrations at which the material will no longer be stable.

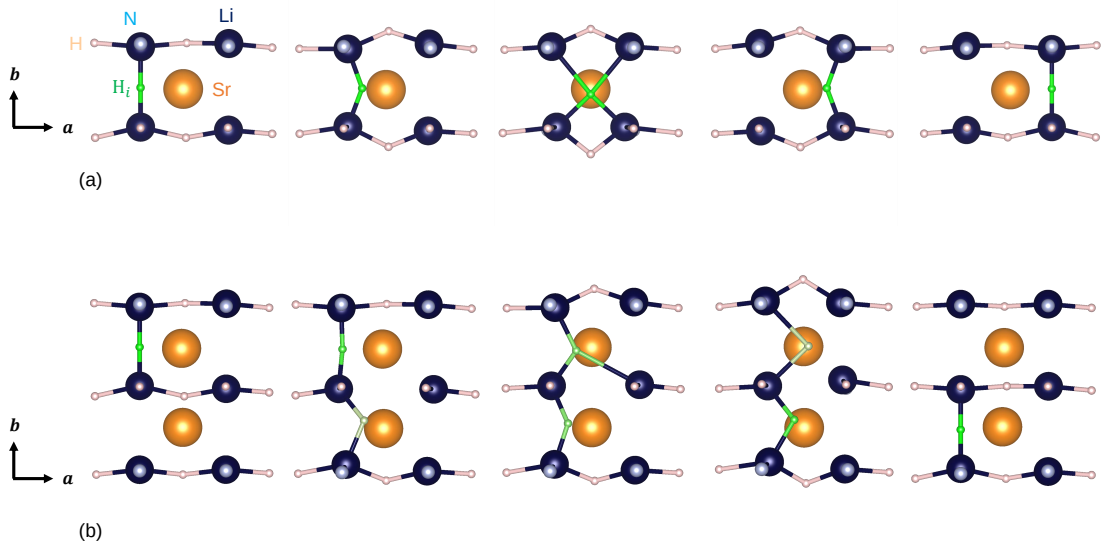

Figure 6.6: Schematic depictions of hydride migration in Sr_2LiH_2N. Mobile hydrogen species are colored green for clarity. (a) Diffusion of H_i^- down an empty channel along the *a*-axis. (b) Diffusion of H_i^- along the *b*-axis.

shown schematically in Fig. 6.6(a). Our calculations reveal a symmetric barrier of 0.40 eV, which translates to an activation energy of 0.41–0.45 eV.

Another possible pathway for H_i^- diffusion is along the *b*-axis. There are no free spaces for H_i^- to move in this direction; however, diffusion may proceed via a "kick-out" process, whereby H_i^- replaces a lattice hydride, which in turn becomes a new H_i^- in the neighboring channel. This process is shown in Fig. 6.6(b), wherein the initial and final states show H_i^- in green, while intermediate images show the evolution between configurations by varying the color. Diffusion along the *b*-axis has a higher migration barrier—0.59 eV—than does diffusion along *a*, indicating that this pathway will be taken less frequently.

In contrast to the *a*- and *b*-directions, there are no obvious migration pathways along the *c*-axis. It is likely that diffusion along the *c*-axis would require the passage of H_i^- around relatively large Sr atoms. We determined that the formation energy of H_i^-

in these regions is high, which means that the migration barrier will also be large. Another option, based on movement of apical H anions, seems similarly unlikely, given that our formation energy calculations imply that there is limited tolerance for disorder on anionic apical sites in SLHN. As a result, diffusion will be primarily anisotropic, and the lower energy pathway along the empty channels parallel to the a-axis should dominate hydride conduction in SLHN. Its activation energy is lower than that measured in LaHO, which has demonstrated the highest measured solid-state hydride conductivity [179].

For comparison, we also consider hydride migration in LLHN. Our NEB calculations show hydride migration to be considerably less favorable in LLHN. H_i^- diffusion along a pathway similar to the one shown in Fig. 6.6(a), has a very high barrier, approximately 1.55 eV. The size of the barrier appears to be connected to Li–Li spacing, which is larger in SLHN than in LLHN; as a result, diffusion of H_i^- is more constricted in LLHN. The large magnitudes of these migration barriers serve as a further indication that LLHN is not worth exploring as a hydride conductor.

6.5 Conclusions

In conclusion, we have calculated defect formation and migration properties in SLHN, a nitride hydride with intriguing prospects as a solid-state hydride electrolyte. We also considered the La-based analogue to SLHN; however, its poor hydride mobility renders it significantly less attractive. For SLHN, we have identified chemical potential conditions under which defect formation energies are positive, implying that careful synthesis can lead to a metastable material. Defects will be quite prevalent in SLHN, particularly H_i^-, which will compensate with H_i^+ under N-rich conditions or Sr_{Li}^+ under more N-poor conditions. The low formation energy of H_i^-, coupled with

its low migration barrier of 0.40 eV along the *a*-axis, leads us to predict an activation energy that can be as low as 0.41–0.45 eV, which is superior to the measured activation energy in the most conductive oxyhydrides. While oxygen incorporation can be damaging for SLHN's stability and conductivity, our results demonstrate that, with careful synthesis and usage, its performance will rival that of the best solid-state hydrogen electrolytes currently known.

Chapter 7

Summary and Future Directions

The work presented in this thesis showed the utility of accurate first-principles defect calculations in describing the properties of several solid-state hydrogen electrolyte materials. We focused primarily on defect formation energies, migration barriers for mobile species, binding energies, and chemical stability, following the procedures outlined in Chapter 2. These results were interpreted in a manner that can be applied to future experimental work on these materials.

We began in Chapter 3 with several proton-conducting oxides, first focusing on the alkaline-earth zirconates ($CaZrO_3$, $SrZrO_3$, and $BaZrO_3$). Because these materials do not intrinsically contain hydrogen, it must be added into them. The commonly proposed method for doing so is to create high concentrations of oxygen vacancies and then to expose the material to water (Eq. 3.1). Doing so fills the vacancies and leaves the remaining two hydrogen atoms to incorporate as interstitial protons [23]. Increasing the concentration of protons therefore requires large quantities of oxygen vacancies, which, due to their positive charge, require the presence of a negatively charged acceptor species to form. We evaluated the traditional trivalent acceptor dopants, Sc^{-}_{Zr} and Y^{-}_{Zr}, for this purpose, while also considering less-studied alkali metal dopants,

such as K_{Sr}^{-} and Rb_{Ba}^{-}. Our results show that the trivalent species are more prone to forming as "wrong"-site acceptors by substituting on the divalent cation site, i.e., Sc_{Sr}^{+}, which conflicts with the goal of promoting oxygen vacancies. Alkali metal acceptors do not exhibit this problem, and furthermore, they have lower binding energies with protons than do trivalent species, implying that their use will lead to higher proton conductivity.

In the course of studying these systems, we also considered various native point defects and extrinsic impurities that may hamper proton conductivity. In $CaZrO_3$, we find cation antisites (Ca_{Zr}^{-2} and Zr_{Ca}^{+2}) to be very low in energy, such that acceptor doping will increase concentrations of Zr_{Ca}^{+2} preferentially to oxygen vacancies. $SrZrO_3$ suffers from a similar problem depending on the chemical potential conditions, while $BaZrO_3$ is resistant to these defects. Carbon is a detrimental impurity in all three materials, incorporating in interstitial (C_i^{+4}) and double-substitutional ($2C_{Zr}^{+4}$) configurations as low-energy donor species, which will also compete with oxygen vacancies.

Our observation of carbon's tendency to incorporate led us to compare the situation in the zirconates with that of the cerates, specifically, $SrCeO_3$ and $BaCeO_3$, which are known to be particularly susceptible to carbon degradation [122]. To understand relative stability in these systems, we calculated the energetics of carbon incorporation in the cerates as well, finding that C_i^{+4} species suppress V_O^{+2} concentrations even more so than in the zirconates. The cerates have particularly low stability with respect to carbonate phases; therefore, we suggest the use of other precursors during synthesis, such as nitrate phases (e.g., $Ba(NO_3)_2$). C_i^{+4} species are also more mobile in the cerates than in the zirconates, implying that they can more readily penetrate into devices during operation as well as synthesis. These findings show why alloying cerates with their respective zirconates has been observed to improve stability.

In Chapter 4, we applied a similar methodology to studying the alkaline-earth hydrides (CaH_2, SrH_2, and BaH_2), which have gained attention due to their high hydride-ion conductivity [28]. Through our study of native point defects, we found hydrogen vacancies—in particular, V_H^+—to form and to migrate very readily, leading us to identify them as the primary ionic charge carriers. As in the zirconates, increasing conductivity requires higher concentrations of these charged species, which can be achieved through the use of acceptor dopants. We identified Na (in CaH_2 and SrH_2) and K (in BaH_2) as the optimal dopants for this purpose, based on their ability to promote V_H^+ formation and based on their low Coulombic binding energies. In BaH_2, which has the lowest formation energy and migration barrier for V_H^+, we estimated an improvement in ionic conductivity on the order of 100-fold upon K-doping, which has powerful implications for using these materials in solid-state fuel cells.

While studying the alkaline-earth hydrides, we became aware of emerging solid-state hydride conductors in the realm of mixed-anionic materials. Such systems, including oxynitrides, oxyfluorides, and oxysulfides, offer improved functionality over many single-anion materials [24]. In our case, we examined oxyhydrides of the form $La_{2-x-y}Sr_{x+y}LiH_{1-x+y}O_{3-y}$, which had demonstrated exceptionally high hydride conductivity in proof-of-concept fuel cells [29]. In particular, we sought to explain the observed increase in conductivity as the ratio of Sr-to-La cations is increased, and to address concerns about the materials' stability.

We focused on La_2LiHO_3 (LLHO) and Sr_2LiH_3O (SLHO) in Chapter 5. Our calculations showed that LLHO has a defined region of chemical stability, while SLHO does not; however, positive defect formation energies imply that it may be possible to synthesize SLHO as a metastable compound. Increasing the degree of disorder, in the form of vacancies and anionic antisite defects, provides a stabilizing effect on the material, while also increasing the concentration of V_H^+, which is again the mobile

charge carrier. We recommend O-rich synthesis conditions slightly off of the H-rich conditions for optimal stability and ionic conductivity.

Studying these oxyhydrides inspired us to look for other mixed-anionic materials, and we discovered the nitride hydrides, in which nitrogen and hydrogen occupy anionic sites. One material, in particular, stood out for its structural similarities to SLHO: Sr_2LiH_2N (SLHN). With two experimental reports of its synthesis as motivation [195, 196], we studied the defect properties and hydride mobility of SLHN; our results are reported in Chapter 6. While SLHN suffers from poor chemical stability, with like the oxyhydrides of Chapter 5, we again find regions in which defect formation energies are positive, implying that the material may be metastable. The prevalent defects include H_i^-, which is the mobile charge carrier. The fact that an interstitial species is the ionic charge carrier for SLHN is relatively uncommon among hydride-ion conductors, most of which see charge transported by vacancies. SLHN possesses empty channels in its crystal structure through which these defects can travel, and we find the activation energy for conduction to be very small, even lower than in some of the best hydride-conducting materials known. Provided that chemically-limiting phases are be suppressed, and that oxygen exposure is prevented, SLHN may set new marks among solid-state hydride ion conductors.

Our studies have followed developments in experimental research to explain observed phenomena and propose new techniques for maximizing ionic conductivity in practice. For hydrogen energy to be adopted on a large scale, materials such as these will need to be integrated into stable, conductive solid-state fuel cells. Proton-conducting oxides have the advantage of experience, having been studied for several decades; however, as our work has demonstrated, there remain plentiful ways to improve their performance. One avenue not yet explored is that of direct hydrogen incorporation, in other words, incorporating H_i^+ *instead* of V_O^{+2}. Our defect formation ener-

gies, which show H_i^+ to have a lower formation energy than V_O^{+2} [see Fig. 3.7] suggest that this should in principle be possible, and it may lead to even higher concentrations of protons than simply filling oxygen vacancies with water molecules. Hydride-ion conductors, on the other hand, are still in their scientific infancy, and a great deal of additional research is needed to optimize their conductivity and chemical stability. Our work has helped to facilitate those efforts by showing what makes hydride conductors more conductive, and how synthesis conditions and carefully-selected dopants can be used to improve their performance. Structural considerations, such as the planar orientation of hydride anions in SLHO, or the linear cavities for migration in SLHN, will also play an important role in materials design.

Without doubt, future research will continue to push the bounds on conductivity and stability, and along the way, first-principles calculations will be an invaluable partner for answering the questions necessary to unlock fully the technological capabilities of solid-state electrolytes. As we continue to march into a future urgently requiring renewable energy solutions, this work has never been more vital.

Appendix A

Quaternary Chemical Potential Stability Diagrams

A.1 Chemical Stability in Quaternary Compounds

Defining stability regions for quaternary compounds is more complicated than for binary or ternary compounds. While one of the four chemical potentials can be rewritten as a function of the others with the thermodynamic stability condition, the other three are free variables. In principle, such a stability diagram can be plotted in three dimensions, as has been done by others [198]. However, we find it more intuitive to plot snapshots of this three-dimensional diagram in two-dimensional chemical potential space, focusing on the regions where chemical stability can be achieved. Each of these two-dimensional snapshots thus assumes a particular chemical potential for one of the elements, which can be treated as a tunable parameter, while the other two chemical potentials vary freely.

We recommend selecting an element with a gas-phase ground state (N, O, H, F, etc.) for the tunable parameter in this methodology. It is easiest to match chemical

potentials of gases to experimentally controlled partial pressures; thus, this choice corresponds best to parameters controlled in a laboratory setting (see Eq. 2.19). If the quaternary compound contains two or more such elements, the remaining one(s) should be plotted explicitly on the two-dimensional snapshots for the same reason. It follows, then, that the element whose chemical potential is rewritten as a function of the remaining three should not have a gas-phase ground state.

In the work presented in Chapters 5 and 6, we discuss results for three quaternary compounds: La_2LiHO_3, Sr_2LiH_3O, and Sr_2LiH_2N. Here, we describe in detail how their stability regions can be derived, or, if the compounds have no stability regions, how we plot their limiting phases in chemical potential space. In doing so, we aim to model a procedure that can be followed in future first-principles studies of quaternary compounds.

As a final note, we recommend an analogous approach for compounds consisting of five (or more) elements. In order to plot two-dimensional snapshots, two (or more) elements will need to be set as parameters—again, choosing gas-phase elements is likely to provide the most meaningful portrayal for experiments.

A.2 Phase stability of La_2LiHO_3

We begin with the oxyhydride La_2LiHO_3. The formation energies of point defects in La_2LiHO_3 depend on the chemical potentials μ, which represent experimental conditions during growth or processing. The La chemical potential, μ_{La}, is referenced to the energy of a single atom in hexagonal-phase La, $E_{\mathrm{tot}}(\mathrm{La})$; we define a quantity $\Delta\mu_{\mathrm{La}}$ with respect to this energy: $\mu_{\mathrm{La}} = E_{\mathrm{tot}}(\mathrm{La}) + \Delta\mu_{\mathrm{La}}$. Similarly, μ_{Li} is referenced to solid (*bcc*) Li and used to define $\Delta\mu_{\mathrm{Li}}$. μ_{H} and μ_{O} are referenced to H_2 and O_2 molecules at $T = 0$ K, respectively, and $\Delta\mu_{\mathrm{H}}$ and $\Delta\mu_{\mathrm{O}}$ are defined with respect to those energies.

The $\Delta\mu$ quantities are variables in our formalism; however, they are subject to bounds. The condition of stability for La_2LiHO_3 requires that:

$$2\Delta\mu_{La} + \Delta\mu_{Li} + \Delta\mu_{H} + 3\Delta\mu_{O} = \Delta H^{f}(La_2LiHO_3). \tag{A.1}$$

In order to prevent precipitation of bulk-phase La or Li, and to prevent loss of H_2 or O_2, the $\Delta\mu$ values are bounded from above:

$$\Delta\mu_{La}, \Delta\mu_{Li}, \Delta\mu_{H}, \Delta\mu_{O} \leq 0. \tag{A.2}$$

Under certain chemical environments, secondary oxide or hydride phases will form. We considered a vast selection of possible limiting phases included in the Materials Project database [199] containing combinations of La, Li, H, and O; however, we only found a select few of them (described below) to be relevant. To prevent the formation of hydride phases,

$$\Delta\mu_{La} + 3\Delta\mu_{H} \leq \Delta H^{f}(LaH_3), \tag{A.3}$$

$$\Delta\mu_{Li} + \Delta\mu_{H} \leq \Delta H^{f}(LiH). \tag{A.4}$$

To prevent the formation of oxide phases,

$$2\Delta\mu_{La} + 3\Delta\mu_{O} \leq \Delta H^{f}(La_2O_3), \tag{A.5}$$

$$2\Delta\mu_{Li} + \Delta\mu_{O} \leq \Delta H^{f}(Li_2O). \tag{A.6}$$

To prevent the formation of hydroxide phases,

$$\Delta\mu_{\mathrm{La}} + 3\Delta\mu_{\mathrm{O}} + 3\Delta\mu_{\mathrm{H}} \leq \Delta H^f(\mathrm{La(OH)_3}), \tag{A.7}$$

$$\Delta\mu_{\mathrm{Li}} + \Delta\mu_{\mathrm{O}} + \Delta\mu_{\mathrm{H}} \leq \Delta H^f(\mathrm{LiOH}). \tag{A.8}$$

Finally, to prevent the formation of water,

$$2\Delta\mu_{\mathrm{H}} + \Delta\mu_{\mathrm{O}} \leq \Delta H^f(\mathrm{H_2O}). \tag{A.9}$$

The enthalpies of formation we use are calculated within our first-principles approach. We list them in Table A.1 alongside values from the literature where available.

To determine a set of chemical potentials for which La_2LiHO_3 is stable, a phase diagram can be constructed. Given that La_2LiHO_3 is a quaternary compound, the phase space is complicated. To simplify the picture, we choose a value for $\Delta\mu_{\mathrm{H}}$; then, using the equilibrium condition in Eq. A.1, we can create plots in terms of two of the remaining three chemical potentials. We generate phase diagrams in the $\Delta\mu_{\mathrm{O}} - \Delta\mu_{\mathrm{La}}$ plane. The inequalities describing the formation of solid-phase La (Eq. A.2), O_2 (Eq. A.2), (LaH_3 Eq. A.3), La_2O_3 (Eq. A.5), $La(OH)_3$ (Eq. A.7), and H_2O (Eq. A.9) can be plotted directly on this plane. The formation boundary of solid-phase Li ($\Delta\mu_{\mathrm{Li}} \leq 0$) can be plotted by substituting Eq. A.1 into Eq. A.2 for Li:

$$\Delta\mu_{\mathrm{La}} \geq \left[\Delta H^f(\mathrm{La_2LiHO_3}) - \Delta\mu_{\mathrm{H}} - 3\Delta\mu_{\mathrm{O}}\right]/2. \tag{A.10}$$

The condition preventing formation of LiH is depicted by substituting Eq. A.1 into Eq. A.4:

$$\Delta\mu_{\mathrm{La}} \geq \left[\Delta H^f(\mathrm{La_2LiHO_3}) - \Delta H^f(\mathrm{LiH}) - 3\Delta\mu_{\mathrm{O}}\right]/2. \tag{A.11}$$

Table A.1: Calculated and reported enthalpies of formation (in eV per formula unit) for compounds pertinent to this study.

Compound	ΔH^f (eV) (calc)	ΔH^f (eV) (exp)
La_2LiHO_3	–18.96	–
Sr_2LiH_3O	–2.19	–
Sr_2LiH_2N	–3.20	–
LaH_3	–2.68	–3.47 [200]
SrH_2	–1.80	–1.87 [142]
LiH	–0.90	–0.94 [142]
La_2O_3	–18.00	–18.59 [142]
SrO	–5.61	–6.14 [142]
Li_2O	–5.76	–6.20 [142]
H_2O	–2.65	–2.96 [142]
Li_3N	–2.69	–1.71 [201]
Sr_2N	–2.59	–
$La(OH)_3$	–14.40	–14.69 [202]
$Sr(OH)_2$	–9.57	–9.94 [142]
Li(OH)	–4.88	–5.05 [142]
$LiSrH_3$	–1.10	–
Sr_2HN	–2.55	–

The condition preventing formation of Li_2O is shown by substituting Eq. A.1 into Eq. A.6:

$$\Delta\mu_{La} \geq \left[2\Delta H^f(La_2LiHO_3) - \Delta H^f(Li_2O) - 2\Delta\mu_H - 5\Delta\mu_O\right]/4. \quad (A.12)$$

Finally, the condition preventing formation of LiOH is shown by substituting Eq. A.1 into Eq. A.8:

$$\Delta\mu_{La} \geq \left[\Delta H^f(La_2LiHO_3) - \Delta H^f(LiOH) - 2\Delta\mu_O\right]/2. \quad (A.13)$$

A.2.1 H-rich limit ($\mu_H = 0$ eV)

We initially set $\Delta\mu_H = 0$ in Fig. A.1(a), corresponding to the H-rich limit. The effects of varying $\Delta\mu_H$ will be discussed subsequently.

The gray shaded area in Fig. A.1(a) indicates the region of chemical potentials for which La_2LiH_3O is stable. From this plot, the oxygen chemical potential can vary over the range -4.23 eV $\leq \Delta\mu_O \leq -3.68$ eV; for the purposes of presenting our results, we use the oxygen-rich limit of this range, $\Delta\mu_O = -3.68$ eV. When $\Delta\mu_O = -3.68$ eV and $\Delta\mu_H = 0$ eV, the remaining chemical potentials are uniquely determined: $\Delta\mu_{La} = -3.36$ eV and $\Delta\mu_{Li} = -1.20$ eV. We use these chemical potentials to calculate the formation energies shown in Fig. 5.2(a).

A.2.2 H-poor limit

It is also possible to identify the H-poor limit, i.e., the lowest possible value of $\Delta\mu_H$ for which La_2LiHO_3 will be stable. In Fig. A.1, we plot La_2LiHO_3 phase diagrams in

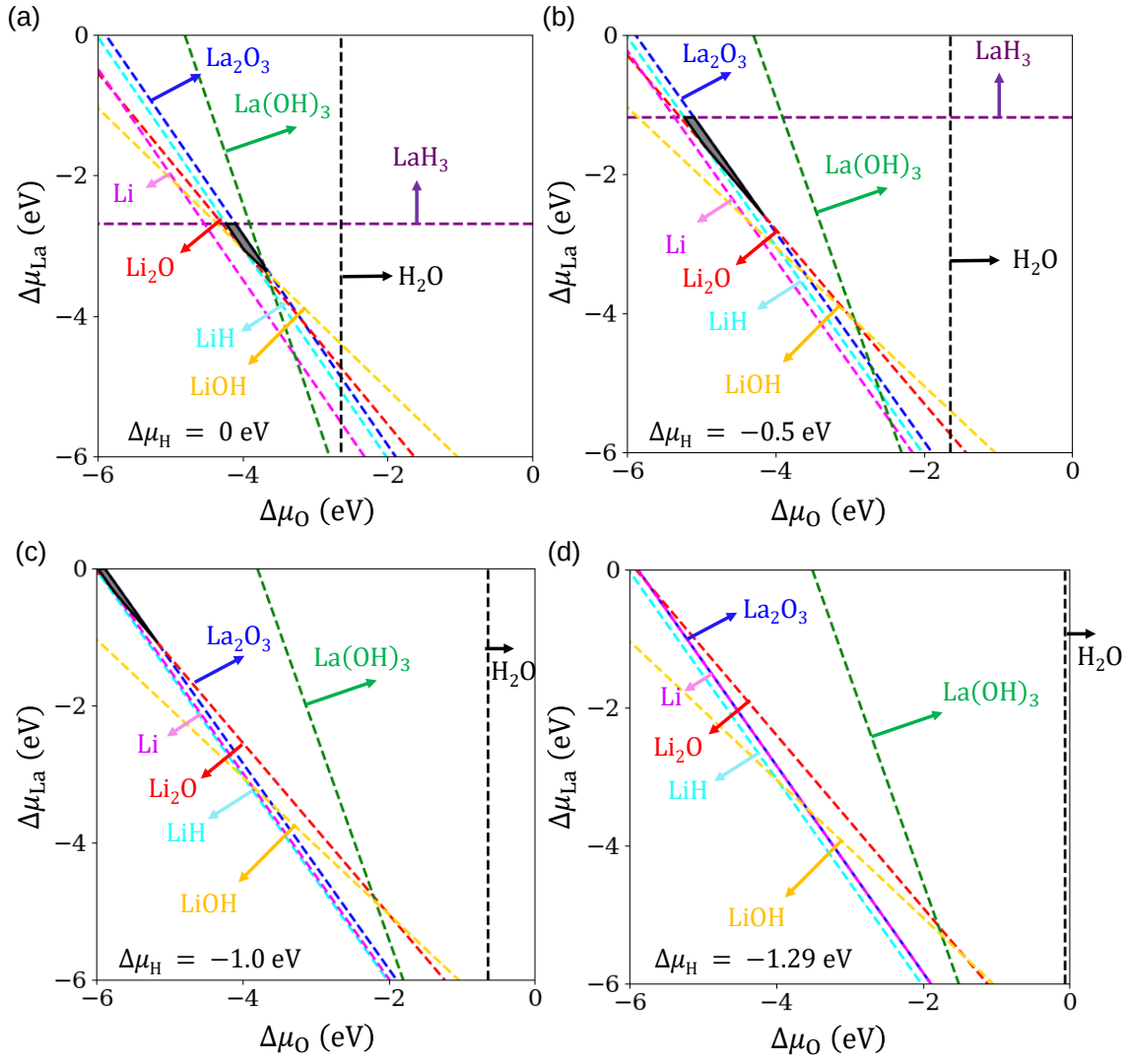

Figure A.1: Phase diagrams for La_2LiHO_3 plotted in the $\Delta\mu_O - \Delta\mu_{La}$ plane, with $\Delta\mu_H$ set to (a) 0 eV, (b) −0.5 eV, (c) −1.0 (eV), and (d) −1.29 eV. The region of chemical stability is shaded gray.

the $\Delta\mu_O - \Delta\mu_{La}$ plane for different values of $\Delta\mu_H$. We specifically plot phase diagrams for $\Delta\mu_H = 0$ eV, -0.5 eV, -1.0 eV, and -1.29 eV.

As $\Delta\mu_H$ is decreased, the phase boundary for La_2O_3 remains fixed (Eq. A.5); however the phase boundaries for Li (Eq. A.10), Li_2O (Eq. A.12), and LaH_3 (Eq. A.3) are shifted upward, such that the La_2LiHO_3 stability region is pushed to higher values of $\Delta\mu_{La}$ and lower values of $\Delta\mu_O$. When $\Delta\mu_H = -1.29$ eV, the stability region disappears entirely—we define that point to be the "H-poor" limit for La_2LiHO_3.

At the H-poor limit, the phase boundaries for Li and La_2O_3 coincide. Along this line, La_2LiHO_3 is stable until these overlapping lines intersect with the phase boundary line for Li_2O. Along this short line segment in the upper-left corner of Fig. A.1(d), the lanthanum chemical potential varies over the range -0.20 eV $\leq \Delta\mu_{La} \leq 0$ eV, and the oxygen chemical potential varies over the narrow range -5.89 eV $\leq \Delta\mu_O \leq -5.76$ eV. We choose the midpoints in these ranges, $\Delta\mu_{La} = -0.10$ eV and $\Delta\mu_O = -5.83$, for plotting H-poor conditions. Given $\Delta\mu_H = -1.29$ eV, Eq. A.1 indicates that $\Delta\mu_{Li} = 0$ eV. These values allow us to plot formation energies under H-poor conditions in Fig. 5.2(b).

A.3 Phase stability of Sr_2LiH_3O

We define chemical potentials for Sr_2LiH_3O in a similar fashion. The Sr chemical potential, μ_{Sr}, is referenced to the energy of a single atom in (*fcc*) Sr, $E_{tot}(Sr)$; we define a quantity $\Delta\mu_{Sr}$ with respect to this energy: $\mu_{Sr} = E_{tot}(Sr) + \Delta\mu_{Sr}$. $(\Delta)\mu_{Li}$, $(\Delta)\mu_H$, and $(\Delta)\mu_O$ are all defined as before.

The condition of stability for Sr_2LiH_3O requires that

$$2\Delta\mu_{Sr} + \Delta\mu_{Li} + 3\Delta\mu_H + \Delta\mu_O = \Delta H^f(Sr_2LiH_3O). \tag{A.14}$$

In order to prevent precipitation of bulk-phase Sr or Li, and to prevent loss of H_2 or O_2, the $\Delta\mu$ values are bounded from above,

$$\Delta\mu_{\mathrm{Sr}}, \Delta\mu_{\mathrm{Li}}, \Delta\mu_{\mathrm{H}}, \Delta\mu_{\mathrm{O}} \leq 0. \tag{A.15}$$

Again, we find only a handful of compounds to be relevant for limiting the chemical stability. To prevent formation of strontium hydride,

$$\Delta\mu_{\mathrm{Sr}} + 2\Delta\mu_{\mathrm{H}} \leq \Delta H^f(\mathrm{SrH_2}). \tag{A.16}$$

To prevent formation of strontium oxide,

$$\Delta\mu_{\mathrm{Sr}} + \Delta\mu_{\mathrm{O}} \leq \Delta H^f(\mathrm{SrO}). \tag{A.17}$$

To prevent the formation of strontium hydroxide,

$$\Delta\mu_{\mathrm{Sr}} + 2\Delta\mu_{\mathrm{O}} + 2\Delta\mu_{\mathrm{H}} \leq \Delta H^f(\mathrm{Sr(OH)_2}). \tag{A.18}$$

Again, the formation of water (Eq. A.9) and the various Li-compounds—LiH (Eq. A.4), Li_2O (Eq. A.6), and LiOH (Eq. A.8)—must also be avoided. The enthalpies of formation we calculated are summarized in Table A.1.

We follow an analogous procedure as before to generate a phase diagram, this time in the $\Delta\mu_{\mathrm{O}} - \Delta\mu_{\mathrm{Sr}}$ plane. Again, to present our results for this quaternary system, we choose a value of $\Delta\mu_{\mathrm{H}}$ and use Eq. A.14 to plot limiting phases in terms of $\Delta\mu_{\mathrm{O}}$ and $\Delta\mu_{\mathrm{Sr}}$. The inequalities describing the formation of solid-phase Sr (Eq. A.15), O_2 (Eq. A.15), SrH_2 (Eq. A.16), SrO (Eq. A.17), SrOH (Eq. A.18), and H_2O (Eq. A.9) can be plotted directly on this plane. The condition to prevent formation of solid-phase Li

can be evaluated by substituting Eq. A.14 into Eq. A.15:

$$\Delta\mu_{\mathrm{Sr}} \geq \left[\Delta H^f(\mathrm{Sr_2LiH_3O}) - 3\Delta\mu_{\mathrm{H}} - \Delta\mu_{\mathrm{O}}\right]/2. \tag{A.19}$$

The condition to prevent formation of LiH can be evaluated by substituting Eq. A.14 into Eq. A.4:

$$\Delta\mu_{\mathrm{Sr}} \geq \left[\Delta H^f(\mathrm{Sr_2LiH_3O}) - \Delta H^f(\mathrm{LiH}) - 2\Delta\mu_{\mathrm{H}} - \Delta\mu_{\mathrm{O}}\right]/2. \tag{A.20}$$

The condition to prevent formation of Li_2O is obtained by substituting Eq. A.14 into Eq. A.6:

$$\Delta\mu_{\mathrm{Sr}} \geq \left[2\Delta H^f(\mathrm{Sr_2LiH_3O}) - \Delta H^f(\mathrm{Li_2O}) - 6\Delta\mu_{\mathrm{H}} - \Delta\mu_{\mathrm{O}}\right]/4. \tag{A.21}$$

Finally, the condition to prevent formation of LiOH is obtained by substituting Eq. A.14 into Eq. A.8 (specifically, $\Delta\mu_{\mathrm{Li}} \leq 0$):

$$\Delta\mu_{\mathrm{Sr}} \geq \left[\Delta H^f(\mathrm{Sr_2LiH_3O}) - \Delta H^f(\mathrm{LiOH}) - 2\Delta\mu_{\mathrm{H}}\right]/2. \tag{A.22}$$

Using these conditions to establish a phase diagram in the $\Delta\mu_{\mathrm{O}} - \Delta\mu_{\mathrm{Sr}}$ plane, with $\Delta\mu_{\mathrm{H}} = 0$, yields Fig. A.2. Unlike La_2LiHO_3, there is no region of stability; for every set of chemical potentials, one or more of the limiting phases will form preferentially. Changing $\Delta\mu_{\mathrm{H}}$ will not produce a stability region. Note that the lines corresponding to formation of Li_2O and LiOH require positive values for both $\Delta\mu_{\mathrm{O}}$ and $\Delta\mu_{\mathrm{Sr}}$ and thus are not shown.

In Chapter 5, we present our results on defect formation for a variety of choices for $\Delta\mu_{\mathrm{H}}$ and $\Delta\mu_{\mathrm{O}}$. Specifically, we choose choose chemical potentials lying halfway

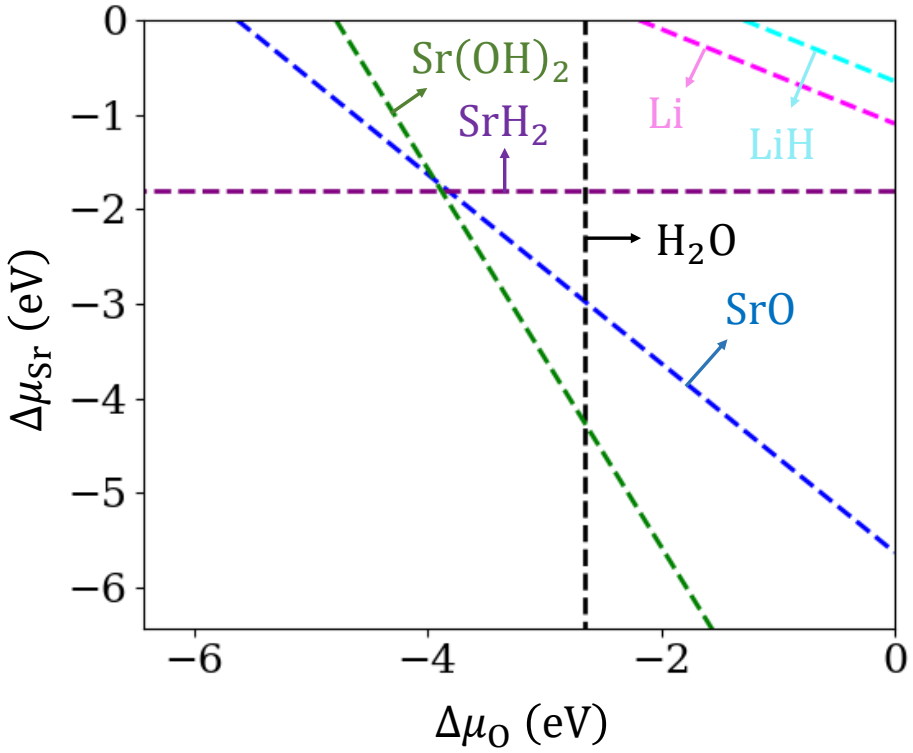

Figure A.2: Phase diagram for Sr_2LiH_3O plotted in the $\Delta\mu_O - \Delta\mu_{Sr}$ plane, with $\Delta\mu_H = 0$.

between the Sr-rich ($\Delta\mu_{\mathrm{Sr}} = 0$ eV) and Li-rich ($\Delta\mu_{\mathrm{Li}} = 0$ eV) endpoints. At the Sr-rich and Li-rich conditions, for a given choice of $\Delta\mu_{\mathrm{H}}$ and $\Delta\mu_{\mathrm{O}}$, we use Eq. A.14 to determine the remaining chemical potential. These specific choices allow us to study the changes in defect chemistry under various permutations of H-rich, H-poor, O-rich, and O-poor growth conditions.

A.4 Phase stability of Sr_2LiH_2N

In Chapter 6, we explore the properties of the prospective hydride-ion conductor Sr_2LiH_2N. In similar fashion as for the oxyhydrides, we can plot its phase stability in chemical potential space. The chemical potentials $(\Delta)\mu_{\mathrm{Sr}}$, $(\Delta)\mu_{\mathrm{Li}}$, and $(\Delta)\mu_{\mathrm{H}}$ are defined as before; now, in place of μ_{O}, we use μ_{N}, which is defined relative to the N_2 molecule at 0 K:

$$\mu_{\mathrm{N}} = \frac{1}{2}E_{\mathrm{tot}}(\mathrm{N_2}) + \Delta\mu_{\mathrm{N}}. \tag{A.23}$$

All pertinent enthalpies of formation are again tabulated in Table A.1.

The condition of stability for Sr_2LiH_2N requires that

$$2\Delta\mu_{\mathrm{Sr}} + \Delta\mu_{\mathrm{Li}} + 2\Delta\mu_{\mathrm{H}} + \Delta\mu_{\mathrm{N}} = \Delta H^f(\mathrm{Sr_2LiH_2N}). \tag{A.24}$$

In order to prevent precipitation of bulk-phase Sr or Li, and to prevent loss of H_2 or N_2, the $\Delta\mu$ values are bounded from above,

$$\Delta\mu_{\mathrm{Sr}}, \Delta\mu_{\mathrm{Li}}, \Delta\mu_{\mathrm{H}}, \Delta\mu_{\mathrm{N}} \leq 0. \tag{A.25}$$

After screening out a large number of possible limiting phases under lower levels of theory, we focus here on a select few compounds that limit the chemical stability of

Sr_2LiH_2N. To prevent formation of distrontium nitride,

$$2\Delta\mu_{Sr} + \Delta\mu_N \leq \Delta H^f(Sr_2N). \tag{A.26}$$

Note that other stoichiometries of Sr and N (e.g., SrN, Sr_4N_3) have similar energetics in the target phase space. To prevent the formation of lithium nitride,

$$3\Delta\mu_{Li} + \Delta\mu_N \leq \Delta H^f(Li_3N). \tag{A.27}$$

To prevent the formation of lithium strontium hydride,

$$\Delta\mu_{Li} + \Delta\mu_{Sr} + 3\Delta\mu_H \leq \Delta H^f(LiSrH_3). \tag{A.28}$$

To prevent the formation of strontium nitride hydride,

$$2\Delta\mu_{Sr} + \Delta\mu_H + \Delta\mu_N \leq \Delta H^f(Sr_2HN). \tag{A.29}$$

Again, the formation of SrH_2 (Eq. A.16) and LiH (Eq. A.4) must be avoided. We did not find any stoichiometries of N and H (i.e., NH_3) that interfere with SLHN; however, such compounds were considered initially.

We now generate a phase diagram in the $\Delta\mu_H - \Delta\mu_{Sr}$ plane, which requires that we choose values for $\Delta\mu_N$ and use Eq. A.24 to plot limiting phases in terms of $\Delta\mu_H$ and $\Delta\mu_{Sr}$. The inequalities describing the formation of solid-phase Sr (Eq. A.25), H_2 (Eq. A.25), SrH_2 (Eq. A.16), Sr_2N (Eq. A.26), and Sr_2HN (Eq. A.29) can be plotted directly on this plane. The condition to prevent formation of solid-phase Li can be

evaluated by substituting Eq. A.24 into Eq. A.15:

$$\Delta\mu_{\mathrm{Sr}} \geq \left[\Delta H^f(\mathrm{Sr_2LiH_2N}) - 2\Delta\mu_{\mathrm{H}} - \Delta\mu_{\mathrm{N}}\right]/2. \tag{A.30}$$

The condition to prevent formation of LiH can be evaluated by substituting Eq. A.24 into Eq. A.4:

$$\Delta\mu_{\mathrm{Sr}} \geq \left[\Delta H^f(\mathrm{Sr_2LiH_2N}) - \Delta H^f(\mathrm{LiH}) - \Delta\mu_{\mathrm{H}} - \Delta\mu_{\mathrm{N}}\right]/2. \tag{A.31}$$

The condition to prevent formation of Li_3N is obtained by substituting Eq. A.24 into Eq. A.27:

$$\Delta\mu_{\mathrm{Sr}} \geq \left[3\Delta H^f(\mathrm{Sr_2LiH_2N}) - \Delta H^f(\mathrm{Li_3N}) - 6\Delta\mu_{\mathrm{H}} - 2\Delta\mu_{\mathrm{N}}\right]/6. \tag{A.32}$$

Finally, the condition to prevent formation of $LiSrH_3$ is obtained by substituting Eq. A.24 into Eq. A.28:

$$\Delta\mu_{\mathrm{Sr}} \geq \left[\Delta H^f(\mathrm{Sr_2LiH_3O}) - \Delta H^f(\mathrm{LiSrH_3}) + \Delta\mu_{\mathrm{H}} - \Delta\mu_{\mathrm{N}}\right]/2. \tag{A.33}$$

The results of this procedure are discussed in detail in Chapter 6, Section 6.4.2. Figure 6.3 shows the stability diagram for SLHN. As with SLHO, there is no region of stability, so we focus on regions of metastability, in which defect formation energies are positive.

Bibliography

[1] S. Arrhenius. "On the influence of carbonic acid in the air upon the temperature of the ground". In: *Phil. Mag. J. Sci.* 41.251 (1896), pp. 237–276. DOI: 10.1080/14786449608620846.

[2] J. Hansen et al. "Global temperature change". In: *Proc. Nat. Acad. Sci.* 103.39 (2006), pp. 14288–14293. DOI: 10.1073/pnas.0606291103.

[3] D. Archer and S. Rahmstorf. *The climate crisis: An introductory guide to climate change*. Cambridge University Press, 2010. DOI: 10.1017/CBO9780511817144.

[4] V. Masson-Delmotte et al. "Global warming of 1.5°C. An IPCC Special Report on the impacts of global warming of 1.5°C above pre-industrial levels and related global greenhouse gas emission pathways, in the context of strengthening the global response to the threat of climate change, sustainable development, and efforts to eradicate poverty". In: *In press* (2019). URL: https://www.ipcc.ch/site/assets/uploads/sites/2/2019/06/SR15_Full_Report_High_Res.pdf.

[5] N. Panwar, S. Kaushik, and S. Kothari. "Role of renewable energy sources in environmental protection: A review". In: *Renew. Sust. Energ. Rev.* 15.3 (2011), pp. 1513–1524. DOI: 10.1016/j.rser.2010.11.037.

[6] R. Pierrehumbert. “There is no Plan B for dealing with the climate crisis”. In: *Bull. Atomic Scientists* 75.5 (2019), pp. 215–221. DOI: 10.1080/00963402.2019.1654255.

[7] I. E. Agency. *The Future of Hydrogen: Seizing today's opportunities*. Paris, FR: International Energy Agency, 2019. URL: https://www.iea.org/reports/the-future-of-hydrogen.

[8] A. Pareek et al. “Insights into renewable hydrogen energy: Recent advances and prospects”. In: *Mater. Sci. Ener. Technol.* 3 (2020), pp. 319–327. DOI: 10.1016/j.mset.2019.12.002.

[9] L. Schlapbach and A. Züttel. “Hydrogen-storage materials for mobile applications”. In: *Nature* 414.6861 (2001), pp. 353–358. DOI: 10.1142/9789814317665_0038.

[10] B. C. Steele and A. Heinzel. “Materials for fuel-cell technologies”. In: *Nature* 414.6861 (2001), pp. 345–352. DOI: 10.1142/9789814317665_0031.

[11] N. R. Council. *Transitions to Alternative Transportation Technologies: A Focus on Hydrogen*. Washington, DC: The National Academies Press, 2008. DOI: 10.17226/12222. URL: https://www.nap.edu/catalog/12222/transitions-to-alternative-transportation-technologies-a-focus-on-hydrogen.

[12] G. W. Crabtree and M. S. Dresselhaus. “The Hydrogen Fuel Alternative”. In: *MRS Bull.* 33.4 (2008), pp. 421–428. ISSN: 0883-7694, 1938-1425. DOI: 10.1557/mrs2008.84.

[13] F. M. Ernsberger. “The nonconformist ion”. In: *J. Am. Chem. Soc.* 66.11 (1983), pp. 747–750. DOI: 10.1111/j.1151-2916.1983.tb10555.x/full.

[14] Y. Wang et al. “A review of polymer electrolyte membrane fuel cells: technology, applications, and needs on fundamental research”. In: *Appl. Ener.* 88.4 (2011), pp. 981–1007. DOI: 10.1016/j.apenergy.2010.09.030.

[15] M Rikukawa and K Sanui. “Proton-conducting polymer electrolyte membranes based on hydrocarbon polymers”. In: *Progress Polymer Sci.* 25.10 (2000), pp. 1463–1502. DOI: 10.1016/S0079-6700(00)00032-0.

[16] L. Dubau et al. “A review of PEM fuel cell durability: materials degradation, local heterogeneities of aging and possible mitigation strategies”. In: *Wiley Interdiscip. Rev. Energy Environ.* 3.6 (2014), pp. 540–560. DOI: 10.1002/wene.113.

[17] P. Jena. “Materials for hydrogen storage: past, present, and future”. In: *J. Phys. Chem. Lett.* 2.3 (2011), pp. 206–211. DOI: 10.1021/jz1015372.

[18] K.-D. Kreuer. “Fast proton transport in solids”. In: *J. Mol. Struct.* 177 (1988), pp. 265–276. DOI: 10.1016/0022-2860(88)80093-0.

[19] C. J. D. T. von Grotthuß. “Sur la décomposition de l’eau et des corps qu’elle tient en dissolution à l’aide de l’électricité galvanique”. In: *Ann. Chim.* 58 (1804), pp. 54–73.

[20] T. Norby. “Solid-state protonic conductors: Principles, properties, progress and prospects”. In: *Solid State Ionics* 125.1 (1999), pp. 1–11. DOI: 10.1016/S0167-2738(99)00152-6.

[21] T. Norby et al. “Hydrogen in oxides”. In: *Dalton Trans.* 19 (2004), pp. 3012–3018. DOI: 10.1039/B403011G.

[22] W. Münch et al. “A quantum molecular dynamics study of proton conduction phenomena in $BaCeO_3$”. In: *Solid State Ionics* 86 (1996), pp. 647–652. DOI: 10.1016/0167-2738(96)00229-9.

[23] K.-D. Kreuer. "Proton-conducting oxides". In: *Annu. Rev. Mater. Res.* 33.1 (2003), pp. 333–359. DOI: 10.1146/annurev.matsci.33.022802.091825.

[24] H. Kageyama et al. "Expanding frontiers in materials chemistry and physics with multiple anions". In: *Nat. Commun.* 9.1 (2018), p. 772. DOI: 10.1038/s41467-018-02838-4.

[25] M. Meot-Ner and F. Field. "Temperature dependences of some fast ion-polar molecule proton transfer and of slow hydride (1-) ion transfer reactions". In: *J. Am. Chem. Soc.* 97.8 (1975), pp. 2014–2017. DOI: 10.1021/ja00841a003.

[26] X. Liu, T. S. Bjørheim, and R. Haugsrud. "Formation and migration of hydride ions in $BaTiO_{3-x}H_x$ oxyhydride". In: *J. Mater. Chem. A* 5.3 (2017), pp. 1050–1056. DOI: 10.1039/C6TA06611A.

[27] C. A. Bridges et al. "Observation of Hydride Mobility in the Transition-Metal Oxide Hydride $LaSrCoO_3H_{0.7}$". In: *Adv. Mater.* 18.24 (2006), pp. 3304–3308. DOI: 10.1002/adma.200601266.

[28] M. C. Verbraeken et al. "High H^- ionic conductivity in barium hydride". In: *Nat. Mater.* 14.1 (Dec. 8, 2014), pp. 95–100. ISSN: 1476-1122, 1476-4660. DOI: 10.1038/nmat4136.

[29] G. Kobayashi et al. "Pure H^- conduction in oxyhydrides". In: *Science* 351.6279 (2016), pp. 1314–1317. DOI: 10.1126/science.aac9185.

[30] S. Hao and D. S. Sholl. "Role of Schottky Defects in Hydrogen and Metal Diffusion in NaH, MgH_2, and $NaMgH_3$". In: *J. Chem. Phys. Lett.* 1.19 (Oct. 7, 2010), pp. 2968–2973. ISSN: 1948-7185, 1948-7185. DOI: 10.1021/jz101118f.

[31] K. Hoang and C. G. Van de Walle. "Hydrogen-related defects and the role of metal additives in the kinetics of complex hydrides: A first-principles study". In: *Phys. Rev. B* 80.21 (Dec. 11, 2009), p. 214109. ISSN: 1098-0121, 1550-235X. DOI: 10.1103/PhysRevB.80.214109.

[32] M. S. Park, A. Janotti, and C. G. Van de Walle. "Formation and migration of charged native point defects in MgH_2: First-principles calculations". In: *Phys. Rev. B* 80.6 (Aug. 4, 2009), p. 064102. ISSN: 1098-0121, 1550-235X. DOI: 10.1103/PhysRevB.80.064102.

[33] G. B. Wilson-Short et al. "First-principles study of the formation and migration of native defects in $NaAlH_4$". In: *Phys. Rev. B* 80.22 (Dec. 4, 2009), p. 224102. ISSN: 1098-0121, 1550-235X. DOI: 10.1103/PhysRevB.80.224102.

[34] M. B. Ley et al. "Complex hydrides for hydrogen storage - new perspectives". In: *Mater. Today* 17.3 (2014), pp. 122–128. DOI: 10.1016/j.mattod.2014.02.013.

[35] A. Bain and W. D. Van Vorst. "The Hindenburg tragedy revisited: the fatal flaw found". In: *Intl. J. Hydrog. Ener.* 24.5 (1999), pp. 399–403. DOI: 10.1016/S0360-3199(98)00176-1.

[36] D. Kramer. "Hydrogen-powered vehicles: A chicken and egg problem". In: *Phys. Today* 70.9 (2017), pp. 31–32. URL: 10.1063/PT.3.3690.

[37] D. Hydrogen and F. C. Program. *FY 2019 Progress Report for the DOE Hydrogen and Fuell Cells Program*. Washington, DC: U.S. Department of Energy, 2020. URL: https://www.nrel.gov/docs/fy20osti/76055.pdf.

[38] H. Council. *Hydrogen scaling up, a sustainable pathway for the global energy transition*. Hydrogen Council, 2017. URL: https://hydrogencouncil.com/wp-content/uploads/2017/11/Hydrogen-scaling-up-Hydrogen-Council.pdf.

[39] E. L. Miller et al. “US Department of Energy hydrogen and fuel cell technologies perspectives”. In: *MRS Bull.* 45.1 (2020), pp. 57–64. DOI: 10.1557/mrs.2019.312.

[40] B. D. James et al. “Mass production cost estimate of direct H_2 PEM fuel cell systems for transportation applications: 2017 update”. In: (2017). URL: https://www.energy.gov/sites/prod/files/2017/06/f34/fcto_sa_2016_pemfc_transportation_cost_analysis.pdf.

[41] J. A. Turner. “Sustainable hydrogen production”. In: *Science* 305.5686 (2004), pp. 972–974. DOI: 10.1126/science.1103197.

[42] J. D. Holladay et al. “An overview of hydrogen production technologies”. In: *Catalysis Today* 139.4 (2009), pp. 244–260. DOI: 10.1016/j.cattod.2008.08.039.

[43] P. Nikolaidis and A. Poullikkas. “A comparative overview of hydrogen production processes”. In: *Renew. Sustain. Ener. Rev.* 67 (2017), pp. 597–611. DOI: 10.1016/j.rser.2016.09.044.

[44] J. Tournet et al. “III–V Semiconductor Materials for Solar Hydrogen Production: Status and Prospects”. In: *ACS Ener. Lett.* 5.2 (2020), pp. 611–622. DOI: 10.1021/acsenergylett.9b02582.

[45] C. J. Bartel et al. “Physical descriptor for the Gibbs energy of inorganic crystalline solids and temperature-dependent materials chemistry”. In: *Nat. Commun.* 9.1 (2018), pp. 1–10. DOI: 10.1038/s41467-018-06682-4.

[46] E. Crespi et al. “Modelling and optimization of a flexible hydrogen-fueled pressurized PEMFC power plant for grid balancing purposes”. In: *Intl. J. Hydrog. Ener.* 46.24 (2021), pp. 13190–13205. ISSN: 0360-3199. DOI: https://doi.org/10.1016/j.ijhydene.2021.01.085.

[47] B. Guinot et al. “Profitability of an electrolysis based hydrogen production plant providing grid balancing services”. In: *Intl. J. Hydrog. Ener.* 40.29 (2015), pp. 8778–8787. ISSN: 0360-3199. DOI: 10.1016/j.ijhydene.2015.05.033.

[48] C.-J. Zhong et al. “Fuel cell technology: nano-engineered multimetallic catalysts”. In: *Ener. Environ. Sci.* 1.4 (2008), pp. 454–466. DOI: 10.1039/B810734N.

[49] Z. Chen et al. “A review on non-precious metal electrocatalysts for PEM fuel cells”. In: *Ener. Environ. Sci.* 4.9 (2011), pp. 3167–3192. DOI: 10.1039/C0EE00558D.

[50] H. T. Chung et al. “Direct atomic-level insight into the active sites of a high-performance PGM-free ORR catalyst”. In: *Science* 357.6350 (2017), pp. 479–484. DOI: 10.1126/science.aan2255.

[51] S. T. Thompson et al. “Direct hydrogen fuel cell electric vehicle cost analysis: System and high-volume manufacturing description, validation, and outlook”. In: *J. Power Sources* 399 (2018), pp. 304–313. ISSN: 0378-7753. DOI: 10.1016/j.jpowsour.2018.07.100.

[52] S. T. Thompson and D. Papageorgopoulos. “Platinum group metal-free catalysts boost cost competitiveness of fuel cell vehicles”. In: *Nat. Catalysis* 2.7 (2019), pp. 558–561. DOI: 10.1038/s41929-019-0291-x.

[53] X. Huang et al. “High-performance transition metal–doped Pt3Ni octahedra for oxygen reduction reaction”. In: *Science* 348.6240 (2015), pp. 1230–1234. ISSN: 0036-8075. DOI: 10.1126/science.aaa8765.

[54] L. George and S. K. Saxena. “Structural stability of metal hydrides, alanates and borohydrides of alkali and alkali- earth elements: A review”. In: *Intl. J. Hydrog. Ener.* 35.11 (June 2010), pp. 5454–5470. ISSN: 03603199. DOI: 10.1016/j.ijhydene.2010.03.078.

[55] A. Schneemann et al. “Nanostructured metal hydrides for hydrogen storage”. In: *Chem. Rev.* 118.22 (2018), pp. 10775–10839. DOI: 10.1021/acs.chemrev.8b00313.

[56] J. L. White et al. “Identifying the role of dynamic surface hydroxides in the dehydrogenation of Ti-doped NaAlH4”. In: *ACS Appl. Mater. Inter* 11.5 (2019), pp. 4930–4941. DOI: 10.1021/acsami.8b17650.

[57] E. Schrödinger. “Quantisierung als Eigenwertproblem”. In: *Ann. Physik* 81 (1926), p. 109. DOI: 10.1002/andp.19263851302.

[58] F. Bloch. “Heisenberg and the early days of quantum mechanics”. In: *Phys. Today* 29.12 (1976), pp. 23–27. DOI: 10.1063/1.3024633.

[59] R. M. Martin. *Electronic structure: basic theory and practical methods*. Cambridge university press, 2013. DOI: 10.1017/9781108555586.

[60] M. Born and R. Oppenheimer. “Zur Quantentheorie der Molekeln”. In: *Ann. Physik* 389.20 (1927), pp. 457–484. DOI: 10.1002/andp.19273892002.

[61] P. E. Blöchl. “Theory and practice of density-functional theory”. In: *arXiv preprint arXiv:1108.1104* (2011). URL: https://arxiv.org/abs/1108.1104.

[62] D. R. Hartree. “The wave mechanics of an atom with a non-coulomb central field. Part I. Theory and methods”. In: *Mathematical Proceedings of the Cambridge Philosophical Society*. Vol. 24. 1. Cambridge University Press. 1928, pp. 111–132. DOI: 10.1017/S0305004100011920.

[63] V. Fock. “Näherungsmethode zur Lösung des quantenmechanischen Mehrkörperproblems”. In: *Z. Phys.* 61.1-2 (1930), pp. 126–148. DOI: 10.1007/BF01340294.

[64] J. C. Slater. “The theory of complex spectra”. In: *Phys. Rev.* 34.10 (1929), p. 1293. DOI: 10.1103/PhysRev.34.1293.

[65] D. M. Ceperley and B. J. Alder. "Ground state of the electron gas by a stochastic method". In: *Phys. Rev. Lett.* 45 (1980), pp. 566–569. DOI: 10.1103/PhysRevLett.45.566.

[66] P. Hohenberg and W. Kohn. "Inhomogeneous electron gas". In: *Phys. Rev.* 136.3B (1964), B864. DOI: 10.1103/PhysRev.136.B864.

[67] W. Kohn and L. J. Sham. "Self-Consistent Equations Including Exchange and Correlation Effects". In: *Phys. Rev.* 140.4 (Nov. 15, 1965), A1133–A1138. ISSN: 0031-899X. DOI: 10.1103/PhysRev.140.A1133.

[68] J. P. Perdew and A. Zunger. "Self-interaction correction to density-functional approximations for many-electron systems". In: *Phys. Rev. B* 23.10 (1981), p. 5048. DOI: 10.1103/PhysRevB.23.5048.

[69] R. W. Godby, M. Schlüter, and L. Sham. "Self-energy operators and exchange-correlation potentials in semiconductors". In: *Phys. Rev. B* 37.17 (1988), p. 10159. DOI: 10.1103/PhysRevB.37.10159.

[70] J. P. Perdew and K. Schmidt. "Jacob's ladder of density functional approximations for the exchange-correlation energy". In: *AIP Conf. Proc.* Vol. 577. 1. American Institute of Physics. 2001, pp. 1–20. DOI: 10.1063/1.1390175.

[71] J. P. Perdew. "Accurate density functional for the energy: Real-space cutoff of the gradient expansion for the exchange hole". In: *Phys. Rev. Lett.* 55.16 (1985), p. 1665. DOI: 10.1103/PhysRevLett.55.1665.

[72] J. P. Perdew, K. Burke, and M. Ernzerhof. "Generalized Gradient Approximation Made Simple". In: *Phys. Rev. Lett.* 77 (18 1996), pp. 3865–3868. DOI: 10.1103/PhysRevLett.77.3865.

[73] U. von Barth. "Basic density-functional theory—an overview". In: *Phys. Scripta* 2004.T109 (2004), p. 9. DOI: 10.1238/Physica.Topical.109a00009.

[74] K. Capelle. "A bird's-eye view of density-functional theory". In: *Braz. J. Phys.* 36.4A (2006), pp. 1318–1343. DOI: 10.1590/S0103-97332006000700035.

[75] E. Engel and R. M. Dreizler. *Density functional theory*. Springer, 2013. DOI: 10.1007/978-3-642-14090-7.

[76] A. D. Becke. "A new mixing of Hartree–Fock and local density-functional theories". In: *J. Chem. Phys.* 98.2 (1993), pp. 1372–1377. DOI: 10.1063/1.464304.

[77] J. P. Perdew, M. Ernzerhof, and K. Burke. "Rationale for mixing exact exchange with density functional approximations". In: *J Chem. Phys.* 105.22 (1996), pp. 9982–9985. DOI: 10.1063/1.472933.

[78] M. Bernardi. "Physical origin of the one-quarter exact exchange in density functional theory". In: *J. Phys.: Condens. Matter* 32.38 (2020), p. 385501. DOI: 10.1088/1361-648X/ab9409.

[79] J. Heyd, G. E. Scuseria, and M. Ernzerhof. "Hybrid functionals based on a screened Coulomb potential". In: *J. Chem. Phys.* 118.18 (May 8, 2003), pp. 8207–8215. ISSN: 0021-9606, 1089-7690. DOI: 10.1063/1.1564060.

[80] J. Heyd and G. E. Scuseria. "Efficient hybrid density functional calculations in solids: Assessment of the Heyd–Scuseria–Ernzerhof screened Coulomb hybrid functional". In: *J. Chem. Phys.* 121 (2004), pp. 1187–1192. DOI: 10.1063/1.1760074.

[81] G. E. Heyd, J. Scuseria, and M. Ernzerhof. "Erratum: "Hybrid functionals based on a screened Coulomb potential"[J. Chem. Phys. 118, 8207 (2003)]". In: *J. Chem. Phys.* 124 (2006), p. 219906. DOI: 10.1063/1.2204597.

[82] M. L. Cohen. "Pseudopotential panacea". In: *Phys. Today;(United States)* 32.7 (1979). DOI: 10.1063/1.2995618.

[83] D. Vanderbilt. "Soft self-consistent pseudopotentials in a generalized eigenvalue formalism". In: *Phys. Rev. B* 41.11 (1990), p. 7892. DOI: 10.1103/PhysRevB.41.7892.

[84] M. L. Cohen. "Pseudopotentials and total energy calculations". In: *Phys. Scripta* 1982.T1 (1982), p. 5. DOI: 10.1088/0031-8949/1982/T1/001.

[85] E. Fermi. "Dispacement by pressure of the high lines of the spectral series". In: *Nuovo Cimento* 11 (1934), p. 157. DOI: 10.1007/BF02959829.

[86] E. Amaldi et al. "Artificial radioactivity produced by neutron bombardment—II". In: *Proc. Roy. Soc. London* 149.868 (1935), pp. 522–558. DOI: 10.1098/rspa.1935.0080.

[87] C. Herring. "A new method for calculating wave functions in crystals". In: *Phys. Rev.* 57.12 (1940), p. 1169. DOI: 10.1103/PhysRev.57.1169.

[88] M. L. Cohen and V. Heine. "The Fitting of Pseudopotentials to Experimental Data and Their Subsequent Application". In: ed. by H. Ehrenreich, F. Seitz, and D. Turnbull. Vol. 24. Solid State Physics. Academic Press, 1970, pp. 37–248. DOI: 10.1016/S0081-1947(08)60070-3.

[89] D. Hamann, M Schlüter, and C Chiang. "Norm-conserving pseudopotentials". In: *Phys. Rev. Lett.* 43.20 (1979), p. 1494. DOI: 10.1103/PhysRevLett.43.1494.

[90] P. E. Blöchl. "Projector augmented-wave method". In: *Phys. Rev. B* 50.24 (1994), pp. 17953–17979. DOI: 10.1103/PhysRevB.50.17953.

[91] G. Kresse and D. Joubert. “From ultrasoft pseudopotentials to the projector augmented-wave method”. In: *Phys. Rev. B* 59.3 (1999), pp. 1758–1775. DOI: 10.1103/PhysRevB.59.1758.

[92] C. J. Humphreys. “STEM imaging of crystals and defects”. In: *Introduction to Analytical Electron Microscopy*. Springer, 1979, p. 305. DOI: 10.1007/978-1-4757-5581-7.

[93] C. Freysoldt et al. “First-principles calculations for point defects in solids”. In: *Rev. Mod. Phys.* 86.1 (2014), p. 253. DOI: 10.1103/RevModPhys.86.253.

[94] A. Walsh et al. “Self-regulation mechanism for charged point defects in hybrid halide perovskites”. In: *Angew. Chem.* 127.6 (2015), pp. 1811–1814. DOI: 10.1002/ange.201409740.

[95] A. K. Singh et al. “Sources of electrical conductivity in SnO_2”. In: *Phys. Rev. Lettl* 101.5 (2008), p. 055502. DOI: 10.1103/PhysRevLett.101.055502.

[96] X. Zhang, J.-X. Shen, and C. G. Van de Walle. “First-Principles Simulation of Carrier Recombination Mechanisms in Halide Perovskites”. In: *Adv. Ener. Mater.* 10.13 (2020), p. 1902830. DOI: 10.1002/aenm.201902830.

[97] E. Kioupakis et al. “First-principles calculations of indirect Auger recombination in nitride semiconductors”. In: *Phys. Rev. B* 92.3 (2015), p. 035207. DOI: 10.1103/PhysRevB.92.035207.

[98] M. M. Can et al. “Electrical and optical properties of point defects in ZnO thin films”. In: *J. Phys. D: Appl. Phys.* 45.19 (2012), p. 195104. DOI: 10.1088/0022-3727/45/19/195104.

[99] I. Chatratin et al. “Role of point defects in the electrical and optical properties of In_2O_3”. In: *Phys. Rev. Mater.* 3.7 (2019), p. 074604. DOI: 10.1103/PhysRevMaterials.3.074604.

[100] C. G. Van de Walle. “Hydrogen as a cause of doping in zinc oxide”. In: *Phys. Rev. Lett.* 85.5 (2000), p. 1012. DOI: 10.1103/PhysRevLett.85.1012.

[101] C. Freysoldt, J. Neugebauer, and C. G. Van de Walle. “Fully *ab initio* finite-size corrections for charged-defect supercell calculations”. In: *Phys. Rev. Lett.* 102 (1 2009), p. 016402. DOI: 10.1103/PhysRevLett.102.016402.

[102] C. Freysoldt, J. Neugebauer, and C. G. Van de Walle. “Electrostatic interactions between charged defects in supercells”. In: *Phys. Status Solidi B* 248.5 (2011), pp. 1067–1076. ISSN: 1521-3951. DOI: 10.1002/pssb.201046289.

[103] H.-P. Komsa, T. T. Rantala, and A. Pasquarello. “Finite-size supercell correction schemes for charged defect calculations”. In: *Phys. Rev. B* 86.4 (2012), p. 045112. DOI: 10.1103/PhysRevB.86.045112.

[104] M. W. Chase Jr. “NIST-JANAF thermochemical tables”. In: *J. Phys. Chem. Ref. Data, Monograph* 9 (1998). URL: https://janaf.nist.gov/.

[105] S. Limpijumnong and C. G. Van de Walle. “Diffusivity of native defects in GaN”. In: *Phys. Rev. B* 69.3 (2004), p. 035207. DOI: 10.1103/PhysRevB.69.035207.

[106] J. Maier. *Physical chemistry of ionic materials: ions and electrons in solids*. John Wiley & Sons, 2004. DOI: 10.1002/0470020229.

[107] G. H. Vineyard. “Frequency factors and isotope effects in solid state rate processes”. In: *J. Phys. Chem. Solids* 3.1 (1957), pp. 121–127. DOI: 10.1016/0022-3697(57)90059-8.

[108] G. Mills and H. Jónsson. "Quantum and thermal effects in H_2 dissociative adsorption: Evaluation of free energy barriers in multidimensional quantum systems". In: *Phys. Rev. Lett.* 72 (7 1994), pp. 1124–1127. DOI: 10.1103/PhysRevLett.72.1124.

[109] G. Mills, H. Jónsson, and G. K. Schenter. "Reversible work transition state theory: application to dissociative adsorption of hydrogen". In: *Surf. Sci.* 324.2 (1995), pp. 305–337. ISSN: 0039-6028. DOI: 10.1016/0039-6028(94)00731-4.

[110] H. Jónsson, G. Mills, and K. W. Jacobsen. "Nudged elastic band method for finding minimum energy paths of transitions". In: *Classical and Quantum Dynamics in Condensed Phase Simulations*. Ed. by B. J. Berne, G. Ciccotti, and D. F. Coker. World Scientific, 1998, pp. 385–404. DOI: 10.1142/9789812839664_0016.

[111] G. Henkelman and H. Jónsson. "Improved tangent estimate in the nudged elastic band method for finding minimum energy paths and saddle points". In: *J. Chem. Phys.* 113.22 (Dec. 8, 2000), pp. 9978–9985. ISSN: 0021-9606, 1089-7690. DOI: 10.1063/1.1323224.

[112] G. Henkelman, B. P. Uberuaga, and H. Jónsson. "A climbing image nudged elastic band method for finding saddle points and minimum energy paths". In: *J. Chem. Phys.* 113.22 (2000), pp. 9901–9904. DOI: 10.1063/1.1329672.

[113] G. Kresse and J. Furthmüller. "Efficient iterative schemes for *ab initio* total-energy calculations using a plane-wave basis set". In: *Phys. Rev. B* 54.16 (1996), p. 11169. DOI: 10.1103/PhysRevB.54.11169.

[114] A. J. E. Rowberg, L. Weston, and C. G. Van de Walle. "Optimizing proton conductivity in zirconates through defect engineering". In: *ACS Appl. Ener. Mater.* 2 (2019), pp. 2611–2619. DOI: 10.1021/acsaem.8b02222.

[115] A. J. E. Rowberg, M. W. Swift, and C. G. Van de Walle. "Understanding carbon contamination in the proton-conducting zirconates and cerates". In: *Phys. Chem. Chem. Phys.* 23 (2021), pp. 14205–14211. DOI: 10.1039/D1CP01902C.

[116] W. G. Coors and M. Marrony. *Three Decades of Ceramic Proton Conductors: The Road to Commercialization*. Pan Stanford, 2015, pp. xi–xvii. URL: https://www.routledge.com/Proton-Conducting-Ceramics-From-Fundamentals-to-Applied-Research/Marrony/p/book/9789814613842.

[117] H. Iwahara et al. "Protonic conduction in calcium, strontium and barium zirconates". In: *Solid State Ionics* 61.1 (1993), pp. 65–69. DOI: 10.1016/0167-2738(93)90335-Z.

[118] T. Yajima et al. "Application of hydrogen sensor using proton conductive ceramics as a solid electrolyte to aluminum casting industries". In: *Solid State Ionics* 79 (1995), pp. 333–337. DOI: 10.1016/0167-2738(95)00083-I.

[119] H Iwahara et al. "Proton conduction in sintered oxides based on $BaCeO_3$". In: *J. Electrochem. Soc.* 135.2 (1988), pp. 529–533. DOI: 10.1149/1.2095649.

[120] K. Katahira et al. "Protonic conduction in Zr-substituted $BaCeO_3$". In: *Solid State Ionics* 138.1-2 (2000), pp. 91–98. DOI: 10.1016/S0167-2738(00)00777-3.

[121] E. Fabbri, D. Pergolesi, and E. Traversa. "Materials challenges toward proton-conducting oxide fuel cells: a critical review". In: *Chem. Soc. Rev.* 39.11 (2010), pp. 4355–4369. DOI: 10.1039/B902343G.

[122] N. Kochetova et al. "Recent activity in the development of proton-conducting oxides for high-temperature applications". In: *RSC Adv.* 6.77 (2016), pp. 73222–73268. DOI: 10.1039/C6RA13347A.

[123] P. Sawant et al. “Synthesis, stability and conductivity of $BaCe_{0.8-x}Zr_xY_{0.2}O_{3-\delta}$ as electrolyte for proton conducting SOFC”. In: *Intl. J. Hydrog. Ener.* 37.4 (2012), pp. 3848–3856. DOI: 10.1016/j.ijhydene.2011.04.106.

[124] J. Lü et al. “Chemical stability of doped $BaCeO_3$-$BaZrO_3$ solid solutions in different atmospheres”. In: *J. Rare Earths* 26.4 (2008), pp. 505–510. DOI: 10.1016/S1002-0721(08)60127-1.

[125] K. H. Ryu and S. M. Haile. “Chemical stability and proton conductivity of doped $BaCeO_3$-$BaZrO_3$ solid solutions”. In: *Solid State Ionics* 125 (1999), p. 355. DOI: 10.1016/S0167-2738(99)00196-4.

[126] T. S. Bjørheim et al. “A combined conductivity and DFT study of protons in $PbZrO_3$ and alkaline earth zirconate perovskites”. In: *Solid State Ionics* 181.3 (2010), pp. 130 –137. ISSN: 0167-2738. DOI: 10.1016/j.ssi.2009.04.013.

[127] M. E. Björketun, P. G. Sundell, and G. Wahnström. “Effect of acceptor dopants on the proton mobility in $BaZrO_3$: A density functional investigation”. In: *Phys. Rev. B* 76.5 (Aug. 23, 2007), p. 054307. ISSN: 1098-0121, 1550-235X. DOI: 10.1103/PhysRevB.76.054307.

[128] M. Saiful Islam, R. A. Davies, and J. D. Gale. “Proton Migration and Defect Interactions in the $CaZrO_3$ Orthorhombic Perovskite: A Quantum Mechanical Study”. In: *Chem. Mater.* 13.6 (June 2001), pp. 2049–2055. ISSN: 0897-4756, 1520-5002. DOI: 10.1021/cm010005a.

[129] S. J. Stokes and M. S. Islam. “Defect chemistry and proton-dopant association in $BaZrO_3$ and $BaPrO_3$”. In: *J. Mater. Chem.* 20 (2010), pp. 6258–6264. DOI: 10.1039/C0JM00328J.

[130] L. Weston et al. “Hybrid functional calculations of point defects and hydrogen in $SrZrO_3$”. In: *Phys. Rev. B* 89.18 (May 22, 2014). ISSN: 1098-0121, 1550-235X. DOI: 10.1103/PhysRevB.89.184109.

[131] S. G. Kang and D. S. Sholl. “First-principles investigation of chemical stability and proton conductivity of M-doped $BaZrO_3$ (M= K, Rb, and Cs)”. In: *J. Am. Ceram. Soc.* 100.7 (2017), pp. 2997–3003. DOI: 10.1111/jace.14839.

[132] A. Løken et al. “Alkali metals as efficient A-site acceptor dopants in proton conducting $BaZrO_3$”. In: *J. Mater. Chem. A* 4.23 (2016), pp. 9229–9235. DOI: 10.1039/C6TA01446A.

[133] M. Swift, A. Janotti, and C. G. Van de Walle. “Small polarons and point defects in barium cerate”. In: *Phys. Rev. B* 92.21 (2015), p. 214114. DOI: 10.1103/PhysRevB.92.214114.

[134] M. Swift and C. G. Van de Walle. “Impact of point defects on proton conduction in strontium cerate”. In: *J. Phys. Chem. C* 120.18 (2016), pp. 9562–9568. DOI: 10.1021/acs.jpcc.6b00765.

[135] L. Weston et al. “Acceptor doping in the proton conductor $SrZrO_3$”. In: *Phys. Chem. Chem. Phys.* 19.18 (2017), pp. 11485–11491. ISSN: 1463-9076, 1463-9084. DOI: 10.1039/C7CP01471F.

[136] A. S. Patnaik and A. V. Virkar. “Transport properties of potassium-doped $BaZrO_3$ in oxygen-and water-vapor-containing atmospheres”. In: *J. Electrochem. Soc.* 153.7 (2006), A1397–A1405. DOI: 10.1149/1.2203095.

[137] X. Xu, S. Tao, and J. T. Irvine. “Proton conductivity of potassium doped barium zirconates”. In: *J. Solid State Chem.* 183.1 (2010), pp. 93–98. DOI: 10.1016/j.jssc.2009.10.017.

[138] V. Stevanović et al. “Correcting density functional theory for accurate predictions of compound enthalpies of formation: Fitted elemental-phase reference energies”. In: *Phys. Rev. B* 85 (2012), p. 115104. DOI: 10.1103/PhysRevB.85.115104.

[139] R. R. Brown and K. O. Bennington. “Thermodynamic properties of calcium zironate ($CaZrO_3$)”. In: *Thermochim. Acta* 106 (1986), pp. 183 –190. DOI: 10.1016/0040-6031(86)85130-9.

[140] M. Huntelaar, A. Booij, and E. Cordfunke. “The standard molar enthalpies of formation of $BaZrO_3$(s) and $SrZrO_3$(s)”. In: *J. Chem. Thermodyn.* 26.10 (1994), pp. 1095 –1101. DOI: 10.1006/jcht.1994.1127.

[141] E. Cordfunke, A. Booij, and M. Huntelaar. “The thermochemical properties of $BaCeO_3$(s) and $SrCeO_3$(s) from T = (5 to 1500) K”. In: *J. Chem. Thermodyn.* 30 (1998), pp. 437–447. DOI: 10.1006/jcht.1997.0302.

[142] D. R. Lide. “CRC handbook of chemistry and physics”. In: *12J204* (2012).

[143] I Molodetsky et al. “Energetics of oxidation of oxynitrides: Zr–N–O, Y–Zr–N–O, Ca–Zr–N–O, and Mg–Zr–N–O”. In: *J. Mater. Res.* 15.11 (2000), pp. 2558–2570. DOI: 10.1557/JMR.2000.0366.

[144] H. J. A. Koopmans, G. M. H. van de Velde, and P. J. Gellings. “Powder neutron diffraction study of the perovskites $CaTiO_3$ and $CaZrO_3$”. In: *Acta Crystallogr., Sect. C: Cryst. Struct. Commun.* 39.10 (Oct. 15, 1983), pp. 1323–1325. ISSN: 01082701. DOI: 10.1107/S0108270183008392.

[145] I. Rosa et al. “A theoretical investigation of the structural and electronic properties of orthorhombic $CaZrO_3$”. In: *Ceram. Int.* 41.2 (Mar. 2015), pp. 3069–3074. ISSN: 02728842. DOI: 10.1016/j.ceramint.2014.10.149.

[146] B. J. Kennedy, C. J. Howard, and B. C. Chakoumakos. "High-temperature phase transitions in $SrZrO_3$". In: *Phys. Rev. B* 59.6 (1999), p. 4023. DOI: 10.1103/PhysRevB.59.4023.

[147] A. Zhang et al. "Novel photoluminescence of $SrZrO_3$ nanocrystals synthesized through a facile combustion method". In: *J. Alloys Cmpnd.* 433.1-2 (2007), pp. L7–L11. DOI: 10.1016/j.jallcom.2006.06.083.

[148] Y. Lee et al. "Systematic trends in the electronic structure parameters of the 4*d* transition-metal oxides $SrMO_3$ (M= Zr, Mo, Ru, and Rh)". In: *Phys. Rev. B* 67.11 (2003), p. 113101. DOI: 10.1103/PhysRevB.67.113101.

[149] R. Borja-Urby et al. "Blue and red emission in wide band gap $BaZrO_3$:Yb^{3+},Tm^{3+}". In: *Mater. Sci. Eng. B* 174.1 (Oct. 2010), pp. 169–173. ISSN: 09215107. DOI: 10.1016/j.mseb.2010.04.024.

[150] T Yajima et al. "Protonic conduction in $SrZrO_3$-based oxides". In: *Solid State Ionics* 51.1-2 (1992), pp. 101–107. DOI: 10.1016/0167-2738(92)90351-O.

[151] R. D. Shannon. "Revised effective ionic radii and systematic studies of interatomic distances in halides and chalcogenides". In: *Acta Cryst.* A32.5 (1976), pp. 751–767. DOI: 10.1107/S0567739476001551.

[152] H. D. Tailor et al. "Impact of nitrogen and carbon on defect equilibrium in ZrO_2". In: *Acta Mater.* 117 (Sept. 2016), pp. 286–292. ISSN: 13596454. DOI: 10.1016/j.actamat.2016.07.003.

[153] J. L. Lyons et al. "Carbon as a shallow donor in transparent conducting oxides". In: *Phys. Rev. Appl.* 2.6 (2014), p. 064005. DOI: 10.1103/PhysRevApplied.2.064005.

[154] H. D. Tailor et al. “Carbon-induced trapping levels in oxide dielectrics”. In: *J. Vac. Sci. Tech.* 33 (2015), 01A120. DOI: 10.1116/1.4901234.

[155] A. Janotti and C. G. Van de Walle. “Hydrogen multicentre bonds”. In: *Nat. Mater.* 6.1 (2007), p. 44. DOI: 10.1038/nmat1795.

[156] T. S. Bjørheim, E. A. Kotomin, and J. Maier. “Hydration entropy of $BaZrO_3$ from first principles phonon calculations”. In: *J. Mater. Chem. A* 3.14 (2015), pp. 7639–7648. DOI: 10.1039/C4TA06880G.

[157] J.-H. Kim et al. “Study on the chemical stability of Y-doped $BaCeO_{3-\delta}$ and $BaZrO_{3-\delta}$ films deposited by aerosol deposition”. In: *Thin Solid Films* 520.3 (2011), pp. 1015–1021. DOI: 10.1016/j.tsf.2011.08.013.

[158] Y. Li et al. “Chemical stability study of nanoscale thin film yttria-doped barium cerate electrolyte for micro solid oxide fuel cells”. In: *J. Power Sources* 268 (2014), pp. 804–809. DOI: 10.1016/j.jpowsour.2014.06.128.

[159] N. Zakowsky, S. Williamson, and J. T. Irvine. “Elaboration of CO_2 tolerance limits of $BaCe_{0.9}Y_{0.1}O_{3-\delta}$ electrolytes for fuel cells and other applications”. In: *Solid State Ionics* 176.39-40 (2005), pp. 3019–3026. DOI: 10.1016/j.ssi.2005.09.040.

[160] J. Li et al. “Stability of Zr-Doped $SrCeO_3$ Under Wet CO/CO_2 Atmospheres”. In: *ECS Trans.* 11.33 (2008), p. 81. DOI: 10.1149/1.3038911.

[161] M. Scholten et al. “Synthesis of strontium and barium cerate and their reaction with carbon dioxide”. In: *Solid State Ionics* 61.1-3 (1993), pp. 83–91. DOI: 10.1016/0167-2738(93)90338-4.

[162] F. Chen et al. “Preparation of Nd-doped barium cerate through different routes”. In: *Solid State Ionics* 100.1-2 (1997), pp. 63–72. DOI: 10.1016/S0167-2738(97)00265-8.

[163] S. D. Flint and R. C. Slade. “Comparison of calcium-doped barium cerate solid electrolytes prepared by different routes”. In: *Solid State Ionics* 77 (1995), pp. 215–221. DOI: 10.1016/0167-2738(94)00232-H.

[164] H. Potdar et al. “Preparation and characterization of strontium zirconate ($SrZrO_3$) fine powders”. In: *Mater. Chem. Phys.* 65.2 (2000), pp. 178–185. DOI: 10.1016/S0254-0584(00)00238-8.

[165] A. Suresh et al. “Synthesis of cobalt-doped barium cerate-zirconate and its evaluation for hydrogen production and electrochemical characterization”. In: *J. Mater. Sci.* 45.12 (2010), pp. 3215–3227. DOI: 10.1007/s10853-010-4329-3.

[166] A. J. Rowberg, L. Weston, and C. G. Van de Walle. “Ion-transport engineering of alkaline-earth hydrides for hydride electrolyte applications”. In: *Chem. Mater.* 30 (2018), pp. 5878–5885. DOI: 10.1021/acs.chemmater.8b01593.

[167] E. S. Shubina, N. V. Belkova, and L. M. Epstein. “Novel types of hydrogen bonding with transition metal π-complexes and hydrides”. In: *J. Organomet. Chem.* 536 (1997), pp. 17–29. DOI: 10.1016/S0022-328X(96)06791-5.

[168] M. C. Verbraeken, E. Suard, and J. T. S. Irvine. “Structural and electrical properties of calcium and strontium hydrides”. In: *J. Mater. Chem.* 19.18 (2009), pp. 2766–2770. ISSN: 0959-9428, 1364-5501. DOI: 10.1039/b820173k.

[169] H. Smithson et al. “First-principles study of the stability and electronic structure of metal hydrides”. In: *Phys. Rev. B* 66 (2002), p. 144107. DOI: 10.1103/PhysRevB.66.144107.

[170] V. P. Gorelov and S. F. Pal'guev. "Conductivity in CaH_2–LiH and CaH_2–CaF_2 systems". In: *Electrokhimya* 28.10 (1992), pp. 1578–1580.

[171] S. Singh and S. Eijt. "Hydrogen vacancies facilitate hydrogen transport kinetics in sodium hydride nanocrystallites". In: *Phys. Rev. B* 78.22 (Dec. 30, 2008), p. 224110. ISSN: 1098-0121, 1550-235X. DOI: 10.1103/PhysRevB.78.224110.

[172] R. R. Wixom et al. "First principles site occupation and migration of hydrogen, helium, and oxygen in β-phase erbium hydride". In: *J. Appl. Phys.* 103.12 (June 15, 2008), p. 123708. ISSN: 0021-8979, 1089-7550. DOI: 10.1063/1.2940134.

[173] J. F. Herbst. "On extending Miedema's model to predict hydrogen content in binary and ternary hydrides". In: *J. Alloys Cmpnd.* 337.1 (May 2, 2002), pp. 99–107. ISSN: 0925-8388. DOI: 10.1016/S0925-8388(01)01939-9.

[174] L. G. Hector et al. "*Ab Initio* thermodynamic and elastic properties of alkaline-earth metals and their hydrides". In: *Phys. Rev. B* 76.1 (July 27, 2007), p. 014121. ISSN: 1098-0121, 1550-235X. DOI: 10.1103/PhysRevB.76.014121.

[175] C. Wolverton, V. Ozoliņš, and M. Asta. "Hydrogen in aluminum: First-principles calculations of structure and thermodynamics". In: *Phys. Rev. B* 69.14 (Apr. 12, 2004), p. 144109. ISSN: 1098-0121, 1550-235X. DOI: 10.1103/PhysRevB.69.144109.

[176] J. Neugebauer and C. G. Van de Walle. "Chemical trends for acceptor impurities in GaN". In: *J. Appl. Phys.* 85 (1999), p. 3003. DOI: 10.1063/1.369619.

[177] A. J. E. Rowberg, L. Weston, and C. G. Van de Walle. "Defect chemistry and Hydrogen Transport in La/Sr-Based Oxyhydrides". In: *J. Phys. Chem. C* 125 (4 2021), pp. 2250–2256. DOI: 10.1021/acs.jpcc.0c09222.

[178] Y. Kobayashi et al. "An oxyhydride of $BaTiO_3$ exhibiting hydride exchange and electronic conductivity". In: *Nat. Mater.* 11.6 (Apr. 15, 2012), pp. 507–511. ISSN: 1476-1122, 1476-4660. DOI: 10.1038/nmat3302.

[179] K. Fukui et al. "Characteristic fast H^- ion conduction in oxygen-substituted lanthanum hydride". In: *Nat. Commun.* 10.1 (2019), pp. 1–8. DOI: 10.1038/s41467-019-10492-7.

[180] Q. Bai et al. "First-Principles Study of Oxyhydride H–Ion Conductors: Toward Facile Anion Conduction in Oxide-Based Materials". In: *ACS Appl. Ener. Mater.* 1.4 (2018), pp. 1626–1634. DOI: 10.1021/acsaem.8b00077.

[181] X. Liu, T. S. Bjørheim, and R. Haugsrud. "Formation of defects and their effects on hydride ion transport properties in a series of K_2NiF_4-type oxyhydrides". In: *J. Mater. Chem. A* 6.4 (2018), pp. 1454–1461. URL: 10.1039/C7TA08435H.

[182] N. Matsui et al. "Ambient pressure synthesis of La_2LiHO_3 as a solid electrolyte for a hydrogen electrochemical cell". In: *J. Am. Ceram. Soc.* 102.6 (2019), pp. 3228–3235. DOI: 10.1111/jace.16214.

[183] F. W. Poulsen. "Speculations on the existence of hydride ions in proton conducting oxides". In: *Solid State Ionics* 145 (2001), pp. 387–397. DOI: 10.1016/S0167-2738(01)00935-3.

[184] M. Widerøe et al. "Proton and apparent hydride ion conduction in Al-substituted $SrTiO_3$". In: *Solid State Ionics* 154-155 (Dec. 2, 2002), pp. 669–677. ISSN: 01672738. DOI: 10.1016/S0167-2738(02)00702-6.

[185] Ø. S. Fjellvåg et al. "Thermal and Structural Aspects of the Hydride-Conducting Oxyhydride La_2LiHO_3 Obtained via a Halide Flux Method". In: *Inorg. Chem.* 56.18 (2017), pp. 11123–11128. DOI: 10.1021/acs.inorgchem.7b01409.

[186] Ø. S. Fjellvåg et al. "A combined deep inelastic neutron scattering and ab initio lattice dynamics study of the hydride anion dynamics and bonding in La_2LiHO_3 oxyhydride". In: *J. Phys. Commun.* 3.10 (2019), p. 103002. DOI: 10.1088/2399-6528/ab4be6.

[187] A. J. E. Rowberg and C. G. Van de Walle. "Hydride conductivity in nitride hydrides". In: *ACS Appl. Energy Mater.* 4.6 (2021), pp. 6348–6355. DOI: 10.1021/acsaem.1c01208.

[188] A. Aleksanyan and S. Dolukhanyan. "Combustion of niobium in hydrogen and nitrogen. Synthesis of niobium hydrides and hydridonitrides". In: *Intl. J. Hydrog. Ener.* 26.5 (2001), pp. 429–433. DOI: 10.1016/S0360-3199(00)00074-4.

[189] P. Chen et al. "Interaction of hydrogen with metal nitrides and imides". In: *Nature* 420.6913 (2002), pp. 302–304. DOI: 10.1038/nature01210.

[190] N. Tapia-Ruiz et al. "Rapid microwave synthesis, characterization and reactivity of lithium nitride hydride, Li_4NH". In: *Materials* 6.11 (2013), pp. 5410–5426. DOI: 10.3390/ma6115410.

[191] O. Reckeweg and F. J. DiSalvo. "Alkaline earth metal nitride compounds with the composition M_2NX (M= Ca, Sr, Ba; X= , H, Cl or Br)". In: *Solid state sciences* 4.5 (2002), pp. 575–584. DOI: 10.1016/S1293-2558(02)01300-6.

[192] R. Chemnitzer et al. "(Sr_2N) H: Untersuchungen zur Redox-Intercalation von Wasserstoff in Sr_2N". In: *Z. Anorg. Allg. Chem.* 631.10 (2005), pp. 1813–1817. DOI: 10.1002/zaac.200500105.

[193] B Wegner et al. "Structure and H–ionic-conductivity of barium hydride nitride, $Ba_2H(D)N$". In: *Eur. J. Solid State Inorg. Chem.* 29.6 (1992), pp. 1217–1227.

URL: https://pascal-francis.inist.fr/vibad/index.php?action=getRecordDetail&idt=4597311.

[194] F Altorfer et al. "H^--jump diffusion in barium-nitride-hydride Ba_2NH". In: *Solid State Ionics* 70 (1994), pp. 272–277. DOI: 10.1016/0167-2738(94)90322-0.

[195] B. Blaschkowski and T. Schleid. "Darstellung und Kristallstruktur des Lithium-Strontium-Hydridnitrids $LiSr_2H_2N$". In: *Z. Anorg. Allg. Chem.* 633.15 (2007), pp. 2644–2648. DOI: 10.1002/zaac.200700315.

[196] D. M. Liu et al. "Synthesis and crystal structure of a novel nitride hydride Sr_2LiNH_2". In: *J. Alloys Cmpnds.* 495.1 (2010), pp. 272–274. DOI: 10.1016/j.jallcom.2010.02.011.

[197] J. M. Gregoire et al. "High mobility single crystalline ScN and single-orientation epitaxial YN on sapphire via magnetron sputtering". In: *J. Appl. Phys.* 104.7 (2008), p. 074913. DOI: 10.1063/1.2996006.

[198] S. Kim, J.-S. Park, and A. Walsh. "Identification of Killer Defects in Kesterite Thin-Film Solar Cells". In: *ACS Ener. Lett.* 3.2 (2018), pp. 496–500. DOI: 10.1021/acsenergylett.7b01313.

[199] A. Jain et al. "Commentary: The Materials Project: A materials genome approach to accelerating materials innovation". In: *APL Materials* 1.1 (July 2013), p. 011002. ISSN: 2166-532X. DOI: 10.1063/1.4812323.

[200] E. T. Henig and H. U. Lukas. "Calorimetric determination of enthalpy of formation and description of defect structure of ordered beta-phase $(Ni,Cu)_{1-x}Al_x$." In: *Z. Metallkn.* 66 (1975), pp. 98–106. DOI: 10.1515/ijmr-1975-660207.

[201] P. A. G. O'Hare and G. K. Johnson. "Lithium nitride (Li_3N): standard enthalpy of formation by solution calorimetry". In: *J. Chem. Thermodyn.* 7.1 (1975), pp. 13–20. DOI: 10.1016/0021-9614(75)90075-0.

[202] L. Merli, B. Lambert, and J. Fuger. "Thermochemistry of lanthanum, neodymium, samarium and americium trihydroxides and their relation to the corresponding hydroxycarbonates". In: *J. Nucl. Mater.* 247 (1997), pp. 172–176. DOI: 10.1016/S0022-3115(97)00044-5.